Active Plasmonic and Dielectric Nanoantennas

Dissertation

zur

Erlangung des Doktorgrades (Dr. rer. nat.)

der

Mathematisch-Naturwissenschaftlichen Fakultät

der

Rheinischen Friedrich-Wilhelms-Universität Bonn

vorgelegt von

Manuel Peter

aus

Siegburg

Bonn, 2017

Angefertigt mit Genehmigung der Mathematisch-Naturwissenschaftlichen Fakultät der Rheinischen Friedrich-Wilhelms-Universität Bonn

1. Gutachter:	Prof. Dr. Stefan Linden
2. Gutachterin:	Priv.-Doz. Dr. Elisabeth Soergel
Tag der mündlichen Prüfung:	11. Juli 2017
Erscheinungsjahr:	2017

Natalie und meinen Eltern

Contents

Chapter 1

Introduction

The 21st century is likely to become the *century of the photon* [1–4]. The need for higher computational power, larger bandwidth and finally the change to a computational architecture based on quantum-mechanical phenomenas leads to the urge to integrate optical signals into electronic devices [5–8]. Technology today already employs devices that manipulate electromagnetic waves, however the coined term is meant to describe a more intriguing change in technology: the miniaturization and integration of photonic devices analogous to the revolution microelectronics brought in the 20th century. Thus, it is crucial for tomorrow's technology to have a deep understanding of a broad set of nanodevices to manipulate light.

Nanoantennas are the analog optical devices to radio and microwave antennas. They have become valuable elements of the photonics toolbox to control and manipulate light on the nanoscale [9–11]. They allow for an efficient interconversion of localized excitations and propagating electromagnetic waves [12, 13]. In receiving mode, nanoantennas can locally increase the light intensity by several orders of magnitude [14–16]. This property can be used for the efficient excitation of quantum emitters [17, 18] and to boost nonlinear effects [19–23]. In transmitting mode, coupling of quantum emitters to nanoantennas allows for the control of the emission properties [24–27].

Like their microwave counterparts, nanoantennas can be categorized based on their functional principle into two large groups: (i) resonant antennas and (ii) non-resonant traveling-wave antennas. So far, most research has focused on resonant nanoantennas based either on plasmonic resonances in metals [26, 28–30] or on Mie resonances in high-refractive index dielectrics [31–33]. In this thesis, an established resonant, plasmonic nanoantenna is investigated with a novel near-field approach and a new non-resonant, dielectric nanoantenna is fabricated and characterized.

The resonant nature of plasmonic nanoantennas gives rise to strong enhancement of the local fields in sub-wavelength regions [15, 18]. A naturally emerging application for them is the sensing of small quantities of particles [34–37]. To engineer working sensing devices a complete knowledge of the optical properties of the used nanoantennas is crucial. Thus, various techniques are used to charac-

terize nanoantennas thoroughly. Besides methodical differences in the techniques, the nature of measured resonances can fundamentally differ. For example it is known that plasmonic nanoparticle's near-field properties peak at lower energies than their far-field quantities [38]. Non-dipolar modes for example are considered to be dark [12, 39], since they do not couple to far-field radiation and thus, can only be detected by special techniques. The investigation of dark modes has lead to the discovery of new effects and applications [12, 40–43].

In this thesis results on dark-mode probing of non-dipolar plasmonic resonances using quantum dot fluorescence are presented. Gold rod nanoantennas serve as a model system, since they have a well known spectrum with an easily designable resonance wavelength. Additionally, they exhibit both dipolar and non-dipolar modes. Far-field spectra of individual nanoantennas and quantum dot based near-field probing are compared. Both methods can identify the first (dipolar) mode, but only the near-field method succeeds to excite the second (non-dipolar) mode.

While metals can be treated as perfect conductors in the microwave regime, their response becomes Drude-like at optical frequencies. Thus, plasmonic nanoantennas are inherently lossy. Moreover, their resonant nature requires precise control of the antenna geometry. It is fruitful to search for nanoantennas based on a different operating principle. In long wavelength technology traveling-wave antennas are known to show broadband operation in the optical regime [44]. There is a growing interest in transferring the traveling-wave concept to higher operating frequencies in order to achieve non-resonant broadband operation [45–47]. A non-resonant highly directional leaky-wave nanoantenna is presented in this thesis. Since the leaky-wave antenna is fabricated from hafnium dioxide, it exhibits low internal loss [48]. Leaky-wave antennas are a subset of traveling-wave antennas that emit radiation over the whole length of a non-resonant guiding structure supporting the traveling wave [44]. The emission patterns of active nanoantennas with different sizes are measured by Fourier imaging. The patterns show a high directivity, which is quite competitive in comparison with plasmonic nanoantennas, however, without an inherent loss channel. One application could be a single photon source equipped with the dielectric nanoantenna.

Both investigated systems – gold rod and hafnium dioxide leaky-wave nanoantennas – are combined with quantum dots to obtain active nanoantennas. While it has been shown that optical nanoantennas can be driven electrically [49], the fluorescence of precisely deposited semiconductor quantum dots is used to excite antenna modes and gain active nanoantennas. This approach gives us a high flexibility to probe the near field of the antennas. Additionally, the proposed applications as particle sensors or single-photon sources emerge naturally. Thus, a crucial part of this thesis is the quantum dot deposition technique.

Multiple techniques to achieve control over the position of quantum emitters next to nanostructures are reported in literature. They can be largely divided into three

main groups: (i) A single quantum emitter (a single nanostructure) attached to an AFM tip is scanned over the nanostructure (the quantum emitter) [24, 28, 50]; (ii) The uncontrolled deposition of a large number of emitters on an array of nanostructures followed by sampling to find the desired geometry [36, 51, 52]; (iii) A lithography step, in which either the nanostructure or the emitter is deposited in a controlled way at predefined positions on the sample [25, 53–55]. The techniques in category (i) can be used to gain insight about the near field in three dimensions, since the movable tip is not restricted to a substrate plane. However, it is not suited for the fabrication of permanent devices, i.e., no stable composite material is produced. The second approach relies on a time-consuming scanning process and does not guarantee that the desired configuration is indeed realized on a given sample. The approach of this thesis falls into the third category. A polymer template fabricated by means of electron-beam lithography defines the sites to deposit quantum dots. They are chemically linked to those sites. The quantum dot deposition technique that was developed during the work of this thesis can be universally employed, regardless of the underlying nanostructure.

Outline

The scope of this thesis covers two distinct types of active nanoantennas for the optical spectrum of light. Their fundamental concepts and fabrication share a common foundation. Hence, in Chapter 2, 3 and 4 they are treated jointly.

Chapter 2 lays the theoretical framework for the experiments. A common model to describe the optical properties of metals and dielectrics is presented, which helps to understand their fundamental difference. The investigated nanoantennas are then introduced and their properties deduced by treating them as scaled down radio-wave devices. In the last part of the chapter the general concept of quantum dots as the shared active part of the antennas is introduced.

Chapter 3 serves as a complete overview over the fabrication method of the active nanoantennas. It is separated into two parts reflecting the two-part workflow: the electron-beam lithography of the gold and hafnium dioxide nanoantennas and the process for the controlled deposition of quantum dots. Here, the used quantum dots are introduced and characterized as well.

The versatile optical measurement setup is the scope of Chapter 4. The core of the setup is a confocal microscope used for experiments on both types of antennas. Additional measurement devices, which differ for the antenna types, are discussed as well.

Since the experiment conducted with the antenna types are disjunct, their results and discussion are separated into Chapter 5 and Chapter 6.
Chapter 5 gives details on the experimental design regarding the active plasmonic nanoantennas. The gold nanoantennas are used as a model system to investigate the difference in behavior of antenna modes when excited with a far or near field.
Chapter 6 reports on the novel active dielectric leaky-wave antenna. Their far-field patterns measured with Fourier imaging are presented and their directivities are quantified.
The outlook in Chapter 7 summarizes further experiments that promise important insight in the systems and proposes general application ideas for both antenna types.

Chapter 2

Fundamentals

This chapter introduces the foundational equations of electro-magnetism. Based on them, a model describing the optical properties of solids is introduced. It can qualitatively explain the interaction of light with metals and dielectrics, which are the two material categories used for the nanoantennas in this thesis. In order to be able to characterize the nanoantennas, basic terminology of antenna theory is established. The working principle of both used nanoantenna types is deduced from an analog antenna from radio and microwave technology. The final part of the chapter deals with the fundamentals of quantum dots that are used as the active part of the nanoantennas.

2.1 Light-Matter Interaction

2.1.1 Maxwell's Equations

In the 1860s James Clerk Maxwell reviewed the equations known at that time, which described the properties of electric and magnetic fields [56]. Coulomb's and Ampère's law describe the interaction between charges or currents via fields. They and the law of absecence of sources in magnetic fields are inherently static. Only Faraday's law had a time component relating temporal change in magnetic and the rotation of electric fields. Maxwell generalized the current with a displacement current, describing temporal change of the electric field. With this supplement Ampère's law still contents the static law for the steady-state case, but in general relates temporal change in electric and the rotation of magnetic fields. He got a set of differential equations describing the behavior and interdependency of temporal varying electric $\mathbf{E}(\mathbf{r},t)$ and magnetic fields $\mathbf{B}(\mathbf{r},t)$ [57]:

$$\begin{aligned} \operatorname{div}\mathbf{D} &= \rho \quad , & \operatorname{rot}\mathbf{H} &= \mathbf{j} + \frac{\mathrm{d}\mathbf{D}}{\mathrm{d}t} \quad , \\ \operatorname{div}\mathbf{B} &= 0 \quad , & \operatorname{rot}\mathbf{E} &= -\frac{\mathrm{d}\mathbf{B}}{\mathrm{d}t} \quad . \end{aligned} \tag{2.1}$$

Together with the Lorentz force law and Newton's second axiom these equations give a complete description of the classical interaction of charged particles and electromagnetic fields. In this macroscopic form only free charge densities ρ and free current densities $\mathbf{j}$ are treated. The displacement field is denoted by $\mathbf{D}(\mathbf{r},t)$ and the magnetizing field by $\mathbf{H}(\mathbf{r},t)$.

These fields are connected by the polarization $\mathbf{P}(\mathbf{r},t)$ and the magnetization $\mathbf{M}(\mathbf{r},t)$, which state the density of electric and magnetic dipole moments in material:

$$\mathbf{D}(\mathbf{r},t) = \varepsilon_0 \mathbf{E}(\mathbf{r},t) + \mathbf{P}(\mathbf{r},t) \quad , \tag{2.2}$$

$$\mathbf{H}(\mathbf{r},t) = \frac{1}{\mu_0}\mathbf{B}(\mathbf{r},t) - \mathbf{M}(\mathbf{r},t) \quad . \tag{2.3}$$

The vacuum permittivity and permeability are denoted by ε_0 and μ_0, respectively.

Often it is useful to remove the explicit time dependence in the equations. In situations with no boundary surfaces, this is possible by a Fourier transformation of vectorial $\mathbf{\Psi}$ and scalar functions s with respect to the frequency ω [57]:

$$\begin{aligned} \mathbf{\Psi}(\mathbf{x},t) &= \frac{1}{2\pi}\int_{-\infty}^{\infty} \mathbf{\Psi}(\mathbf{x},\omega) \quad \mathrm{e}^{-\mathrm{i}\omega t}\mathrm{d}\omega \quad , \\ s(\mathbf{x},t) &= \frac{1}{2\pi}\int_{-\infty}^{\infty} s(\mathbf{x},\omega) \quad \mathrm{e}^{-\mathrm{i}\omega t}\mathrm{d}\omega \quad , \end{aligned} \tag{2.4}$$

and the inverse transform:

$$\begin{aligned} \mathbf{\Psi}(\mathbf{x},\omega) &= \int_{-\infty}^{\infty} \mathbf{\Psi}(\mathbf{x},t) \quad \mathrm{e}^{\mathrm{i}\omega t}\mathrm{d}t \quad , \\ s(\mathbf{x},\omega) &= \int_{-\infty}^{\infty} s(\mathbf{x},t) \quad \mathrm{e}^{\mathrm{i}\omega t}\mathrm{d}t \quad . \end{aligned} \tag{2.5}$$

Isotropic and linear media, as investigated in this thesis, are described by constitutive equations:

$$\mathbf{D}(\mathbf{r},\omega) = \varepsilon_0 \varepsilon(\omega)\mathbf{E}(\mathbf{r},\omega) \quad , \tag{2.6}$$

$$\mathbf{H}(\mathbf{r},\omega) = \frac{1}{\mu_0 \mu(\omega)}\mathbf{B}(\mathbf{r},\omega) \quad , \tag{2.7}$$

with $\varepsilon(\omega) = \varepsilon_1(\omega) + \mathrm{i}\varepsilon_2(\omega)$ the relative permittivity (or dielectric function) and $\mu(\omega)$ the relative permeability of the material as a function of the frequency ω. These two material properties describe the response of a material to an electromagnetic field.

Wave equations

Arguably, the most famous derivation of Maxwell's equations are the wave equations.

If an isotropic, linear medium and no free currents or charges are assumed, Maxwell's equations read:

$$\begin{aligned} \operatorname{div}\mathbf{E} &= 0 \quad , & \operatorname{rot}\mathbf{B} &= -\mathrm{i}\omega\mu_0\mu(\omega)\varepsilon_0\varepsilon(\omega)\mathbf{E} \quad , \\ \operatorname{div}\mathbf{B} &= 0 \quad , & \operatorname{rot}\mathbf{E} &= \mathrm{i}\omega\mathbf{B} \quad . \end{aligned} \tag{2.8}$$

Here, the derivatives with respect to time have been transformed to the frequency domain ($\frac{\mathrm{d}}{\mathrm{d}t} \rightarrow -\omega t$). The phase velocity is defined as $v_\mathrm{p} = (\mu_0\mu(\omega)\varepsilon_0\varepsilon(\omega))^{-1/2}$. Now the rotor of the equations is taken and the identity

$$\operatorname{rot}(\operatorname{rot}(\mathbf{\Psi})) = \operatorname{grad}(\operatorname{div}(\mathbf{\Psi})) - \Delta\mathbf{\Psi} \quad , \tag{2.9}$$

is used to get the wave equations for the electric and magnetic field:

$$\left(\frac{\omega^2}{v_\mathrm{p}^2} - \Delta\right)\mathbf{E} = 0 \quad , \tag{2.10}$$

$$\left(\frac{\omega^2}{v_\mathrm{p}^2} - \Delta\right)\mathbf{B} = 0 \quad . \tag{2.11}$$

Since the equations are symmetric regarding $\mathbf{E}$ and $\mathbf{B}$, in the calculations $\mathbf{\Psi}$ is used, where substitution of both fields is suitable. The wave equations are Helmholtz equations of the form

$$\left(\hat{n}^2 k_0^2 + \Delta\right)\mathbf{\Psi} = 0 \quad , \tag{2.12}$$

with the wavenumber in vacuum $k_0 = \omega/c$, the speed of light in vacuum c and the complex refractive index $\hat{n}$.

Refractive index and extinction coefficient

In natural materials the magnetic permeability for optical frequencies can be assumed to be 1. There is a simple relationship between the macroscopic optical properties refractive index n, extinction coefficient κ and the dielectric function:

$$\hat{n} = n + \mathrm{i}\kappa = \sqrt{\varepsilon} \quad , \tag{2.13}$$

$$n = \sqrt{\frac{1}{2}\left(\sqrt{\varepsilon_1^2 + \varepsilon_2^2} + \varepsilon_1\right)} \quad , \tag{2.14}$$

$$\kappa = \sqrt{\frac{1}{2}\left(\sqrt{\varepsilon_1^2 + \varepsilon_2^2} - \varepsilon_1\right)} \quad . \tag{2.15}$$

A suitable material model predicting the dielectric function is needed to conclude optical properties of a material.

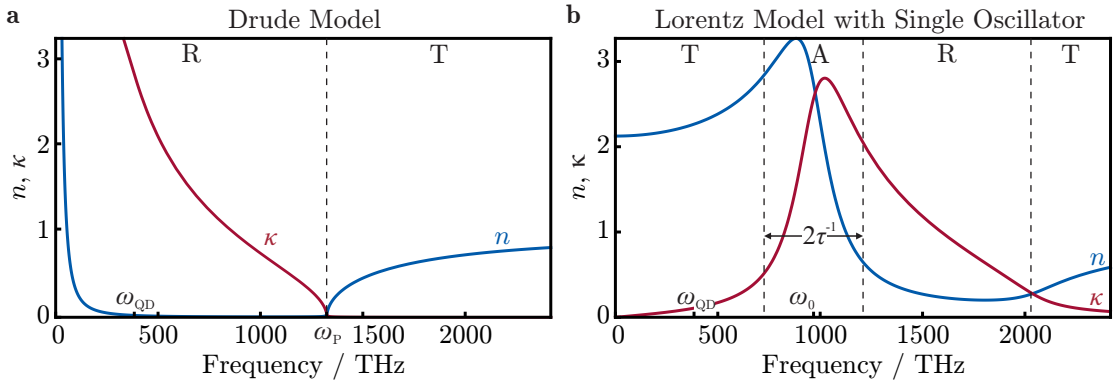

Figure 2.1: Spectral dependencies of n and κ for the Drude model and the Lorentz model with a single oscillator. The prime operating frequency of this thesis is denoted by ω_{QD}. **a** In the Drude model for metals two regions can be identified: primarily reflecting (R) in the near infrared regime and a primarily transmitting (T) for $\omega > \omega_{\mathrm{P}}$. **b** In the Lorentz model for dielectrics four regions can be identified: transparency because of neglectable absorption for frequencies smaller than ω_0 (T); absorption around the oscillators frequency (A); the following regions (R) and (T) resemble the same behavior as a Drude metal just for higher frequencies.

2.1.2 The Drude Model

The model named after the German physicist Paul Drude aims to describe electrical transport in metals by a kinetic theory. He treated the motion of electrons classically as a gas of free particles in a box which undergo collisions after an average time τ. Paul Drude published the model in 1900 [58]. Despite its simplicity, it is still used to some extend today [43], since it yields a valid expression for the electrical permittivity $\varepsilon(\omega)$ at least for sufficiently low frequencies [59]. The electrons surrounding the ionic crystal are thought to be gas-like, since in absence of an electric field, they behave as gas particles in a box. The model takes two forces on the electrons into account: They are accelerated by the electric part of the Lorentz force

$$\mathbf{F}_{\mathrm{el}} = -\mathfrak{e}\mathbf{E} \quad , \tag{2.16}$$

with the elementary charge $\mathfrak{e}$ and decelerated by a friction like force caused by collisions with the ions:

$$\mathbf{F}_{\mathrm{col}} = \frac{m_{\mathrm{e}}}{\tau}\dot{\mathbf{x}} \quad , \tag{2.17}$$

where $\dot{\mathbf{x}}$ is the electron velocity. Thus, the equation of motion reads:

$$m_{\mathrm{e}}\ddot{\mathbf{x}} + \frac{m_{\mathrm{e}}}{\tau}\dot{\mathbf{x}} = \mathfrak{e}\mathbf{E} \quad . \tag{2.18}$$

In the case of an impinging harmonic light field, the time dependency of the electric field can be separated $\mathbf{E} = \mathbf{E}_0 \mathrm{e}^{-\mathrm{i}\omega t}$. A solution to this differential equation representing a periodic motion with the ansatz $\mathbf{x}(t) = \mathbf{x}_0 \mathrm{e}^{-\mathrm{i}\omega t}$ is:

$$\mathbf{x}_0 = -\frac{\mathfrak{e}}{m_\mathrm{e}\left(\omega^2 + \mathrm{i}\tau^{-1}\omega\right)}\mathbf{E}_0 \quad . \tag{2.19}$$

At this point the polarization caused by the electrons is investigated with a vanishing free current density, since this leads directly to the complex permittivity. An equivalent treatment would be to assume a vanishing polarization and calculate the complex conductivity. Calculating the wave equations from Maxwell's equations for both assumptions and then comparing the result yields a conversion between the two expressions. Assuming, that the number density of free electrons is N_e, the polarization reads:

$$\mathbf{P} = -N_\mathrm{e}\mathfrak{e}\mathbf{x}_0 = \frac{N_\mathrm{e}\mathfrak{e}^2}{m_\mathrm{e}\left(\omega^2 + \mathrm{i}\tau^{-1}\omega\right)}\mathbf{E}_0 \quad . \tag{2.20}$$

The plasma frequency is defined as $\omega_\mathrm{P}^2 = N_\mathrm{e}\mathfrak{e}^2/(m_\mathrm{e}\varepsilon_0)$ such that comparing with eq. (2.2) and eq. (2.6) yields:

$$\varepsilon_\mathrm{D}(\omega) = 1 - \frac{\omega_\mathrm{P}^2}{\omega^2 + \mathrm{i}\tau^{-1}\omega} = \varepsilon_{\mathrm{D},1} + \mathrm{i}\varepsilon_{\mathrm{D},2} \quad , \tag{2.21}$$

$$= 1 - \frac{\omega_\mathrm{P}^2}{\left(\omega^2 + \tau^{-2}\right)} + \mathrm{i}\frac{\tau^{-1}\omega_\mathrm{P}^2}{\omega\left(\omega^2 + \tau^{-2}\right)} \quad . \tag{2.22}$$

The relaxation time for noble metals at optical frequencies is typically in the order of 10 fs to 1 ps [10, 12, 60], so that $\omega \gg \tau^{-1}$. Their plasma frequency is usually in the blue and ultraviolet regime [61, 62]. For frequencies below ω_p, the model gives a positive imaginary part of the dielectric function and a negative real part: The electrons are not in phase with the driving field, which is a good description of real metals and their high reflectivity. In the near infrared, especially around the operating frequency of the experiments in this thesis ($\approx 400\,\mathrm{THz} \mathrel{\widehat{=}} 750\,\mathrm{nm}$) the qualitative behavior of metals is described quite well by the Drude Model [15]. The refractive index and absorption coefficient as calculated from the model (eq. (2.14) and (2.15)) can be seen in Fig. 2.1.a.

2.1.3 Lorentz Oscillator Model

The Drude model describes the qualitative behavior of the dielectric function of metals in the infrared part of the spectrum quite well [15]. However, it fails to describe insulators or dielectric materials. Moreover, it becomes apparent that for higher frequencies even for metals the model needs extensions to describe reality.

The model is restricted to conduction electrons, which do not interact with each other or the ionic crystal apart from elastic collision. In reality interband transitions occur, where bound electrons can react to the electromagnetic field. For example, it is well known that the imaginary part of gold in the green part of the spectrum ($\lambda \approx 550\,\mathrm{nm}$) is underestimated dramatically by the Drude Model [10]. Here, the energy of the photons is sufficient to excite electrons from lower, bound bands to the conduction band [12]. This additional possibility for the electromagnetic field to interact with matter can be described by damped harmonic oscillators. Those oscillators were introduced by the Dutch physicist Hendrik Lorentz in 1905 [63] as an addition to the Drude model, but can describe the behavior of dielectrics as well. The results from this classical theory are formally identical to those of a quantum-mechanical treatment [64], even though the interpretation differs. This might be a reason why the model is still in use today [65, 66]. The oscillators have resonance frequency $\omega_0 = \sqrt{s_\mathrm{L}/\tilde{m}_\mathrm{e}}$ such that the equation of motion for the bound electrons reads [64]:

$$\tilde{m}_\mathrm{e}\ddot{\mathbf{x}} + \tilde{m}_\mathrm{e}\gamma_\mathrm{L}\dot{\mathbf{x}} + s_\mathrm{L}\mathbf{x} = \mathfrak{e}\mathbf{E} \quad , \tag{2.23}$$

where $\tilde{m}_\mathrm{e}$ is the effective mass of the bound electron, γ the damping constant and s_L the restoring spring constant. With the same argumentation as for the Drude model, the dielectric function of the Lorentz model is derived to be:

$$\varepsilon_\mathrm{L}(\omega) = 1 + \frac{\tilde{\omega}_\mathrm{P}^2}{(\omega_0^2 - \omega^2) - \mathrm{i}\gamma\omega} = \varepsilon_{\mathrm{L},1} + \mathrm{i}\varepsilon_{\mathrm{L},2} \quad , \tag{2.24}$$

$$= 1 + \frac{\tilde{\omega}_\mathrm{P}^2\,(\omega_0^2 - \omega^2)}{(\omega_0^2 - \omega^2)^2 + \gamma^2\omega^2} + \mathrm{i}\frac{\gamma\tilde{\omega}_\mathrm{P}^2\omega}{(\omega_0^2 - \omega^2)^2 + \gamma^2\omega^2} \quad , \tag{2.25}$$

the plasma frequency for the bound electrons is defined $\tilde{\omega}_\mathrm{P}^2 = \tilde{N}\mathfrak{e}^2/(\tilde{m}_\mathrm{e}\varepsilon_0)$ in analogy to the Drude model, but depends on the effective mass and number density $\tilde{N}$ of the bound electrons. The refractive index and absorption coefficient as calculate for a single Lorentz oscillator (eq. (2.14) and (2.15)) can be seen in Fig. 2.1.b. A Lorentz oscillator with a high damping constant is a good description of the tendency of all solids and liquids to absorb strongly in the ultraviolet regime. Here, electric excitations occur, since the photon energy matches energy differences between filled and empty electron bands. The behavior in the near infrared regime is governed by this resonance: the dielectric's transparency is represented by the neglectable absorption coefficient. Additionally, the Lorentz oscillator approach can be used to model other excitations, e.g., lattice vibrations. The bound electrons' contribution to the dielectric function of a real material can be represented by the integrated effect of multiple different oscillators, one kind for each excitation. Moreover, the whole Drude model could be obtained by using the Lorentz model with a vanishing restoring constant [62]. This is the reason, why the reflecting and transmitting regions of the pure Drude model as labeled in Fig. 2.1.a find a

resemblance in the regions (R) and (T) of the Lorentz oscillator model just for higher frequencies.

In order to get a good description of the dielectric function of a real metal the Drude model and the Lorentz model for a series of transition (j) are combined:

$$\begin{aligned}\varepsilon(\omega) &= \varepsilon_\infty + \quad \varepsilon_\mathrm{D} \quad + \sum_j \varepsilon_{\mathrm{P},j} \\ &= \varepsilon_\infty - \frac{\omega_\mathrm{P}^2}{\omega^2 + \mathrm{i}\tau^{-1}\omega} + \sum_j \frac{\tilde{\omega}_{\mathrm{P},j}^2}{\left(\omega_{0,j}^2 - \omega^2\right) - \mathrm{i}\gamma_j\omega} \quad .\end{aligned} \tag{2.26}$$

The offset ε_∞ accounts for the effect that usually not all the higher-energy interband transitions are included in the sum [10]. Those equations are in practice often fitted to measured values [67] in order to extract the parameters.

With the Lorentz and the Drude model the behavior of the materials used in this thesis can be understood qualitatively. The high absorption and reflectivity of metals in the near infrared regime is governed by the free electron gas dispersion, while the transparency and slow dispersion of dielectrics stem from the lack of unbound electrons.

2.2 Antennas for Light

2.2.1 General Antenna Properties

Since a lot of progress in nanophotonics is based on copying and scaling down devices from radio and microwave technology, similar concepts and terminology can be used. Thus, the core terms and concepts of antenna technology are introduced in this section.

In a general definition antennas are transitional structures, which interconverse between localized near-field excitements and radiative far-field modes [68]. Regardless of their operating principle, universal parameters are defined to characterize their performance.

Radiation Pattern

A radiation pattern is a representation of the radiation properties of the antenna as a function of spatial coordinates. The represented properties can be power flux density, radiation intensity, field strength, directivity, phase or polarization [69]. A radiation pattern is usually determined in the far-field region and given by standard directional coordinates (spherical coordinates, restricted to a sphere's surface with

radius r) with the polar angle θ and the azimuthal angle φ:

$$x = \sin(\theta)\cos(\varphi)\, r \quad , \tag{2.27}$$

$$y = \sin(\theta)\sin(\varphi)\, r \quad , \tag{2.28}$$

$$z = \cos(\theta)\, r \quad . \tag{2.29}$$

This thesis covers intensity measurements, so that relevant radiation patterns are power, intensity or directivity ones. The terms power and intensity can often be interchanged here, since the form of both patterns is the same. An antenna's power pattern exhibits radiation lobes, which are defined as *portions of the radiation pattern bounded by regions of relatively weak radiation intensity* [69]. The main lobe is the strongest of those and is usually accompanied by smaller side lobes. The antenna is designed such that the main lobe points in the desired transmitting direction.

Hertzian Dipole

The Hertzian dipole is introduced as an approximation for microscopic emitters and an important tool in theoretical treatments. It is thought of as a thin conductor with uniform current over its very short or even infinitesimal length δL. The current oscillates with frequency ω in time ($I = I_0 \mathrm{e}^{\mathrm{i}\omega t}$). When the dipole is in the origin of the coordinate system oriented along the z-axis, the electric far field of the Hertzian dipole is given by [69]:

$$E_0(\theta, r) = \mathrm{i}\frac{I_0 \delta L k}{4\pi r}\mathrm{e}^{-\mathrm{i}kr}\sin(\theta)\ \hat{\mathbf{e}}_\theta \quad , \tag{2.30}$$

with the wavenumber $k = \omega/c$ and r the distance to the origin. The electric far field has only θ-components and is symmetric around the antenna axis.

Directivity

The directivity is a parameter that describes the ability of an antenna to confine its radiation to a solid angle. There exist several definitions. Most useful here is to define the directivity $D(\theta, \varphi)$ as the intensity $I(\theta, \varphi)$ normalized to the average intensity I_{av}:

$$D(\theta, \varphi) = \frac{I(\theta, \varphi)}{I_{\mathrm{av}}} \quad , \tag{2.31}$$

Sometimes the term directivity is used to describe the maximal directivity D_0 [70]:

$$D_0 = \frac{I_{\max}}{I_{\mathrm{av}}} \quad . \tag{2.32}$$

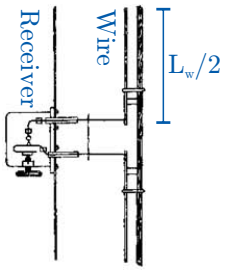

Figure 2.2: Original figure of thin wire antenna as used by Heinrich Hertz [71]. Blue labels added.

usually the distinction can be made by context.

Since the directivity is a quantity of ratio, it is sometimes measured in decibel. Per definition the directivity of an antenna can not be lower than 1 ($= 0\,\mathrm{dB}$), and the value 1 is only reached by the non-existing idealized perfect isotropic antenna.

To determine the directivity, measurements of the radiated power over the whole sphere have to be performed, since it depends on the average intensity. However, there are several approximations for situations, where such a measurement can not be achieved [70]. They rely on measurements of the main lobe size or restrict the intensity averaging to just the measurable directions. To be accurate, reasonable assumptions regarding the not measured part of the field have to be made. The beam direction is the direction of the maximal intensity and thus coincides with the direction of maximal directivity.

Front-to-Back Ratio

The front-to-back ratio (FBR) can be used to quantify an antenna's performance, when only one hemisphere of its radiation pattern is known. Without loss of generality, the hemisphere is assumed to be centered around $\theta = 0°$. The FBR is then defined as the intensity ratio between the direction of maximal intensity $(\theta_{\max},\ \varphi_{\max})$ and the opposing point $(\theta_{\max},\ \varphi_{\max} + 180°)$ [25]. The FBR has the advantage over the use of directivity that it is properly defined even without knowledge of the whole pattern. The trade-off is that the FBR is only a meaningful figure of merit for specific radiation patterns: There are patterns that are obviously highly directive, but give a small FBR and vice versa. Antennas of similar pattern, however, can be compared with the FBR.

2.2.2 Resonant and Traveling-Wave Antennas

For the scope of this thesis it is useful to categorize antennas into two large groups based on their functional principle: (i) resonant antennas and (ii) nonresonant

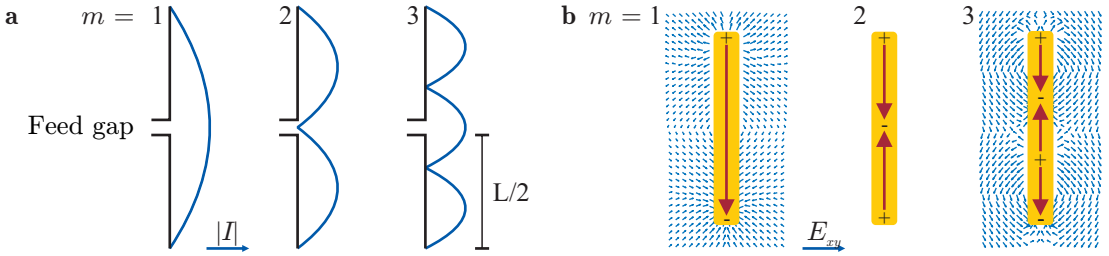

Figure 2.3: **a** Schematic representation of the first three modes of a thin linear wire antenna with a feed gap. **b** Schematic representation of the charge separation of the first three modes of a plasmonic nanoantenna. The red arrows represent the electric dipole moment. For the first and third mode, the calculated electric field in the plane is shown.

traveling-wave antennas. The aim of the following section is to explain the operating principle of both types of nanoantennas used in this thesis: gold rod nanoantennas representing the resonant group and dielectric leaky-wave nanoantennas as nonresonant devices. To explain the technological, terminological and historical context in both cases, first an analogue device from microwave technology is introduced.

2.2.3 From Hertz' Antenna to Rod Nanoantennas

When antennas are discussed in academic and non-academic context, resonant antennas are the commonly thought of type. This might be due to the fact that a lot of the antenna technology in our every day life is based on standing waves, e.g., FM broadcast antennas or the antennas connecting our mobile devices to wireless local area networks. In fact, the first antenna ever for electromagnetic radiation was a resonant one. Heinrich Hertz used a copper wire with a spark gap in the late 19th century in his pioneering investigations of radio waves. He observed nodes and antinodes on the metallic wire and found that the waves on it were essentially undisturbed, when the wire was cut at a node [72]; a clear sign for a standing wave pattern. Figure 2.2 shows Hertz' schematic of an antenna that he used to receive electromagnetic waves in his later experiments.

The concept of a conductor supporting a standing wave of charge carriers is still at the core of complexer resonant antennas used today: The antenna designs feature a characteristic length L_c, which is directly related to the operating wavelength λ_{op} [73]. A thin linear wire as used by Hertz is one of the simplest antenna forms. Here, a linear relationship between the wire length L_w and the operating wavelength can be derived: The antenna supports a sinusoidal current distribution, when the wire is thin compared to the wavelength, i.e., the diameter of the wire

is less than one hundredth of the wavelength [70]. With the boundary condition of vanishing currents at the ends of the wire, it is obvious that there are only a discrete number of allowed modes indexed by integer m:

$$L_{\mathrm{w}} = \frac{m}{2}\lambda_{\mathrm{op}} \quad . \tag{2.33}$$

This relationship remains true for the specific antenna type with a feed gap between two $L/2$ wires, as long as the gap is impedance matched [73]. The first three modes of a thin linear wire antenna are sketched in Fig. 2.3.a.

Plasmonic Nanoantennas

The definition for antennas given before includes the notion of localized near-field excitements. Antennas can be used to couple far-field modes to those local effects. Classical optical devices, e.g., lenses and mirrors, control the far field of light. Antennas can be seen as bridges to the utilization of near fields. Those local effects are one of the reasons, why antennas in the optical range are such widely researched tools: Effects of the near field are not restricted by the diffraction limit. Thus, resolutions beyond Abbe's limit are possible and give rise to hot spots of enhanced intensities [15].

Exactly as their radio and microwave counterparts, plasmonic nanoantennas rely on a resonance effect of the electromagnetic field in a metallic structure. In a metallic rod nanoantenna an impinging electromagnetic wave, i.e., light, induces charge separation as sketched in Fig. 2.3.b. This leads to very similar possible antenna modes $\frac{m}{2}\lambda_{\mathrm{eff}}$ as in the radio-wave context [74]. Here however, an effective wavelength λ_{eff} becomes necessary to use: As discussed in Section 2.1.2, a drude metal does not reflect light perfectly anymore once the frequency approaches the plasma frequency, i.e., at optical frequencies. The radiation penetrates the metal and gives rise to oscillations of the electron gas. For rod antennas a simple scaling law for the effective wavelength can be derived [73]:

$$\lambda_{\mathrm{eff}} = p_1 + p_2\frac{\lambda}{\lambda_{\mathrm{P}}} \quad , \tag{2.34}$$

with the plasma wavelength λ_{P} and two parameters p_1 and p_2 depending on the antenna dimension, the dielectric properties and the order of the investigated mode. Thus, for a given mode m, the resonance wavelength scales linearly with antenna length.

Indeed, this behavior is reproduced by numerical calculations: Figure 2.4 shows the extinction cross sections of a set of gold rod nanoantennas with lengths ranging from 80 nm to 320 nm, calculated with a finite element method (FEM). As expected the maximum's position of the antenna's cross section increases with the antenna

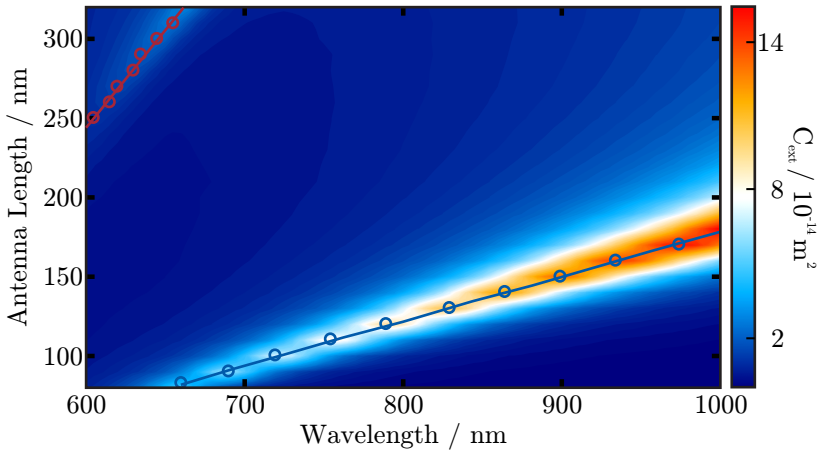

Figure 2.4: Numerically calculated extinction cross section of gold rod nanoantennas. As expected, the maxima of the fundamental resonance (blue circles) shift to longer wavelengths. The blue line is a linear regression to the maximum positions. For the longest antennas the third order maxima are visible (red cricles). The linear regression shown in red has a higher slope.

length. A linear regression to the maximum positions and comparison to eq. (2.34) yields:

$$L = \frac{1}{2}\lambda_{\text{eff}} = \frac{1}{2}\left(p_1 + p_2\frac{\lambda}{\lambda_{\text{P}}}\right) = \frac{1}{2}\left(-210\,\text{nm} + 0.566\cdot\lambda\right) \quad . \tag{2.35}$$

For the longest antennas a new maximum at small wavelength arises. This is the third-order resonance with $m = 3$. It shifts to higher frequencies for longer antennas as well. The slope of the $m = 3$ regression line is 4.4 times larger than the fundamental mode's. The discrepancy to a factor of 3 arises from the fact that the derivation of eq. (2.34) is based on the fundamental ($m = 1$) mode in rod antennas. Additionally, the numerical calculations were performed for rectangular cross sections, while the analytical model assumes a circular shape. A final distinction is the fact that a pure Drude metal is assumed for the scaling law, and thus, the occurring interband transition at $\lambda \approx 500\,\text{nm}$ will cause perturbations especially for smaller wavelengths [73].

In the calculated cross section there are no second order resonances visible. The simulated far-field excitation with plane waves under normal incident can not excite all antenna modes. In Fig. 2.3 the standing wave profiles of a thin wire antenna and a rod nanoantenna are compared. For a rod antenna of 300 nm length the calculated electric fields are shown.

The current density distribution of the m-th plasmonic mode of the rod antenna is a simple standing wave with nodes at the ends and $m-1$ nodes distributed along

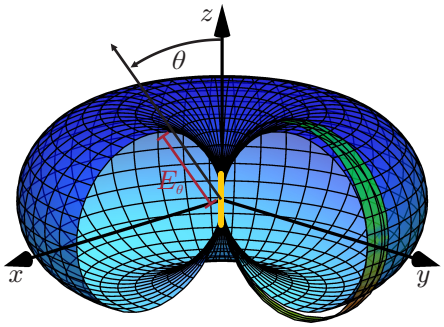

Figure 2.5: The electric far-field pattern of a $\lambda/2$ antenna oriented along the z-axis (blue). The only non-zero component of the electric field is E_θ. For comparison a slice of the pattern of a Hertzian dipole is shown in green. Both patterns are rotational symmetric in respect to the z-axis.

the rod. The locations of the current density nodes coincide with the anti-nodes of the charge density oscillation. Hence, the fundamental mode ($m = 1$) exhibits anti-nodes of the charge density oscillation at the two ends. The corresponding electric dipole moment can be represented by an arrow from one charge density anti-node to the other. The third order mode $m = 3$ has two additional anti-nodes along the rod. Thus, there are three subsidiary electric dipole moments, two pointing in the same and the third in opposite direction. The overall dipole moment is the vector sum of the three. The second mode $m = 2$ is not visible in our calculations, because it has a vanishing dipole moment. The subsidiary dipole moments have the same length and necessarily point in opposite directions. In conclusion, it can be inducted that only modes with even m exhibit a non-vanishing dipole moment. Modes with small dipole moments are considered to be optically dark, since thy can not be exited with standard far-field methods [12, 39].

The far-field pattern of the $\lambda/2$ antenna can be calculated analytically. If the antenna axis coincidences with the z axis and the polar angle θ is measured from this axis, the pattern is independent of the azimuthal angle φ. It is important to note that the electric field always points in $\hat{\mathbf{e}}_\theta$-direction [70]. Thus, the emitted radiation is p-polarized. The resulting form factor for the electrical far field of a $\lambda/2$ antenna is:

$$E_\theta(\theta) \propto \frac{\cos\left(\pi/2\cos(\theta)\right)}{\sin\theta} \quad . \tag{2.36}$$

The electric far-field pattern of the antenna is shown and compared to that of a Hertzian dipole (Section 2.2.1) in Fig. 2.5 . The directivity of the antenna is only slightly larger than that of an idealized Hertzian dipole.

In conclusion, rod metallic nanoantennas exhibit plasmonic resonances with wavelengths, which scale linearly with the antenna length. Their radiation is not

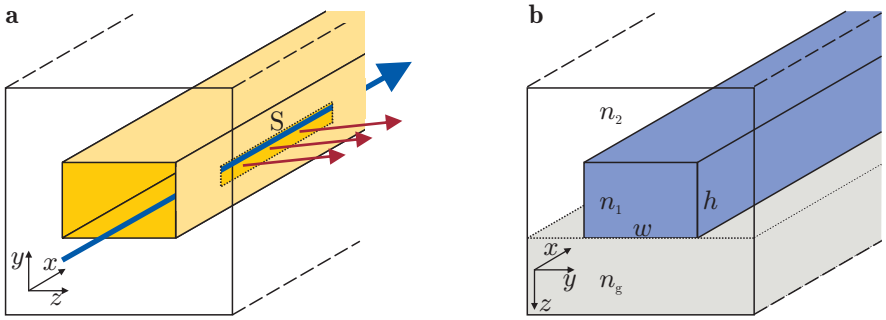

Figure 2.6: Sketches of two waveguides for different spectral regimes. **a** A hollow rectangular metallic waveguide for the microwave regime. The blue arrow indicates the guided mode with propagation constant β. To get a leaky-wave antenna, a slit (S) has to be introduced and $\beta < k_0$. **b** A dielectric waveguide for optical frequencies. The mode is guided by a dielectric with refractive index n_1 in x-direction. To get a leaky-wave antenna, a material with the correct refractive index has to be introduced (gray) such that $\beta < k_g$. In both cases the antennas radiate in the positive quadrant of the z-x-plane.

particular directive, but highly polarized.

2.2.4 From Waveguides to Leaky-Wave Antennas

Besides antennas that rely on resonances, there is a whole category of antennas that are based on traveling, guided waves. The discussions in this thesis will focus on leaky-wave antennas – a subset of traveling-wave antennas. A leaky-wave antenna consists of a waveguide with a leaking mechanism, e.g., a hollow metallic waveguide with a slit. The antenna radiation is formed by the combined waves leaked over the length of the guiding structure [44]. This section first introduces a leaky-wave antenna for the microwave regime to develop the concept and terminology. In a second step the changes that have to be made when scaling the device down to optical frequencies are investigated.

Microwave Leaky-Wave Antennas

Leaky-wave antennas have been employed to control radio and microwaves since the first half of the 20th century [44, 75] and are especially useful for low-profile installations [68]. Since the waveguide is the defining feature of leaky-wave antennas of any kind, this section will shortly recapitulate the basic principles of waveguides.

In the radio and microwave regime, the earliest examples were realized as hollow rectangular metallic waveguides as sketched in Fig. 2.6.a, where radiation is confined in y- and z-direction by reflection at the metal surface. Since the cross section stays constant in direction of propagation the ansatz $\mathbf{\Psi}(x, y, z) = \mathbf{\Psi}(y, z)\mathrm{e}^{\mathrm{i}\beta x}$ can be used such that the Helmoltz equation (2.12) for this system in vacuum reduces to:

$$\left[\frac{\partial^2}{\partial y^2} + \frac{\partial^2}{\partial z^2} + \left(k_0^2 - \beta^2\right)\right] \mathbf{\Psi} = 0 \quad . \tag{2.37}$$

The solutions for this equation together with the boundary conditions, give rise to two different supported types of modes, transverse magnetic (TM) and transverse electric (TE) [57]:

$$\begin{array}{lll} & \mathbf{r} \text{ inside WG} & \mathbf{r} \text{ at boundary} \\ \text{TM:} & B_x(\mathbf{r}) = 0 & E_x(\mathbf{r}) = 0 \\ \text{TE:} & E_x(\mathbf{r}) = 0 & \dfrac{\partial B_x}{\partial \tilde{n}}(\mathbf{r}) = 0 \end{array} \tag{2.38}$$

Here $\partial/\partial\tilde{n}$ is the normal derivative at a point on the surface.

In both cases (TM and TE), due to the confinement in y- and z-direction, the number of modes is discrete. Thus, the modes are usually characterized by two integers, giving the number of zeros in the field distribution in the respective direction. For each mode the propagation constant β is defined by $n^2k_0^2 = k_y^2 + k_z^2 + \beta^2$, with the discretized wavenumbers k_y and k_z.

The propagation constant β of the modes is always smaller than the free space value k_0 and thus the phase velocity of the guided modes is higher than the infinite space value [57]. To operate the waveguide as a leaky wave antenna, a slit (S) in the metal parallel to the traveling direction is introduced. Through this slit radiation leaks out and it forms an antenna aperture [44].

Optical Leaky-Wave Antennas

In optics, light can be guided by dielectric waveguides, which rely on total internal reflection to establish confinement in two dimensions [76]. Hollow metallic waveguide analogs are only used in special condition in the optical spectrum anymore. So called metal-insulator-metal waveguides are foreseen for use in on-chip optical devices, but suffer from small propagation length [14]. As discussed in Section 2.1.2, metals are no perfect conductors here. Additionally, the fabrication of nanoscale hollow metallic waveguides is challenging. However, the fundamental concepts and arising modes in dielectric and metallic waveguide are similar in the microwave and optical frequency regime.

A dielectric waveguide with refarctive index n_1 with rectangular cross section is sketched in Fig. 2.6.b. To simplify the discussion, the dielectric is surrounded

by a homogeneous surrounding ($n_\mathrm{g} = n_2$). The Helmholtz equation (2.37) derived for the hollow metallic waveguide still applies, but since the fields are not confined inside the waveguide anymore, two equation for the different regions are needed [57]:

$$\begin{aligned} \text{Inside} \quad & \left[\frac{\partial^2}{\partial y^2} + \frac{\partial^2}{\partial z^2} + \left(n_1^2 k_0^2 - \beta^2\right)\right] \boldsymbol{\Psi} = 0 \quad , \\ \text{Outside} \quad & \left[\frac{\partial^2}{\partial y^2} + \frac{\partial^2}{\partial z^2} + \left(n_2^2 k_0^2 - \beta^2\right)\right] \boldsymbol{\Psi} = 0 \quad . \end{aligned} \tag{2.39}$$

The external fields must match the internal field at all boundary points, so that both equations have the same propagation constant β. Since the expected modes have to fall off exponentially outside the waveguide, the term $(n_2^2 k_0^2 - \beta^2)$ needs to be negative. Thus, the propagation constant of the mode β is larger than the wavenumber in the surrounding medium $n_2 k_0$. Additionally, with the same argument as for the hollow metallic waveguide, the propagation constant is larger than the wavenumber in the dielectric $n_2 k_0 < \beta < n_1 k_0$.

In this special geometry of a rectangular waveguide, the fields separate into TM and TE modes again. Note that this is not necessarily true in general for dielectric waveguides due to the more complex boundary conditions: continuity of normal components of $\boldsymbol{B}$ and $\boldsymbol{D}$ as well as tangential component of $\boldsymbol{E}$ and $\boldsymbol{H}$ [57, 76]. So like its microwave counterpart, a rectangular, dielectric waveguide supports a discrete number of modes, which can be separated regarding their polarization and the propagation constant β depending on the cross section of the waveguide.

To change the metallic waveguide to a leaky-wave antenna, a slit was introduced, where the radiation could leak out in a radiative free space mode ($\beta < k_0$). In analogy to that, a substrate with refractive index $n_\mathrm{g} \neq n_2$ touching the waveguide serves as a leak channel: if $\beta < n_\mathrm{g} k_0$ the leaked wave can couple to a radiating mode in the substrate. Now, the whole base of the waveguides forms the antenna aperture of the leaky-wave antenna. Both alterations, the introduction of the slit and the substrate, will influence the modes of the waveguides significantly such that a numerical evaluation of β is necessary.

Properties of Leaky-Wave Antennas

For the discussed cases of leaky-wave antennas with uniform cross sections along the guiding structure, β has to be larger than the wavenumber k_g in the medium in which the antenna emits. Otherwise the leaked wave could not couple to radiative modes. There are approaches to overcome that restriction, e.g., periodic structuring of the guiding structure [70]. However, those are not be covered by this thesis.

The beam direction of a leaky-wave antenna θ_{beam} measured from the surface normal of the guiding structure and the beamwidth can be estimated by [44]:

$$\sin\left(\theta_{\mathrm{beam}}\right) \approx \beta / k_{\mathrm{g}} \quad , \tag{2.40}$$

$$\Delta\theta \approx \frac{2\pi}{k_{\mathrm{g}} L \cos(\theta_{\mathrm{beam}})} \quad , \tag{2.41}$$

where $k_{\mathrm{g}} = n_{\mathrm{g}} k_0$ is the wavenumber in the medium, in which the antenna emits and L the antenna length. The complete radiation pattern in the far field can be obtained by solving the Fraunhofer diffraction integral of the aperture distribution [44]. Finite lengths of the waveguide as well as the radiation losses give rise to side lobes. The polarization of the radiation depends on the mode that is excited in the waveguide: TE and TM modes give rise to different field distributions at the antenna aperture. The propagation constant β and, hence, the beam direction can be controlled by designing the cross section of the guiding structure.

A main difference to resonant antennas is their broadband operation. As long as for a given frequency a propagating mode exists, there will be a directed beam with direction according to eq. (2.40). However, a different frequency will result in a change of the propagation constant β and thus the beam direction. In principle this behavior can be used to scan the antenna from broadside ($\theta_{\mathrm{beam}} = 0°$) to end-fire operation ($\theta_{\mathrm{beam}} = 90°$). The limits in reality depend heavily on the specific structure [44].

2.3 Quantum Dots

Both types of antennas used in this thesis – plasmonic rod nanoantennas and dielectric leaky-wave nanoantennas – are fed by the fluorescence of colloidal semiconductor quantum dots. Quantum dots are structures that confine the wave function of electrons and holes in three spatial dimension. Because of the energy spectrum arising from this confinement, they are often thought of as artificial atoms [78].

One application is their use as a dye with high quantum yield. The earliest technique to fabricate quantum dots was to grow them in glass, which then changed its color. In the 1930s the yellow and red color of some glasses was found to be caused by particles composed of cadmium sulphide and cadmium selenide [79]. Although the role of the size of the particles had not been identified, this work laid the foundation for development of sharp-cut color filter glasses in the 1960s [80]. In the 1980s the effect of the stoichiometry and size of the particles on the optical absorption spectra was discussed theoretically and measured in experiments [81, 82]. In Fig. 2.7 (adapted from [80]) the absorption spectra for CdSe nanoparticles of various sizes in a glass matrix are shown. The spectrum of the biggest particles

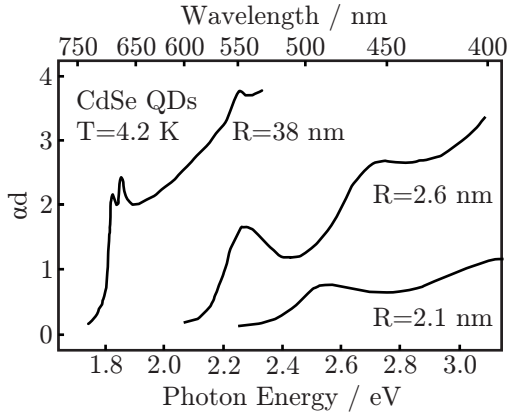

Figure 2.7: Spectra of linear absorption of CdSe nanocrystals with different radii R. Data from Ekimov et al. [77]. For particles of size $R = 38\,\text{nm}$. The absorption spectra resembles that of bulk material and its sharp absorption edge.

$R = 38\,\text{nm}$ resembles the bulk material with the steep band gap and multiple exciton states close by. The form of the absorption spectrum depends strongly on the particle size.

The following section discusses the effect of low dimensionality on electrons and then derives a relationship between band gap and particle size. The particular quantum dots used in this thesis are introduced in Section 3.2.1.

2.3.1 Density of States of Lower Dimensional Electron Gases

The interesting effects of quantum dots arise from their low dimensionality. It makes sense to discuss not only the 0-dimensional case of quantum dots, but to shortly investigate 3-, 2- and 1-dimensional systems (bulk, quantum well, quantum wire) as well to see how low-dimensional properties evolve. A lower dimensional system is experimentally achieved by restricting the accessible length in one dimension. Confining particles in a dimension gives rise to quantized confinement energies. As long as the next energy quanta can not be reached by the total energy E, the particle acts as being in a lower dimensional space. In the case of quantum dots, the electrons are confined in three dimension to the range of typically 1 nm to 100 nm [83].

The density of states $\mathcal{D}(E)$ of free electron gas system is characteristic for its dimensionality d. Clearly, a free electron gas approach is not suitable for a complete description of semiconductor systems. However, a qualitative understanding of emerging low-dimensional effects can be gained [83]. The density of states gives the

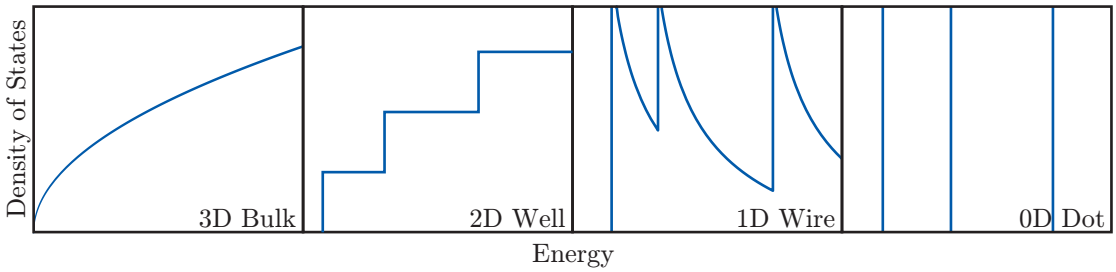

Figure 2.8: Density of states of a free electron gas of dimensionality in 0–3.

number of available modes per unit volume and particle energy. Note, that in this discussion the terms volume and sphere are used as the appropriate d-dimensional analog. The number of states $N(k)$ per crystal volume V_C to be reached by a particle with wavenumber k is:

$$N(k) = \frac{S^{(d)}(k)}{V_\mathrm{S}} \frac{1}{V_\mathrm{C}} \quad , \tag{2.42}$$

where V_S denotes the volume in reciprocal space occupied by one state and $S^{(d)}(k)$ the volume of a d-dimensional sphere. To calculate the number of states per energy, the dispersion needs to be considered:

$$E(\mathbf{k}) = \frac{\hbar^2 k}{2m_\mathrm{e}} |\mathbf{k}|^2 \qquad \Rightarrow \qquad \mathrm{d}E = \frac{\hbar^2 k}{m_\mathrm{e}} \mathrm{d}k \quad , \tag{2.43}$$

where the electron mass is denoted by m_e. The density of states as the number of states per unit volume and per energy interval is:

$$\mathcal{D}(E) = \frac{\mathrm{d}N}{\mathrm{d}E} = \frac{\mathrm{d}N}{\mathrm{d}k} \frac{\mathrm{d}k}{\mathrm{d}E} \quad . \tag{2.44}$$

In the $3-d$ confined dimensions, the energy spectrum is discrete. The available energy levels for the confined dimensions are denoted E_l, with l counting the energy levels. The density of states $\mathcal{D}^{(d)}$ for a free electron gas in dimension d is:

$$\begin{aligned}
\mathcal{D}^{(3)}(E) &= \frac{(2m_\mathrm{e})^{3/2}}{2\pi^2\hbar^3} && \mathrm{E}^{1/2} \quad , \\
\mathcal{D}^{(2)}(E) &= \frac{m_\mathrm{e}}{\pi\hbar^2 V_\mathrm{C}} && \sum_{E_\mathrm{l}<E} \Theta(E - E_\mathrm{l}) \quad , \\
\mathcal{D}^{(1)}(E) &= \frac{(2m_\mathrm{e})^{1/2}}{\pi\hbar V_\mathrm{C}} && \sum_{E_\mathrm{l}<E} (E - E_\mathrm{l})^{-1/2} \quad , \\
\mathcal{D}^{(0)}(E) &= \frac{2}{V_\mathrm{C}} && \sum_{E_\mathrm{l}<E} \delta(E - E_\mathrm{l}) \quad .
\end{aligned} \tag{2.45}$$

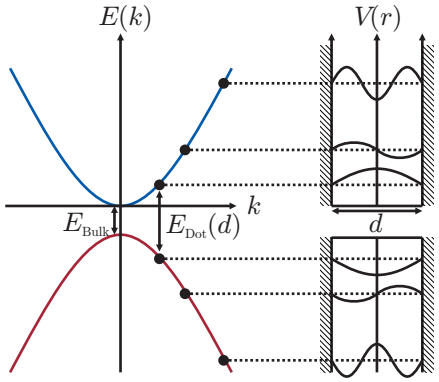

Figure 2.9: The discrete energy levels of electrons (holes) in quantum dots modeled as a sphere with infinite potential walls, lie on the blue parabola (red). The bulk energy gap E_{Bulk} is modified by the effects of the small size to E_{Dot} [78].

Here, the Heaviside step function is denoted by Θ and the Dirac delta function by δ. These results are sketched in Fig. 2.8: the density of states is more and more governed by the confinement energies. The 3D bulk density of states follows a simple square root law. In the 2D case (quantum well), the density of state is constant, but the density of states jumps every time the energy is high enough to excite the next state in the confined dimension. In the 1D case (quantum wire) $\mathcal{D}$ decreases with an inverse square root law and – similar to the quantum well – jumps as soon as the total energy is high enough for the next excited state in a confined dimension. Finally, the quantum dot density of states is discrete and only the jumps are left: the quantum dot has a dimensionality of 0 and is therefore described by a particle in a box model in all dimensions. This complete energy discretization supports the notion of artificial atoms.

2.3.2 Size Dependent Energy Gap

To extend the model of free electrons to semiconductors, the concept of the hole as a new charge carrier is introduced. A lot of semiconductor properties can be described by free electrons and holes moving on different energy bands (conduction and valence) seperated by an energy gap. The size of this gap is crucial for optical experiments, since it governs absorption and fluorescence processes. The size dependency of the gap in a quantum dot is estimated here.

The dispersion relation of holes and electrons at the edges of their band can be approximated by parabolas [78]. In the zero-dimensional case of a quantum dot, the discretized energy states still lie on those parabolas as sketched in Fig. 2.9. The size of the energy gap of a quantum dot can then be modeled by three components:

the bulk band gap E_{Bulk}, the confinement energy E_{C} and a Coulomb term E_{Coul}:

$$E_{\mathrm{Dot}} = E_{\mathrm{Bulk}} + E_{\mathrm{C}} + E_{\mathrm{Coul}} \quad . \tag{2.46}$$

To calculate the confinement energy, the shape of a quantum dot is modeled as a sphere of diameter d. The potential energy is zero inside the sphere and infinite on the walls. The lowest confinement energy E_1 of a particle with mass m in such a 3D box can be derived in spherical coordinates by separating the radial part and solving the Schrödinger equation:

$$E_1 = \frac{h^2}{2md^2} \quad . \tag{2.47}$$

In an optical experiment an electron-hole pair is generated, when the photon energy is large enough to excite an electron to the conduction band, leaving a hole in the valence band. Thus, any energy term needs to account for the confinement energy of holes and electrons. With the effective masses m_{e} and m_{h} of electron and hole, the reduced mass is:

$$\frac{1}{m^*} = \frac{1}{m_{\mathrm{h}}} + \frac{1}{m_{\mathrm{e}}} \quad , \tag{2.48}$$

and the sum of the two confinement energies simplifies to:

$$E_{\mathrm{C}} = E_1(e) + E_1(h) = \frac{h^2}{2m^*d^2} \quad . \tag{2.49}$$

The Coulomb term takes the fact into account that electron and hole attract each other. This attraction is shielded by the crystal. An estimate for the Coulomb term can be given as [78]:

$$E_{\mathrm{Coul}} = \frac{-1.8e^2}{2\pi\varepsilon\varepsilon_0 d} \quad . \tag{2.50}$$

In conclusion, an estimate for the energy gap of a semi conductor quantum dot is:

$$E_{\mathrm{Dot}} = E_{\mathrm{Bulk}} + \frac{h^2}{2m^*d^2} - \frac{1.8e^2}{2\pi\varepsilon\varepsilon_0 d} \quad . \tag{2.51}$$

For large particles, the energy gap approaches the bulk case, while for small particles the gap can be tailored by the size of the particle.

2.3.3 Quantum Dot Fluorescence

The change of the energy gap size has a striking effect on the optical properties of quantum dots. The discussion of quantum dots in the previous section started with absorption spectra (Fig. 2.7), where it was found that the lowest photon

energy needed for absorption depends on the particle size. This effect is described by eq. (2.51): a photon can only generate an electron/hole pair and be absorbed when its energy is larger than E_{Dot}.

In case of fluorescence it is assumed that a photon of energy larger than the gap energy has created an excited electron. This excited state has absorbed the photons angular momentum of ± 1. Immediately, this excited state relaxes to a state with angular momentum of 2. This relaxation is non radiative and rapid. In a first approximation, the resulting state can not further relax to the ground state (angular momentum 0) by emitting a photon, as a photon can only carry angular momentum of 1. This state is called "dark exciton". It can only decay over slight perturbations of the crystal lattice or weak coupling to phonons and thus, has a long lifetime [78,84]. The fluorescence is red-shifted with respect to the absorption band edge energy.

A quantum dot can be excited by light with photon energy greater than the energy gap. The following relaxation to the exciton ground state is faster than the subsequent dipolar process of photon emission such that the fluorescence spectrum has a maximum at the energy of the gap. The decay of the exited quantum dot state is of dipolar character: The quantum dot can be modeled as an oscillating electric dipole as long as only classical optical effects are taken into account [10].

Local Density of States

An important concept to quantify the interaction of emitters with their environment is the local density of states (LDOS). Its use bases on Edward Mills Purcell's work in the 1940s, who found that the decay rate of a magnetic dipole is not an intrinsic property of the atom or molecule, but rather depends on its environment [85]. The numerical calculations performed in case of the plasmonic rod antennas, use this terminology. As the density of states calculated for electron gases, the LDOS is a measurement of available states. Here, it gives the number of modes per unit volume and frequency into which a photon can be released during a spontaneous decay process. With Fermi's Golden Rule, which connects the decay rate of an initial state to the properties of available final states, the decay rate can be calculated as [10]:

$$\gamma = \frac{\pi\omega}{3\hbar\varepsilon_0}|\boldsymbol{\mu}|^2\rho_\mu(\mathbf{r},\omega) \quad , \tag{2.52}$$

with the transition dipole moment μ and the partial local density of state for that transition $\rho_\mu(\mathbf{r},\omega)$. In this thesis, the calculated LDOS in the near field of nanoantennas is used to get insight to quantum dot fluorescence enhancement, which is an experimental manifestation of enhanced decay rates.

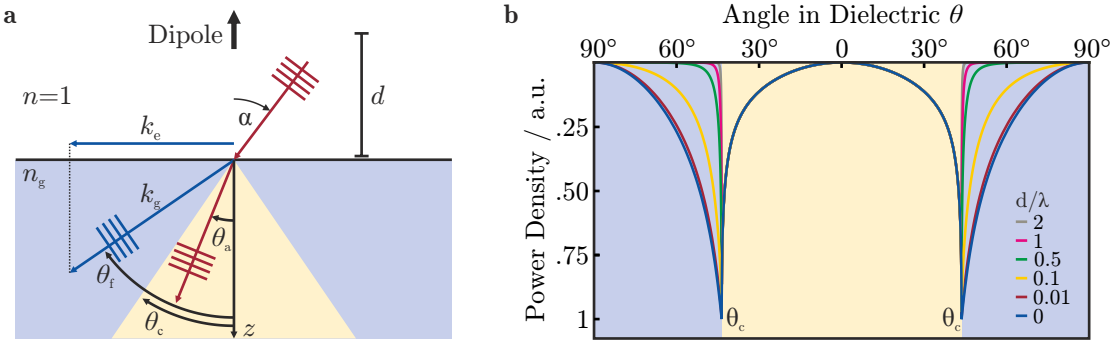

Figure 2.10: **a** Electric dipole with distance d above a dielectric with refractive index $n_g > 1$. Impinging light with angle α_a is refracted into the glass with angle $\theta_a < \theta_c$. Angles $\theta_f > \theta_c$ are reached by evanescent wave with $k_e = k_g \sin(\theta_f)$. **b** Angular power density of an electric dipole oriented perpendicular to the interface. *Allowed* light (yellow background) does not depend on distance d. For distances larger than λ nearly no *forbidden* light (blue background) is left.

2.3.4 Dipole Emitters at an Interface

In Section 2.2.4 a dielectric waveguide in a homogeneous environment was discussed. Just by introducing a glass substrate, the functionality of the waveguide changes dramatically and it turns into an antenna. Interfaces close to optical structures have a huge influence, partially because they introduce new radiation conditions for otherwise evanescent waves. For example, it is known that the total radiated power of single dipole emitters changes in vicinity of a substrate interface [86]. In this section the far-field distribution of the radiated power $P(\theta)$ per unit solid angle of such an emitter is discussed. Unfortunately, even for this potentially highly symmetric problem there is no closed solution [10]. Thus, here just an argument for the specific form of the far-field pattern of a single dipole emitter perpendicular orientated to the interface is given. The calculations follows closely [87].

An electric dipole is placed in vacuum with distance d to a dielectric interface as sketched in Fig. 2.10.a. The dielectric is homogeneous, lossless and described by the refractive index n_g. A plane wave emitted by the dipole impinges on the surface with angle α. The z-axis is parallel to the surface normal and points into the substrate such that the polar angle θ can be expressed by Snell's law as $\sin(\theta) = \sin(\alpha)/n_g$. Relevant for this thesis is the power distribution in the dielectric half space. Angles measured from the surface normal are denoted by θ and a subscript. The power transmitted into the solid angle $d\Omega_g = \sin(\theta)d\theta d\varphi$ (in the substrate) is equal to the power that the dipole emits into the solid angle

$d\Omega_1 = \sin(\alpha) d\alpha d\varphi$ (in vacuum) and transmitted through the interface. With the Fresnel transmittance $T_{1,\mathrm{g}}(\alpha)$ the power gets:

$$P(\theta) = T_{1,\mathrm{g}}(\alpha) P_0(\alpha) \frac{d\Omega_1}{d\Omega_\mathrm{g}} \quad . \tag{2.53}$$

The power pattern of the undisturbed (Hertzian) dipole is $P_0(\alpha) \propto E_0(\alpha)^2 \propto \sin^2(\alpha)$ as discussed in Section 2.2.1. Clearly, with Snell's law the solid angles are related as:

$$\frac{d\Omega_1}{d\Omega_\mathrm{g}} = \frac{n_\mathrm{g}^2 \cos(\theta)}{\cos(\alpha)} \quad . \tag{2.54}$$

Since the calculation is restricted here to a dipole perpendicular to the interface, only the Fresnel transmittance $T_{1,\mathrm{g}}(\alpha)$ for p-polarized waves need to be considered:

$$T_{1,\mathrm{g}}(\alpha) = T^p_{1,\mathrm{g}}(\alpha) = \frac{4 n_\mathrm{g} \cos(\alpha) \cos(\theta)}{(n_\mathrm{g} \cos(\alpha) + \cos(\theta))^2} \quad . \tag{2.55}$$

Equation (2.55) and eq. (2.54) can be inserted into eq. (2.53) and an intermediate result is:

$$P_\mathrm{a}(\theta) \propto \frac{n_\mathrm{g}^5 \sin^2(2\theta)}{(n_\mathrm{g} \cos(\alpha) + \cos(\theta))^2} \quad . \tag{2.56}$$

It is important to note here that so far the power pattern is independent of the distance of the dipole to the interface d.

Up to here the more intuitive case of the so called *allowed* light [10] was discussed. As mentioned above the angles on both sides of the interface are related by Snell's law:

$$\theta = \arcsin(\sin(\alpha)/n_\mathrm{g}) \quad . \tag{2.57}$$

Thus, eq. (2.56) is only valid for $0 \leq \theta_\mathrm{a} \leq \theta_\mathrm{c} = \arcsin(1/n_\mathrm{g})$ – or in other words: plane waves impinging with $0 \leq \alpha \leq \pi/2$ from the vacuum side can only reach the angular range $0 \leq \theta \leq \theta_\mathrm{c}$ on the dielectric side.

This result is well known even from basic discussion of Snell's law: traveling waves are only refracted into a cone around the surface normal with θ_c. This *allowed* region is marked yellow in Fig. 2.10.a. To get an expression for the power in the *forbidden* region (blue), the role of evanescence waves in the dipole's near field needs to be acknowledged. The wave vector components of the evanescence waves fulfills:

$$k_0 < \sqrt{k_x^2 + k_y^2} = k_\mathrm{g} \sin(\theta_\mathrm{f}) \leq k_\mathrm{g} \quad , \tag{2.58}$$

the magnitude of the wave vector $\sqrt{k_x^2 + k_y^2}$ is per definition larger than the wavenumber in vacuum k_0, but smaller than the wavenumber in the dielectric k_g. Thus, the evanescence wave can radiate into the dielectric with angle $\pi/2 \geq \theta_\mathrm{f} \geq \theta_\mathrm{c}$. This

effect is quite similar to the one used in the dielectric leaky-wave antennas. Since the evanescence wave decays exponentially, the emitted power will clearly depend on the distance d. Indeed, after further calculation the transmitted power for $\pi/2 \geq \theta_\mathrm{f} \geq \theta_\mathrm{c}$ can be written as [87]:

$$P_\mathrm{f}(\theta, d) \propto \frac{n_\mathrm{g}^5}{n_\mathrm{g}^2 - 1} \frac{\sin^2(2\theta)}{(n_\mathrm{g}^2 + 1)\sin^2\theta - 1} \exp\left(-2\frac{d}{\Delta d}\right) \quad , \tag{2.59}$$

and it is obvious that the power of this *forbidden* light [10] does decrease exponentially with distance. The characteristic depth Δd is defined as:

$$\Delta d = \frac{\lambda}{2\pi} \frac{1}{\sqrt{n_\mathrm{g}^2 \sin^2\theta - 1}} \quad . \tag{2.60}$$

Both, $P_\mathrm{f}(\theta, d)$ and $P_\mathrm{a}(\theta, d)$ have a maximum at $\theta = \theta_\mathrm{c}$ and are continuous at this point. Figure 2.10.b shows the calculated power $P(\theta)$ for a dielectric with $n_\mathrm{g} = 1.45$. The distribution of the *allowed* light is independent of the distance d of the dipole. For distances $d > \lambda$ there is nearly no power in the *forbidden* angular range, while for bigger distances $d \ll \lambda$, the distributions quickly resemble the $d = 0$ case with most power in the *forbidden* part [87]. Further calculation shows that the *forbidden* light is symmetrical with respect to the z-axis regardless of the dipole orientation [10].

Chapter 3

Sample Processing Methods

An essential part of the work conducted during this thesis was the fabrication of the active nanoantennas. This chapter illustrates the developed workflow in chronological order and serves as a complete overview over the process with all parameters given. The fabrication process is a combination of established procedures, new processes and protocol alterations. The chapter is divided into the first step producing nanostructures of gold and hafnium and the second step combining them with a fluorescence source.

3.1 Fabrication of Nanoantennas by Electron-Beam Lithography

Lithographically defined structures are at the core of modern technology. Microelectronics all around us, e.g., in our mobile phone processors or in our smart TVs, are lithographically manufactured [88]. In lithography a substrate is coated with a resist and the features, e.g., electronic circuits on a chip, are defined by radiation exposure. Subsequently, the exposed areas are dissolved in a developer (in the case of a positive tone resist). The fabricated template can be used to operate selectively on the exposed areas, e.g., etching or coating. The absolute resolution limit for standard processes is proportional to the used wavelength of radiation [89, 90].

The structures used in this thesis exhibit feature sizes in the order of tens of nanometers, e.g., the rod antennas discussed in Section 2.2.3 are 30 nm wide. The standard technique to fabricate them is a lithographic technique based on electron microscopy. Due to the small electron wavelength, e.g., for an acceleration voltage of $U_{\mathrm{acc}} = 20\,\mathrm{kV}$ it is $\lambda_{\mathrm{e}} = 9\,\mathrm{pm}$ [91], nanoscale structures can be fabricated. In contrast to photo lithography, there is no need for a physical mask [89], which allows a rapid prototype workflow.

The steps of the electron-beam lithography (EBL) process is sketched in Fig. 3.1 using the example of hafnium dioxide antennas. In the work for this thesis gold

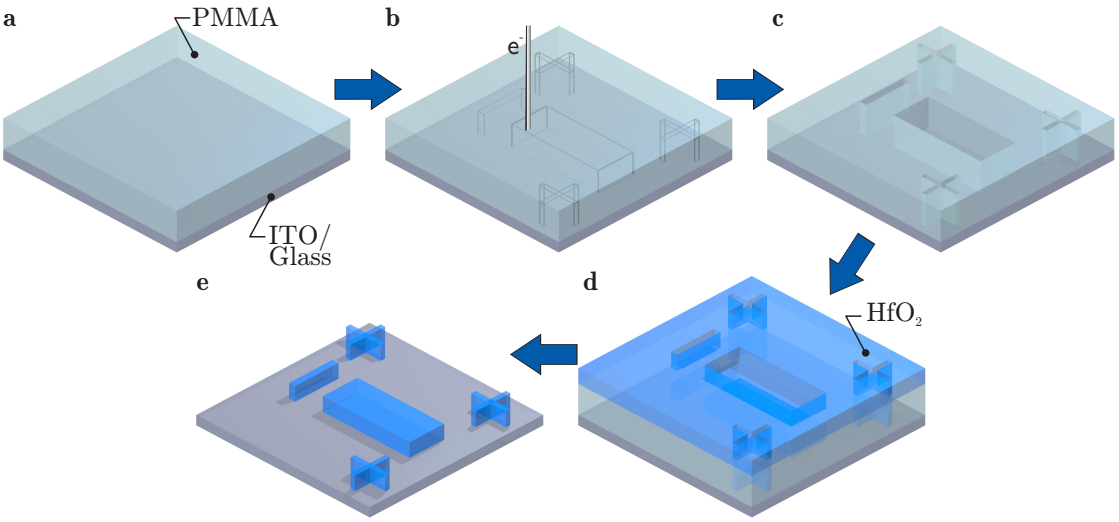

Figure 3.1: Electron-beam lithography for structuring nanoantennas: **a** PMMA is spincoated on a conductive sample. **b** The structure and potential alignment markers are defined by electron-beam exposure. **c** The exposed areas are removed by development in a solvent. **d** A thin film of the nanoantennas material is evaporated on the template. Here hafnium dioxide is chosen. **e** In a lift-off process the PMMA template and residual antenna material is removed.

was used to fabricate plasmonic and hafnium dioxide to fabricate dielectric nanoantennas. Since the process is structurally independent of the material, it is discussed together here for both material types. If parameters differ for gold (i) and hafnium dioxide (ii), they are discussed in the text separately.

Sample Preparation

The sample substrate is a 22 mm × 22 mm microscope cover glass with precises thickness of (170 ± 5) µm and a refractive index of $n_g = 1.52$ at 780 nm [92]. The glass slides have to be rigorously cleaned: first they are rubbed with an aceton wetted rag. Thereafter, they are submerged in sodium hydroxide (0.2 %), methanol and water, successively for 30 min each, while in an ultra sonic bath.

After cleaning, the substrates are coated with an 8 nm layer of indium tin oxide (ITO). The (for low frequencies) metallic ITO layer is necessary for the lithographic process, because a conductive sample is needed to prevent electrostatic charging from the deposited electrons in the microscope. Since thin layers of ITO are transparent, ITO is suitable for optical experiments [93]. The coating was carried out in the clean room facility at the research center *caesar* in Bonn with an electron-beam evaporator. The last step of the ITO-coating process is annealing of the sample in an oven at 430 °C for 4 h.

As an electron resist, we use poly(methyl methacrylate) (PMMA), which is spincoated on the sample. In a spincoater the sample is hold by a vacuum chuck. A solution of the coating material is dropped onto the surface and the sample is rotated. Usually there are two rotation phases: First a short one of moderate speed, which spreads the solution over the whole surface, followed by a longer and faster rotation, where the thin layer is formed. The adhesive forces at the interface of the liquid and the substrate together with the centrifugal forces result in an uniform thin film coating. The volatile solvent evaporates during the rotation. In case of a polymer coating the film thickness can be regulated by the molecular weight, the mass fraction of the solution and the rotational speed [94]. The PMMA-layer types and their resulting thicknesses used in this thesis are listed in Tab. 3.1.

As an electron resist the film needs to be substantially thicker then the structure to be fabricated. The gold nanoantennas have a designed height of 40 nm, while the hafnium dioxide nanoantennas are 180 nm thick.

(i) For the gold nanoantennas a moderate height of the resist layer is sufficient: A PMMA layer of 180 nm is fabricated (type A).

(ii) The hafnium dioxide antenna design is substantially thicker. Thus, the electron resist needs to be thicker as well. To reach a sufficient layer thickness two layers are stacked. First, a 260 nm layer (type B1) is spincoated. The layer is annealed on a heating plate at 150 °C for 3 min. After cooling down,

Layer type	A	B1	B2
Solvent	anisole	ethyl lactate	ethyl lactate
Mass fraction	4 %	4 %	4 %
Molecular weight	950 kg/mol	600 kg/mol	950 kg/mol
Rotation phase 1			
Rotational speed	500 rpm	500 rpm	500 rpm
Time	5 s	5 s	5 s
Rotation phase 2			
Rotational speed	4000 rpm	3000 rpm	7000 rpm
Time	90 s	90 s	90 s
Thickness	180 nm	260 nm	200 nm

Table 3.1: Spincoating parameters of the used PMMA layers and their resulting thicknesses [95, 96].

the second layer of 200 nm thickness (type B2) is coated on top of the first one. A different solvent is chosen here, since ethyl lactate does not, in contrast to other solvents, attack the first existing layer. In addition, the layers with the different molecular weights react differently to the electron beam, resulting in an undercut structure, which benefits the later lift off [96].

Finally, the samples are annealed in an oven at 175 °C for 20 min to remove residue solvent and smoothen the surface of the layer.

Lithography

The geometries of the antennas are written with a standard EBL system, consisting of a Zeiss SIGMA scanning electron microscope equipped with a Raith Beam Controller. The sample is mounted to a mechanical stage, to move it relative to the electron beam. The beam is deflected during the writing process electronically such that geometric shapes can be traced. A mechanical stage movement would neither be fast nor accurate enough. The maximal beam deflection is limited. Thus, depending on the choice of magnification, only specific write-fields sizes can be used. A lower magnification results in a larger write field. But at the same time the minimal step size of geometries traced by the beam increases, since it is limited by a digital-to-analog converter. The used magnification for the writing process is 600×, resulting in a write-field size of 100 µm × 100 µm and a minimum beam step size of 1.6 nm. Numerous write fields can be written on a sample sequentially in order to have multiple experiments or to achieve redundancy. Each field is limited by four 10 µm × 10 µm cross shaped markers, leaving an effective available area to write structures of 80 µm × 80 µm. In the EBL system structures are

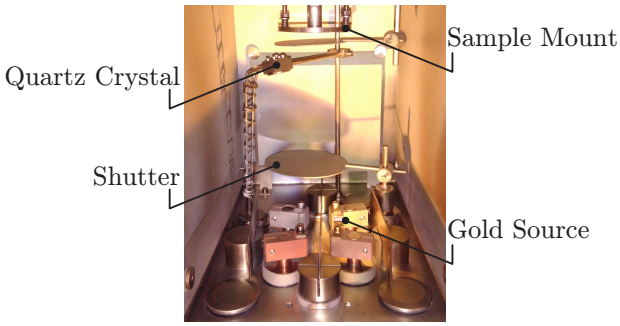

Figure 3.2: Photography of the vacuum chamber of the evaporation machines used for gold-film deposition. The material source is a tungsten vessel with gold pellets in it. The vessel heats up, when an electrical current flows through it. In the vacuum the evaporated gold particles have a long free path and cast a thin film over the whole chamber. The quartz crystal is use to monitor the deposition rate and needs to be close to the substrate.

represented by polygons and lines that are patterned automatically to be written by the electron beam. The fundamental elements used are lines and rectangular area elements.

(i) The gold nanoantennas are defined as straight lines with an electron line dose of 6.3 nC/cm. The electron beam follows the lines without patterning. In that sense, they do not exhibit a width.

(ii) The hafnium dioxide nanoantennas are defined by two rectangles with an electron area dose of 1.28 mC/cm^2. The rectangles are patterned by the system such that the electron beam writes parallel lines filling the area.

An acceleration voltage of 20 kV and an electron aperture with a diameter of 10 µm is used for exposure.

The deposited electrons destroy links in the PMMA chains. They recombine to chains of molecular weight of about 5 kg/mol [95]. Those smaller chains are soluble in a developer consisting of isopropyl alcohol (IPA) and methyl isobutyl ketone (MIBK) in a ratio of 3:1, with added butanone making up 1.5 % of the total volume. The solvent is kept in a refrigerator to ensure a stable temperature. The sample is developed by immersing it for 45 s in the developer, which removes the exposed PMMA. The sample is then dried.

Evaporation

At this stage, the substrate is covered with a PMMA template with a negative image of the written structures on it. This template needs to be covered with a thin film of the material of the nanostructers. To deposit a thin film of the nanostructure material, i.e., gold or hafnium dioxide, physical vapor deposition is used. The deposition material is brought into a vacuum chamber, where it is heated up and then evaporates. A photography of the vacuum chamber used for gold evaporation, where the source and the sample is labeled, is shown in Fig. 3.2. In the vacuum the vapor particle have a large free path length and can travel through the chamber without colliding with a background gas particle [97]. The sample is placed in the chamber, and vapor particles reaching it condensate into a solid on it. The deposition rate is measured by monitoring the change of the oscillation frequency of a quartz crystal inside the chamber. By integrating the rate over time, the height of the deposited film is measured [98]. The quartz crystal needs to be close to the sample, to have an accurate rate measurement.

(i) The gold evaporation is carried out with an electrical resistance evaporation machine (Univex 250, oerlikon leybold vacuum). Gold pellets are placed in a tungsten vessel. A high current heats up the gold to around 1400 °C. A layer of 40 nm with a rate of 0.4 nm/s is evaporated.

(ii) Evaporation of hafnium dioxide needs temperatures too high to be reasonably achieved with resistive heating ($\approx$ 2500 °C), but it can be evaporated by an electron beam impinging the source [99]. This process was carried out with an electron-beam evaporator (HVB 100L, Winter Vakuumtechnik) by collaborators at the University of Paderborn. Because the sample heats up through radiation during this process as well, the deposition of the 180 nm thick layer is done in two steps: during the process, the sample temperature is monitored and the evaporation is paused to let the substrate cool down under 100 °C. High sample temperatures result in a modification of the PMMA template leading to failures in the following lift-off process.

The deposited material on the ITO inside the template is disjoint from the layer on the PMMA template, since the PMMA film is thicker than the deposited material film. This way the layer on the template can be separated from the structures on the substrate: in the so called lift-off process a solvent dissolves the PMMA and washes away the material on it. Since both, gold and hafnium dioxide, exhibit a sufficient adhesion to ITO, the material on the substrate stays attached. As a lift-off solvent N-Methyl-2-pyrrolidone (NMP) is chosen. The dissolvement takes place on a long time scale (hours) relative to other solvents, e.g., aceton (seconds). Thus, the time parameter of the process can be adjusted with higher relative accuracy.

Additionally, because of its high boiling point (203 °C) [100], NMP can be safely heated during the process.

The PMMA template and the residue material is removed in a lift-off processes:

(i) The gold sample is submerged in 60 °C (NMP) for 3 h.

(ii) Presumably because of the larger thickness and hardness of hafnium dioxide, the lift off takes more preparation: A blade is used to scratch a roughly 10 mm × 10 mm rectangular form around the structure to give the solvent a larger working surface, assisting the lift off. The sample is then submerged in 60 °C NMP for 3.5 h. Afterwards, the sample, still in NMP, is put in an ultra-sonic bath for 30 s.

Results

In contrast to photo lithography, electron-beam lithography is not limited by the wavelength, but the resolution of the resist and the subsequent fabrication. Lithographic setups as used in this thesis with conventional PMMA resist have a feature size limit of about 30 nm [101]. The gold processing follows a well established protocol [19, 102, 103] such that the fabricated structures can have feature sizes close to the resolution limit of the lithographic process. Since the gold antennas are written as lines (1 pixel width), the width of an antenna is the smallest spatial feature on the sample. An electron micrograph of a gold nanoantenna of 170 nm length is shown in Fig. 3.3.a. The resulting antenna width is 30 nm. The width of the antenna can to some extend be increased by a slower scanning speed of the electron beam, i.e., a higher deposited dose. Scatterd electrons that are absorbed in the vicinity of the line increase its width. However, a substantially thinner line is not feasible to fabricate, since it is already at the resolution limit of the process.

In contrast to this, the hafnium dioxide antennas are of comparatively large scale in the micrometer range. Still, the achieved structures show imperfections. This can be attributed to the non-standard evaporation and lift-off process. Even with the cooling down phase of the sample during evaporation, the PMMA template was still near its glass transition temperature of 105 °C, where the polymer transitions to its soft rubbery state and deformation can occur [104]. Additionally, in preliminary experiments it was observed that scattered electrons in the evaporation chamber can cause exposure of the PMMA film, resulting in an altered reaction to the lift-off solvent. In Fig. 3.3.b an exemplary electron micrograph of hafnium dioxide nanoantennas is shown. It can be seen that there is a two layer structure on the antennas, with the upper layer not filling the same footprint as the bottom one. Additionally, they are not centered to each other but are shifted. This shift is unidirectional for all shown antennas. A possible explanation is that

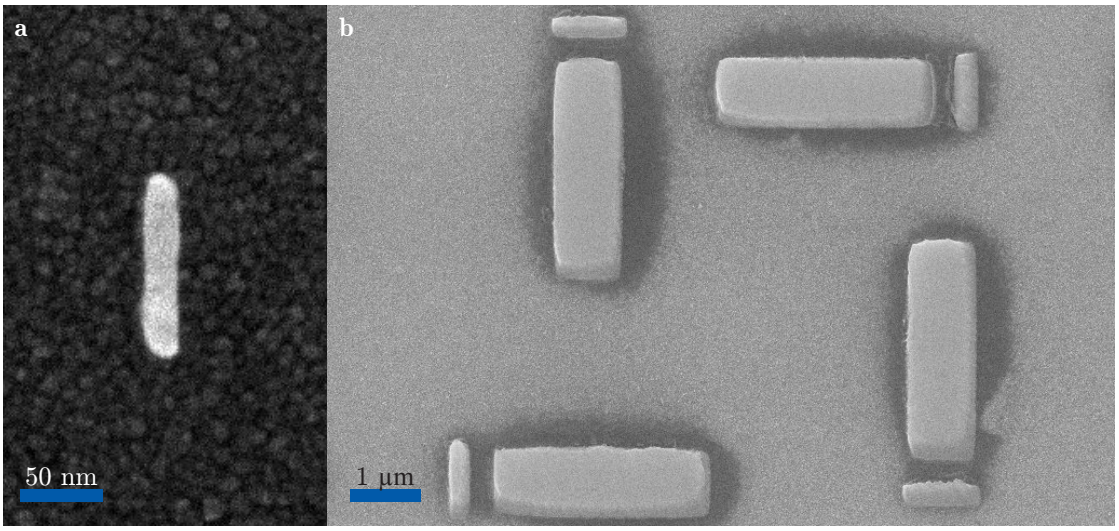

Figure 3.3: Electron micrograph of lithographically fabricated nanostructures: **a** A gold rod nanoantenna of 170 nm length and 30 nm width. **b** Four hafnium dioxide antennas with directors (larger rectangle) of size 1 µm × 3.2 µm. In the hafnium dioxide there is an underlying structure visible.

the sample was perpendicularly mounted to the line of sight to the hafnium dioxide source. For successive experiments, improvements of the evaporation process promise to result in smaller feature sizes of the nanostructured hafnium dioxide, which were not necessary for this thesis.

3.2 Quantum Dot Deposition

Nanoantennas can be employed in arrays to manipulate light beams, e.g., as polarization or spectral filter. Those effects rely on the far field properties of the structures. Another fruitful but also more challenging way is to tailor devices that directly exploit the near-fields of the structures. In particular, hot-spots are promising features, since the light-matter interaction in the enhanced near field can be significantly increased. Additionally, the antenna can gap the mismatch between the wavelength of light and the size of local emitters such as single molecules or quantum dots. Nanoantennas can be designed to mediate the coupling of small emitters to the far field and vice versa [9, 11, 26]. Because of those properties a naturally emerging application is the sensing of single fluorescent molecules, where the antennas ability to enhance the quantum efficiency is used [36, 37].

In this thesis, quantum dots are used as local emitters to feed nanoantennas.

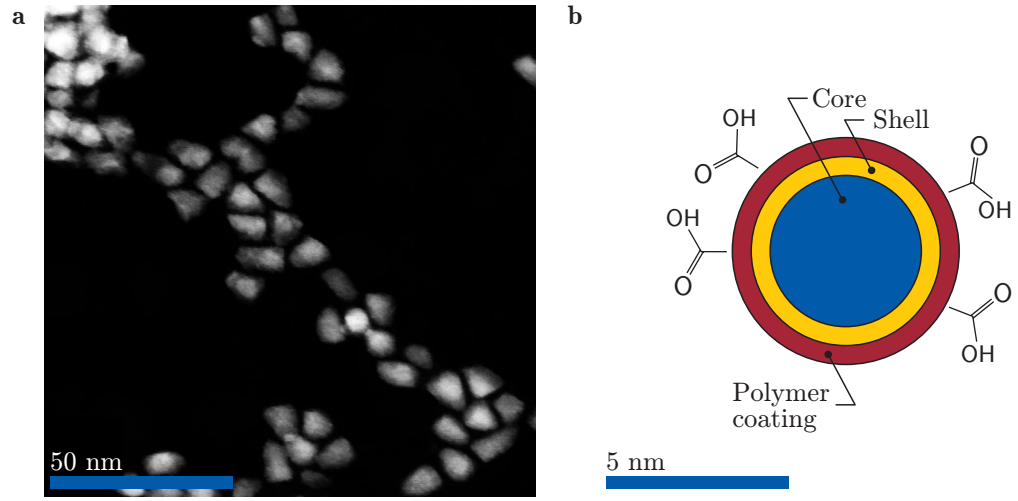

Figure 3.4: **a** Transmission electron micrograph of colloidal CdTeSe quantum dots. **b** Schematic representation of CdTeSe quantum dots. The CdTeSe core is shelled with ZnS. The thicknesses of the layers are roughly to scale.

Nanoantennas are challenging to feed electrically, since macroscopic wiring interferes with the antenna's small geometry. Thus, quantum dots, i.e., semiconductor nanocrystals, are placed close to the nanoantenna, pumped by light and then feed the antenna with their fluorescence.

In order to investigate the discussed near-field effects, a precise method of deposting emitters into the vicinity of the nanoantenna is necessary.

In the following section the used semiconductor quantum dots are introduced and the deposition method developed during this thesis is discussed.

3.2.1 Colloidal Semiconductor Quantum Dots

In this thesis commercial available colloidal semiconductor quantum dots are used (Qdot 800 Carboxyl Quantum Dots, Thermo Fisher Scientific). A transmission electron micrograph of an ensemble of the quantum dots is shown in Fig. 3.4.a. They consist of a cadmium telluride selenide (CdTeSe) core and a zinc sulfide (ZnS) shell with a polymer coating in aqueous solution (see Fig. 3.4.b). Their emission is centered around a wavelength of 780 nm. This wavelength range was chosen to be far from the interband transition of gold, so that the quantum dots are suited as active elements for gold nanoantennas.

Colloidal quantum dots are semiconductor nanocrystals grown in large numbers in a liquid solution. In contrast to dots epitaxially grown on a substrate, they are free-standing [78]. They are fabricated by a wet chemical process in a liquid that contains the atomic species that will later build the nanocrystal and compounds

that control nucleation and growth. Their typical size ranges from 1 nm to about 20 nm [105].

The fabrication of colloidal quantum dots with high fluorescence yields for the near infrared regime is quite challenging. In the visible regime CdSe based quantum dots are widely used, but they are restricted by their bulk band gap (see Section 2.3) to wavelengths smaller than $\sim$ 700 nm. To overcome this, alloys of semiconductor like CdTeSe can be used [106]. The optically active core of the quantum dot is usually protected by a shell that serves as a physical barrier to the surrounding medium. Typically, a shell material with a large band gap is chosen, e.g., ZnS, such that the conduction band energy of the shell material is higher than that of the core material, while the valence band energy of the shell material is lower. This caps the generated electrons/holes from spreading over the whole particle [78]. Additionally, the core is protected by the shell from oxidation and leeching of the core material into the surrounding solution is prevented [107]. With a polymer coating, the dot can be further protected from influences of the chemical environment. Moreover, this coating can be chosen such that it provides surface groups suitable for further processing. The quantum dots used here exhibit a polymer layer that allows facile dispersion in aqueous solutions. At the surface there is a carboxyl group, which will be utilized for chemical linking.

3.2.2 Lithographic Technique

Multiple techniques to achieve control over the position of quantum emitters next to nanostructures are established in literature [24,25,36,50–55]. During this thesis, a deposition technique for colloidal quantum dots was developed and employed that focuses on the ability to be applicable in versatile experimental situations. Additionally, the individual procedures (electron-beam lithography and chemical linking) that are combined to deposit the quantum dots are all well established, which promises an easy adaptation for applications.

The techniques described here are to some extend identically to the first lithograpic step. For the sake of a comprehensive description, some parameters are repeated here. In a first lithography step nanoantennas and markers are written as described above. Subsequently, the markers are used in a second lithography step to produce a PMMA template defining the sites to deposit quantum dots. They are chemically linked to those sites. The quantum dot deposition technique that was developed during the work of this thesis can be universally employed on all samples with an ITO surface. Usually, on the sample there is already an underlying nanostructure. For illustration purposes in the sketch of the procedure (Fig. (3.5).a-f) a dielectric nanostructure is shown.

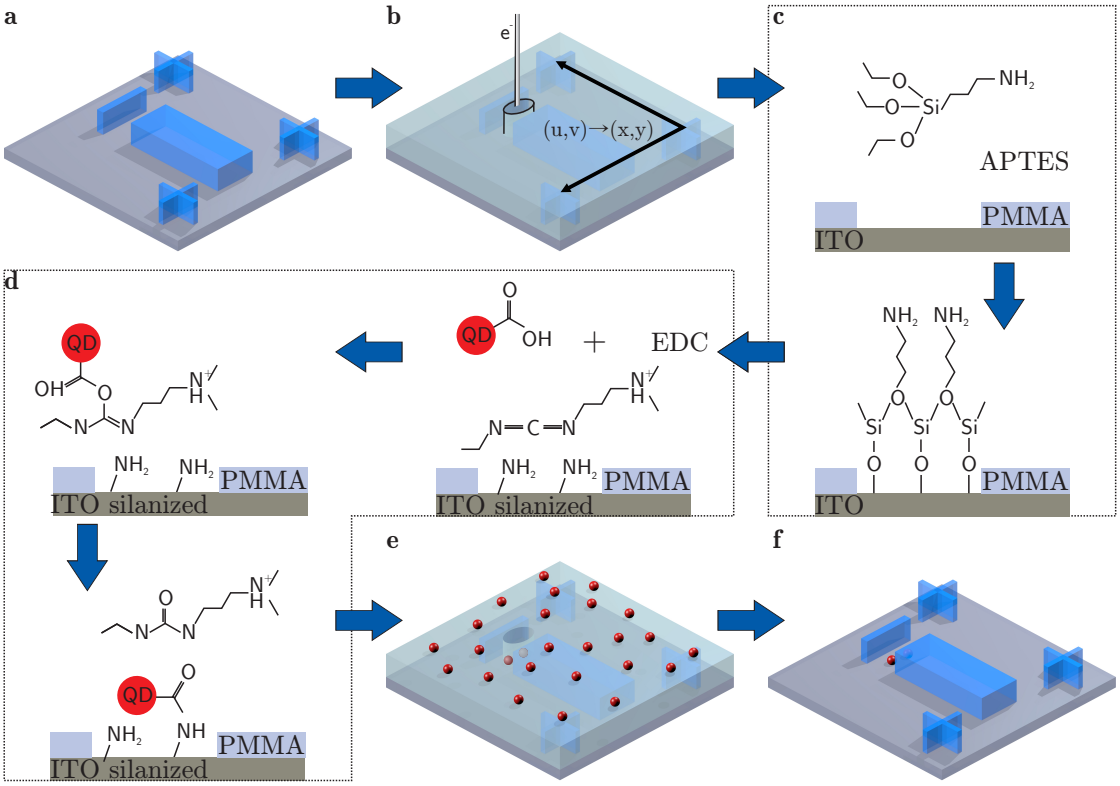

Figure 3.5: Quantum dot deposition technique using the example of a dielectric nanoantenna: **a** Nanostructured sample on an ITO substrate with alignment markers. **b** The alignment markers are used to precisely read in the coordinate system of the existing structures and the deposition sites are exposed to the electron beam. **c** The surface of the ITO is silanized by APTES. **d** The aqueous quantum dot solution and EDC is applied to the substrate and the dots are chemically bound to the exposed silanized ITO. **e** Quantum dots on the PMMA are removed together with the template in a lift-off process such that **f** the nanostructure with quantum dots at the lithographically defined patches is the result.

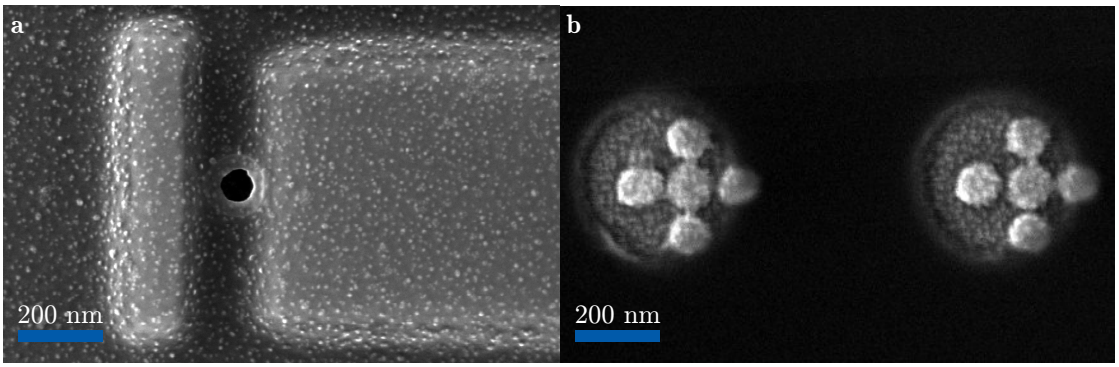

Figure 3.6: Electron micrographs of nanostructures after the second lithography step and quantum dot deposition, but before the second lift off: **a** Cut-out of a dielectric nanoantenna. The contrast is chosen such that the quantum dots on the template are visible. The deposition hole is black. **b** Gold nanostructures with large deposition holes. Contrast highlights the dots in the deposition holes and the template is black.

Sample Preparation

The starting point of the procedure can be any sample with an ITO surface. For the sake of this discussion a sample with a dielectric nanoantenna is chosen. Together with the nanoantennas, alignment markers are part of the sample design. As in the first lithography step, PMMA is used as an electron resist. A 180 nm thick PMMA layer is spincoated as described in the previous section (type A in Tab. 3.1). The sample is then annealed in an oven at 175 °C for 20 min, to remove residue solvent and smoothen the surface of the layer. Subsequently, it is mounted in the electron microscope again.

Second Lithography Step

The second lithography step bases on the same principle as the first one. While for the first step a rough position calibration on a millimeter scale is sufficient, the patterns of the second step need to be positioned precisely relative to the existing structure. The structure is covered in a PMMA layer, which makes imaging challenging. For better visibility a detector in the electron mircsocope is chosen, which is most sensitive to electrons generated after multiple scattering events (SE2 detector) [108]. The nanostructures relevant for the experiment must not be imaged with the electron microscope at this point. The electron deposition during image scanning would already expose the resist. In order to locate the write fields on the sample without exposing them to the electron beam, the experimentally relevant fields are surrounded by 100 µm × 100 µm cross shaped markers. They are found

by manually driving the sample carefully into the field of view. Based on their position, the original coordinate system of the sample is mapped to the current stage position. The stage can now be automatically driven to the coordinates of the write fields.

To accomplish high accuracy the coordinate system needs to be aligned again for each write field individually. Since the electron microscope is not equipped with a laser controlled stage, the stage movement to the write field is only precise to approximately 5 µm. This value depends on the driven distance and is typical for the used distances between the write fields. When the stage is driven to the write field position, all points on the field (plus an additional safety margin) can be reached by beam deflection without mechanical movement. The error of the mechanical movement can be corrected by beam shift alone. For this purpose each write field has four 10 µm × 10 µm cross shaped markers at the corners. The system scans images of their estimated positions, while blanking the beam at the center of the field with the functional structures. The markers' center positions have to be manually identified by the lithography system user. The appropriate rotational and zooming parameters are then calculated automatically. This method ensures that only PMMA on the alignment markers and not on the functional nanostructures is exposed. The deposition sites are defined by circles and rectangles. As far as the electron dose is concerned, the same values as for standard lithography of nanostructres are applicable. However, they have to be adapted to the structure in the vicinity of the hole, e.g., due to more scattered electrons, the dose of a hole next to a gold structure needs to be smaller than on pure substrate.

After the exposure, the sample is developed by immersing it for 45 s in a solvent consisting of isopropyl alcohol (IPA) and methyl isobutyl ketone (MIBK) in a ratio of 3:1, with added butanone making up (1.5 %) of the total volume. This removes the exposed PMMA.

Silanization

At this step, the sample is covered in PMMA and at the designated quantum dot sites the ITO is cleared. Additionally, the imaging of the markers inevitable exposes the PMMA covering them. First, the ITO must be functionalized with the correct surface group to enable the chemical linking [109]: the sample is put in a solution of 10 % (3-Aminopropyl)triethoxysilane (APTES) in isopropyl alcohol for an hour (typical: 10 ml). APTES silanizes the surface by building bonds across the interface with free amino groups (NH_2) at the outside [110]. After the silanization the sample is thoroughly rinsed with isopropyl alcohol to prevent contamination of the sample with unbound APTES. Isopropyl alcohol was chosen as a solvent for APTES, since it proved in preliminary experiments to be the least aggressive towards the PMMA template among methanol, ethanol and hexane.

Aqueous Quantum Dot Solution

The quantum dots come in a solution with molar concentration given by the manufacturer as $c_{\mathrm{st}} = 8\,\mu\mathrm{mol/l}$. The solution is buffered to pH 9 [111]. The optimal reaction medium for the later used agent is at acidic ph values [112], but the used reaction occurs at least up to pH 7.5 without significant loss of yield [113]. To have a medium suitable for the quantum dots and the EDC reaction, a new pH buffer is prepared. Tris(hydroxymethyl)aminomethane (TRIS) is used as a buffer component. In 100 ml water 120 mg TRIS is solved. The pH value of the solution is measured continuously, while hydrochloric acid (0.24 %) is added in 100 µl doses until the pH value reaches 7.5.

From the starting quantum dot solution $V_{\mathrm{QD}} = 2\,\mu\mathrm{l}$ is given into $V_{\mathrm{Buf}} = 1\,\mathrm{ml}$ of the prepared buffer solution. Thus, the molar concentration of quantum dots in the pH 7.5 buffer is $c_{\mathrm{QD}} = c_{\mathrm{st}} V_{\mathrm{QD}} / V_{\mathrm{Buf}} = 16\,\mathrm{nmol/l}$.

Chemical Linking

As discussed before the used quantum dots are coated with a polymer such that the surface exhibits carboxyl groups. The sites to couple to on the substrate were modified to exhibit amino groups (silanzied ITO). This is a common situation in protein chemistry and there are established processes to link those two groups. Carbodiimides are known to mediate the formation of amide linkage [113]. We use the carbodiimide 1-Ethyl-3-(3-dimethylaminopropyl)carbodiimide (EDC), because of available protocols (Fig. (3.5).d): First 30 mg EDC is dissolved in 1 ml water. Then 30 µl of this solution is added to the prepared quantum dot solution. EDC reacts with the carboxylic groups at the quantum dots surface to form an intermediate bound. The EDC solution as well as intermediate bound are unstable in aqueous solutions. Hence, the steps involving them are to be done without any time delay. On the sample surface an o-ring, as used for fluid sealing, is placed centering the nanostructures. The container formed in this fashion is filled with the quantum dot/EDC fluid. The amine group on the ITO forms an amide bond with the quantum dots carboxyl group and an EDC by-product is released and dissolved in the surrounding water, while the quantum dots stick to the modified surfaces. Since the EDC only moderates the link and does not add any components to it, it is consequently called a zero-length cross-linker [113]. The fluid stays on the substrate for two hours with periodic stirring. Then it is picked up with a pipette to avoid spillage of quantum dots to the back side of the substrate. An electron micrograph of a dielectric antenna in this processing stage is shown in Fig. 3.6.a. Here, the contrast is chosen such that the quantum dots on the PMMA template are visible. The hole, in which the dots are to be deposited, is visible in the center of the image. Figure 3.6.b shows the same processing stage of a sample

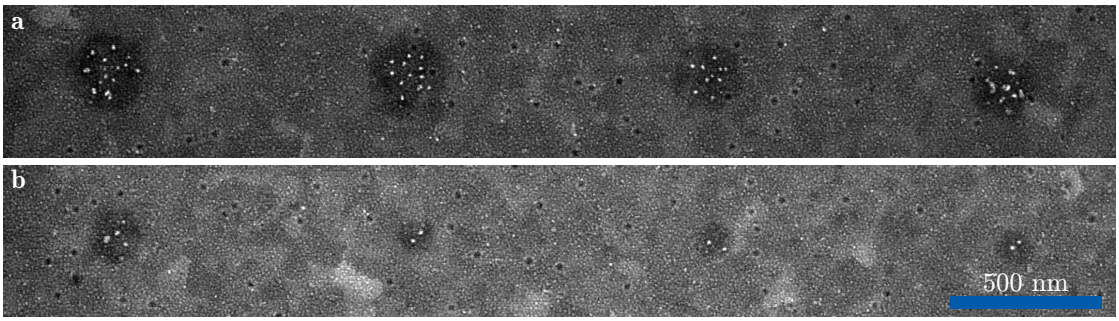

Figure 3.7: Electron micrographs of deposited quantum dots. The patches are on a grid with 1 µm separation. **a** The surface modification on the larger patches appears dark in the electron microscope. **b** For smaller patches, the number of deposited quantum dots decreases.

with a gold nanostructure. The contrast here makes the dots in the hole visible and blacks out the ones on the template. To wash away chemical process remains and residue quantum dots on the template, the substrate is rinsed carefully with buffer solution. Then the PMMA is removed in a lift-off process, where the sample is suspended in 60 °C NMP for 3 h.

Deposition examples

In general, the precision of the quantum dot placement is governed by the size of the holes in the template, i.e., it is restricted to the standard resolution of the EBL system. A standard lithographic setup as used in this thesis with conventional PMMA resist has a feature size limit of about 30 nm [101]. The accuracy of the placement, i.e., how well the area of the patch can be positioned, relatively to an underlying nanostructure, depends on the quality of the used coordinate system. In the first step, markers have to be set that define a coordinate system such that in the second lithography step the same coordinate system is used. The coordinate system mapping is typically accurate to ~ 5 nm. Thus, the accuracy of the deposition is better then the precision.

Figure 3.7 consists of two electron micrographs and shows typical quantum dot patches on ITO. On a blank ITO-covered glass substrate patches of quantum dots of various sizes were written on a micrometer grid. The surface alteration at the patch sites is visible: the areas around the deposited dots appear darker in the electron microscope. On those areas the dots are randomly distributed. For the smallest shown patches only two dots can be identified in the electron microscope. A first verification that the white spots seen in the electron micrographs are quantum dots can be achieved by taking a fluorescence image as seen in Fig. 3.8. On

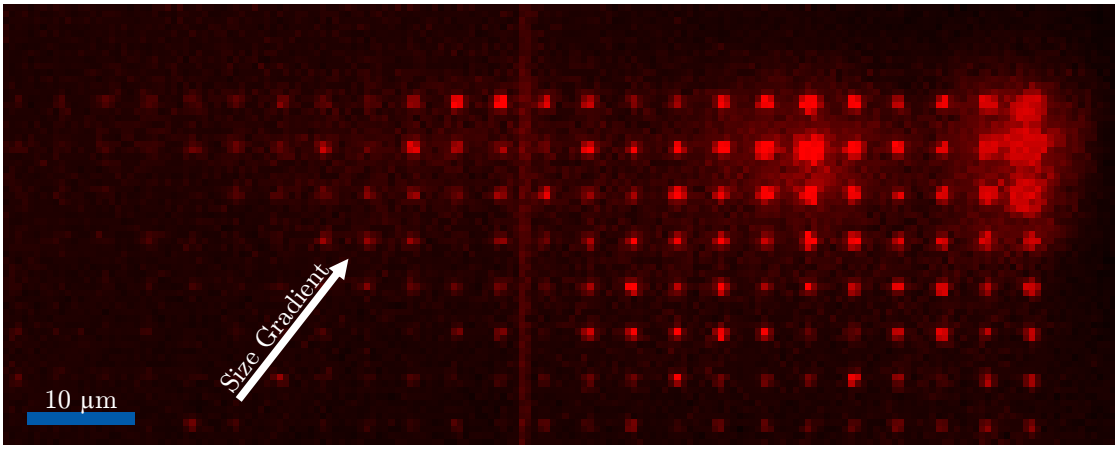

Figure 3.8: Image of quantum dot fluorescence in false color. The quantum dots were lithographically deposited in patches on a 2 µm grid. The direction of the size gradient of the patches is given by the white arrow. The line in the center of the image is a gold line for alignment purposes.

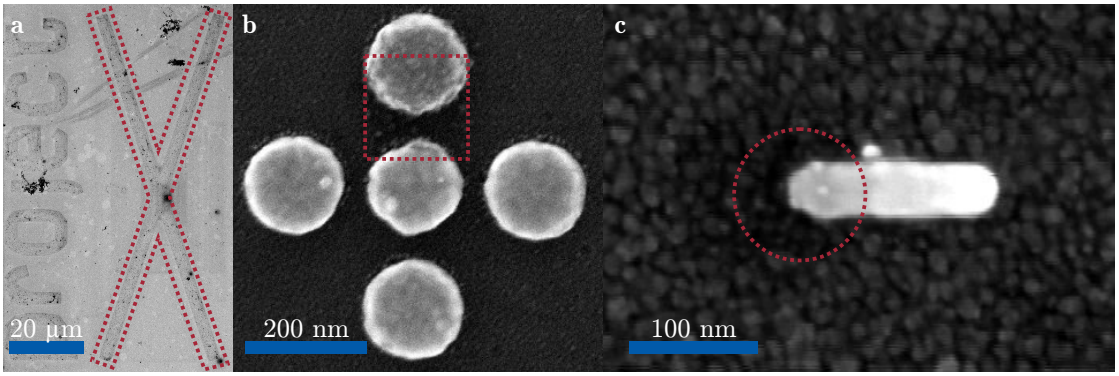

Figure 3.9: Electron micrographs of deposited quantum dots. To guide the eye, the quantum dot patches are marked in red. **a** The large cross and the writing on the left consist of lithographically deposited quantum dots. **b** Gold nanostructure with quadratic quantum dot patch. **c** Gold rod antenna with circular quantum dot patch.

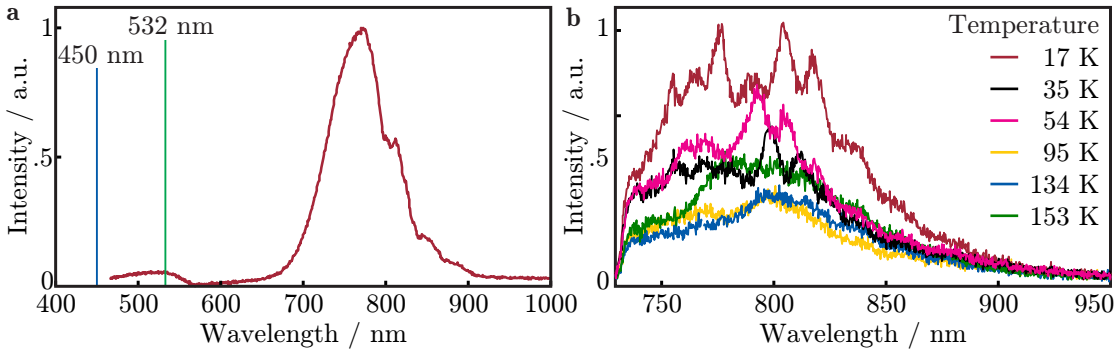

Figure 3.10: **a** Fluorescence spectrum of an ensemble of colloidal CdTeSe quantum dots on a glass substrate. The quantum dots were excited by a laser beam with $\lambda = 532\,\mathrm{nm}$. Residue pump light is detected in this spectrum. Later experiments use a blue laser with $\lambda = 450\,\mathrm{nm}$. **b** Temperature depended spectra of an ensemble of quantum dots. For low temperatures the fluorescence lines of individual emitters arise from the emission continuum. The sharp edge at $\lambda = 730\,\mathrm{nm}$ is due to a long-pass filter.

this sample, quantum dots are deposited on patches of increasing size. The larger the patches, the higher the fluorescence signal gets. The largest patches in this image contain about 100 dots.

The deposition method is as versatile as the lithography system: Figure 3.9.a shows an electron micrograph of a lithographically defined large-scale structure of quantum dots. In such large structures, a layer of dots forms in the written PMMA template. Relevant for this thesis is the ability to place smaller patches in vicinity of nanostructures. For reasons of contrast, small patches of dots next to structures are hardly visible in the electron microscope: in the exemplary images in Fig. 3.9.b and .c the medium sized deposition areas are additionally marked with a dashed line to guide the eye.

It is an interesting observation that the quantum dots remain on the gold structures, even when the process is designed to provide a link between ITO and the quantum dots. A possible explanation is that the inherent adhesion between gold and quantum dots is strong enough to resist the lift of process. Additionally, the gold surface can easily be contaminated by carbonaceous molecules [114] to which a link could be formed.

3.2.3 Fluorescence Spectra of Quantum Dots

A typical fluorescence spectrum of a large ensemble of colloidal quantum dots on a glass substrate is shown in Fig. 3.10.a. A lithographically defined patch of $5\,\mu m \times 5\,\mu m$ covered in a layer of quantum dots is excited by a green ($\lambda = 532\,nm$), continuous wave laser beam. About 250 quantum dots are excited in the focus. The fluorescence light is separated from the pump light by a dichroic mirror and optical filters. The fluorescence spectrum is recorded by a grating spectrometer with a cooled CCD camera. The fluorescence is centered around $\lambda = 780\,nm$. The fluorescence is spectrally broad with a full width at half maximum of $\Delta\lambda_{QD} = (95 \pm 5)\,nm$. Due to the nature of the growth process, any colloidal quantum dot ensemble contains a distribution of sizes and thus the emission band is broadened. In the infrared regime this effect is usually stronger, since the longer growth period of the crystals leads to a broader size distribution [78]. Besides this inhomogeneous effect, colloidal quantum dots experience homogeneous line broadening due to thermal effects (exciton-phonon coupling) [115].

In order to measure unbroadened quantum dot fluorescence, additional low-temperature measurements were performed at the Max-Planck-Institut für Festkörperforschung in Stuttgart. Here, the sample was mounted in a helium cryostat and cooled down to a minimal stable temperature of 17 K. As a pump source a green ($\lambda = 532\,nm$), continuous wave laser beam was used. The fluorescence spectra of a smaller ensemble of roughly 15 particles were measured at different temperatures and can be seen in Fig. 3.10.b. The spectra with the three highest sample temperatures (95 K, 134 K and 153 K) resemble a single broad fluorescence band similar to the large ensemble. For lower sample temperatures (17 K, 35 K and 54 K), the temperature broadening gets small enough for sharper lines of individual emitters to arise from the ensemble spectrum. The sharp edge at $\lambda = 730\,nm$ is due to the long-pass filter suppressing the pump light. This measurement was performed to investigate the transition between the deep and high temperature behavior, while the sample was warming up. The temperature was not stabilized at the measurement points. Therefore, it was not feasible to take a background measurement at each point and the intensities are not comparable. Additionally, the integration time was limited to 20 s. Nevertheless, the purpose of the measurement to see the emerging quantum dot lines was met.

A fluorescent measurement at a stabilized temperature of 19 K was performed with an integration time of 60 s. The width of the emerging lines is deduced by fitting Lorentz profiles to them. An exemplary background-corrected spectrum is plotted in Fig. 3.11. Here the apparently sharpest line was cut off by the long-pass filter. The line width of the quantum dots is nearly 10 times smaller than the room temperature ensemble width. The experiments of this thesis can be conducted at room temperature, since no resonant excitation of the quantum dots is used and

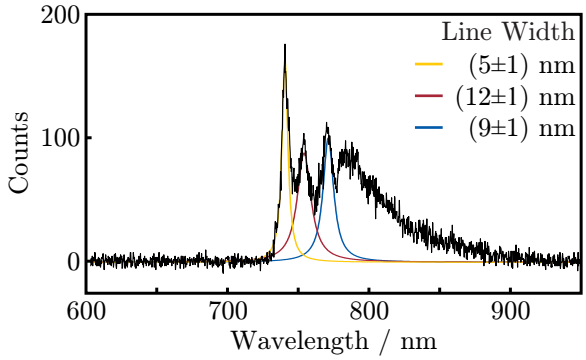

Figure 3.11: Background-corrected fluorescence spectra of quantum dots at 19 K. The width of the line is determined by fitting Lorentz profiles. The apparently sharpest line is cut off by the long-pass filter.

the investigated antenna modes are broad as well.

Chapter 4

Optical Measurement Setup

Both fabricated types of active nanoantennas were characterized and investigated in the same optical setup. The core of the setup is a high numerical aperture microscope objective, providing a high resolution and a big detection angle, crucial for measurements on both types of antennas. The concept of the microscope and shared instruments relevant to both experiments are described in this chapter. While the capabilities of the setup are described here, details on used experimental parameters are given in Chapter 5 and 6.

4.1 Confocal Microscope

The optical characterization of the active nanoantennas is done in a confocal microscope. In a classical microscope a specimen is illuminated by a light source. The specimen plane is mapped to an image plane. The spatial information of the whole specimen can be obtained simultaneously. In contrast to that, in a confocal microscope only information of one point is available at any given moment. Both the illumination and the detection relies on a pinhole. The illumination source is focused and the specimen is put in the focal plane (or the illumination pinhole is imaged onto the specimen plane). Thus, only one point limited by diffraction is illuminated on the specimen. This point is than mapped onto an aperture (the detection pinhole) such that only the intensity of light passing it can be measured. To retrieve spatial information of the specimen, raster scanning is necessary: either the focal point or the sample needs to be moved with respect to each other. Confocal microscopy has some advantages in specific measurement situations over standard microscopy, like spatially precise optical excitement and better spatial resolution [116].

The lateral resolution limit of a microscope with operating wavelength λ and numerical aperture NA is given as [3]:

$$\Delta x = K\frac{\lambda}{\mathrm{NA}} \quad , \tag{4.1}$$

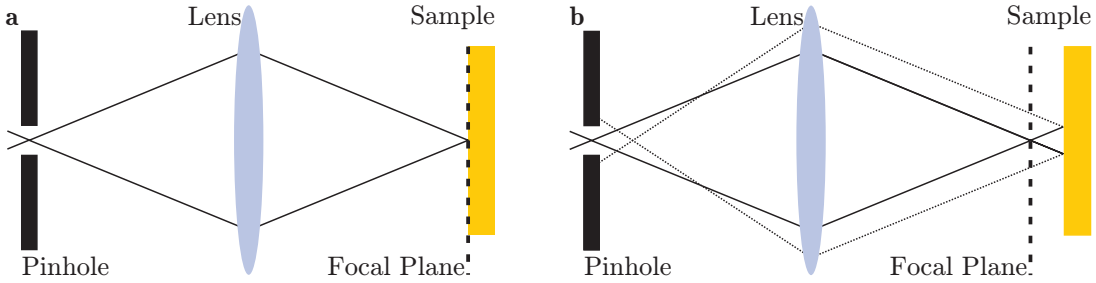

Figure 4.1: Simplified schematic of a confocal scanning microscope and the origin of its depth resolution. A pinhole is used to illuminate the sample point like. **a** If the sample is located at the focal plane, the sample point is imaged back onto the pinhole. **b** If the sample is out of focus, the signal from the sample is not imaged onto the pinhole. The reflected rays are drawn dashed.

where the constant K depends on the definition of resolvability and the used microscopy technique. The often used Rayleigh criterion defines two points to be just separately resolvable, when the maximum respond of one point is located in the zero of the respond of the second point. With that criterion, K for standard microscopy becomes $K = 0.61$, while being only $K = 0.37$ for a confocal setup. The reason for the better resolution is that with a standard microscope, each point of the uniformly illuminated sample gives rise to an Airy function describing the field at the image plane. In a confocal microscope however, the illumination itself has the form of an Airy function and is spatially coherent. Thus, the resulting field in the image plane is the square of an Airy function [117].

A second advantage of confocal microscopy is the ability to only image specific planes in the specimen, employing the small depth of field of the microscope objective. Figure (4.1).a is a simplified schematic of a confocal microscope. Only one point at a time is illuminated on the sample by an illumination pinhole. Light reflected on the sample is imaged back to the pinhole. In a real setup the illuminating aperture would usually be distinct from the detection aperture, i.e., the light originating from the sample is separated by a beam splitter. If the sample moves out of focus (Fig. (4.1).b), the light coming from the sample is not focused back into the pinhole. The image of the defocused plane disappears quickly, when a raster scan is performed. In contrast to that a defocussed sample in a classical microscope leads to a blurred image, since the defocussed light is still recorded. With the refractive index n, the resolution in z-direction is given as [117]:

$$\Delta z = 0.45 \frac{\lambda}{\left(n - \sqrt{n^2 - \mathrm{NA}^2}\right)} \quad . \tag{4.2}$$

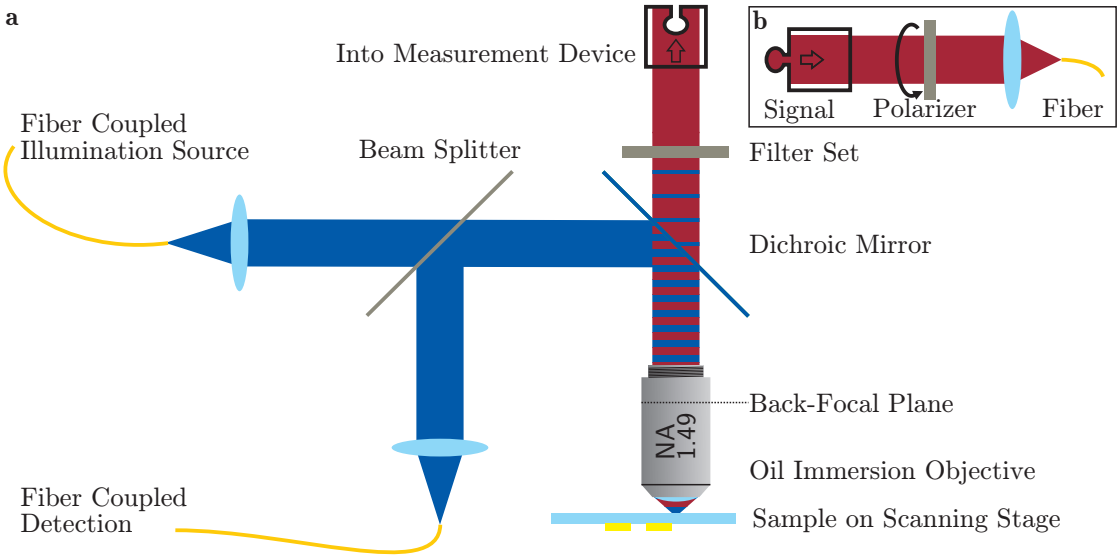

Figure 4.2: **a** The illumination and reflection detection of the setup used in this thesis is fiber based. It resembles a confocal microscope. The apertures of the fibers serve as the confocal pinholes. Light is focused the sample and collected by the same high-numerical-aperture objective. Since the objective is oil immersed, the structured interface of the sample faces away from the objective. A dichroic mirror and a set of filters separate the pump light from the fluorescence. The fluorescence is detected by a measurement device suitable for the experiment. **b** With a lens focusing the fluorescence into a fiber, the setup becomes a confocal fluorescence microscope.

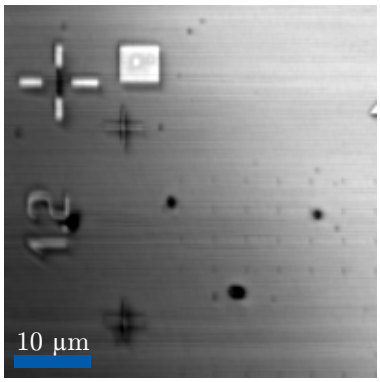

Figure 4.3: A reflection scan of gold structures. The image size is 50 µm × 50 µm with 0.125 µm step size. A write field alignment marker in the upper left corner is accompanied by a gold square. In the center of the image point like features on a grid stem from gold nanoantennas. During this scan the sample tilt was not corrected, apparent by the background gradient.

In a typical setup (NA = 1.45, $n = 1.52$) the depth resolution ($\Delta z = 0.42\lambda$) is about twice as large as the lateral resolution ($\Delta x = 0.26\lambda$).

Besides the inherent, slight resolution advantages, in this thesis a confocal setup is mainly chosen, since single nanostructers are to be addressed and their emission imaged on sensors. A sketch of the illuminating and reflection detection part of the optical setup can be seen in Fig. 4.2.a. This part closely resembles a standard confocal microscope. Only the beam path of the collected light of a single point is sketched. The illumination source is fiber coupled and the fiber aperture serves as the illumination pinhole of the microscope. The light is collimated and focused on the sample by a high-numerical-aperture objective (100× magnification, NA = 1.49) through the substrate. Light that is reflected at the sample is collected with the same objective. It is reflected by a dichroic mirror and a beam splitter to be coupled into a fiber. This fiber aperture serves as the detection pinhole. The light coupled to the fiber is detected by a photo diode. The sample is mounted on a piezo-driven three-axis translation stage to raster scan images. This way maps of the reflectivity of the sample can be recorded. Since a confocal microscope is very sensitive to the lateral position of the imaged object, a slightly tilted sample leads to a disturbed scan. When the plane of the substrate is not perpendicular to the scanning plane, some features of the sample will be in focus and some will be defocused. An example of a reflection map of a sample of gold nanostructures on a glass substrate is shown in Fig. 4.3. An alignment marker, labeling and a gold square can clearly be seen. In the center of the image gold nanoantennas appear point like. Over the size of the scan defocussing due to the sample tilt is obvious.

To compensate for that effect each 100 µm × 100 µm write field is equipped with gold squares, big enough to precisely measure the beam size at the sample plane. In a scan, the gold square is driven into the beam. The form function of the gold edge is convoluted with the Gaussian beam shape. Assuming a perfectly sharp edge, i.e., a Heaviside function, the resulting measurement can be modeled as a Gaussian error function and the beam width is extracted by a fit. This line scan is done at multiple z-positions such that the smallest beam width and the focal point position z_0 is found. The z-position is measured for three gold squares on the write field. Thus, the equation for the substrate plane in scanning coordinates is known. In detailed scans this is used to correct for a tilted sample in the scan. A possible bending or non-planar distortion is neglected.

Confocal Fluorescence Microscope

Fluorescence generated in a point on the surface of the substrate and collected with the high NA objective is separated from reflected pump light with a series of a dichroic mirror and optical filters. Depending on the specific experiment conducted, the fluorescence light is investigated by a suitable measurement device. To use the apparatus as a confocal fluorescence microscope, the fluorescence can be focused into a fiber with the fiber aperture serving as the detection pinhole (see Fig. 4.2.b). The fiber is coupled to a single photon avalanche diode (τ-SPAD, PicoQuant). A time-correlated single photon counting (TCSPC) system (PicoHarp 300, PicoQuant) records its count rate, serving as a measure of intensity. By raster scanning the sample, fluorescence maps can be recorded.

Polarization Sensitive Confocal Fluorescence Microscope

To investigate the polarization state of the fluorescence a linear polarizer can be used as an analyzer. It is attached to a rotation mount. The intensity of the signal is then measured in dependence of the direction of the polarization axis of the analyzer. With this method, the analyzer angle can be changed in arbitrarily small steps. The method with the available manually operated mount has the disadvantage that it takes minutes to take a full set of polarization measurements for each scanning point. Taking a raster scanned map of the sample is not feasible. Rastering for different analyzer angles sequentially is an option that suffers from high sensitivity to overall small drifts of the fluorescence power. These fluctuation can for example be caused by slight mechanical movements of the sample. They would be falsely interpreted as a polarized signal.

In Fig. 4.4.a the measurement setup to automatically obtain a fluorescent map of the sample with information of the polarization state in a single scan is shown. The fluorescence light impinges on a polarizing beam splitter cube. It separates

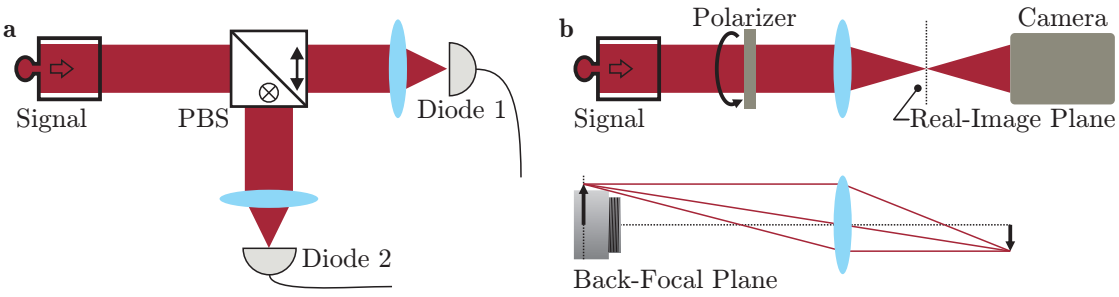

Figure 4.4: Two methods to investigate the fluorescence signal coming from the confocal microscope: **a** To investigate the polarization, a polarizing beam splitter (PBS) is used to split the light into two orthogonal polarizations. They can be measured simultaneously, when focused onto two avalanche photo diodes. **b** To record spatial information a lens forms an image on a camera. To gain information on the angular distribution, the back focal plane is imaged as sketched in the bottom.

the *s*- and *p*-polarization components of the light by reflecting the s component and transmitting the *p*-component. Each beam is focused onto an individual single photon avalanche diode (PDM, Micro Photon Devices). Their small active areas serve as detection pinholes of the confocal microscope. The count rates of both diodes are recorded simultaneously. In each scan a big patch with hundreds of quantum dots needs to be included. The fluorescence signal of this patch is unpolarized, due to averaging over many quantum dots. Both detectors should measure the same power here. Due to differences in the optical arms leading to the detector and slightly different efficiency of the diodes, the measured signal differs. Those differing signals are used to calibrate and normalize both detection arms to each other. This way it is ensured that the measured power ratio between the two channels stems from a polarized signal and not power fluctuation in time.

Fourier Imaging

The used high-NA microscope objective is infinity corrected. It does not form a real image of an object set in working distance. The working distance coincidence with the front-focal length such that the light from one point of the object is collimated behind the objective. To form an image of the sample a tube lens is needed. Since the object in the confocal case is a single point, the image formed by this tube lens is a single point, i.e., the focal point, as well. As sketched in Fig. 4.4.b the setup can be equipped with a scientific complementary metal-oxide-semiconductor (sCMOS) camera (Zyla, Andor). It is not placed in the real-image plane but rather such that there is a real image of the back-focal of the microscope

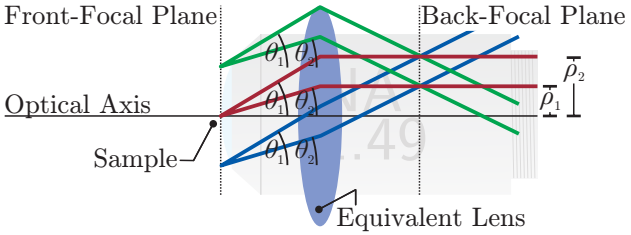

Figure 4.5: Schematic of Fourier imaging. The complex composite lenses of the objective (grayed out) are substituted by an equivalent single lens. Light rays originating from the same point in the front-focal plane are collimated behind the lens. The intersection length ρ of a ray with the back-focal plane only depends on the emission angle θ.

objective on the camera chip.

For an aplanatic objective lens, the spatial intensity distribution in the back-focal plane of the objective is related to the angular distribution of the collected light by the sine condition [118]. Light emitted under an angle in the front-focal plane gets mapped to a point in the back focal plane independent of its origin position. This principle is sketched with the help of an equivalent lens in a schematic in Fig. 4.5. Thus, an emission angle θ, measured with respect to the optical axis, corresponds to a distance $\rho = \sqrt{x_{\mathrm{cam}}^2 + y_{\mathrm{cam}}^2}$ from the optical image center on the camera chip:

$$\rho = \kappa \sin(\theta) \quad , \tag{4.3}$$

where κ is the conversion factor. The biggest angle θ_{NA}, which can be still collected with the objective, and hence be observed on the camera corresponds to the radius of a ring with $\rho_{\mathrm{NA}} = \kappa \mathrm{NA}/n_{\mathrm{g}}$. This relation is used with the known NA of the microscope objective to determine the conversion factor κ.

The data is presented in this thesis with a linear θ axis and not in the pseudo momentum space of the camera chip. Antenna data is commonly represented in spherical coordinates $(\theta,\ \varphi)$, where θ is the polar and φ the azimuthal angle. So, the transformation from the x_{cam} and y_{cam} coordinates of the camera chip to spherical coordinates reads:

$$\theta = \arcsin\left(\frac{\sqrt{x_{\mathrm{cam}}^2 + y_{\mathrm{cam}}^2}}{\kappa}\right) \quad , \tag{4.4}$$

$$\varphi = \arctan\left(\frac{y_{\mathrm{cam}}}{x_{\mathrm{cam}}}\right) \quad . \tag{4.5}$$

The choice of the orientation of φ is arbitrary. To investigate the polarization of the antenna signal, we place a linear polarizer as an analyzer in front of the camera.

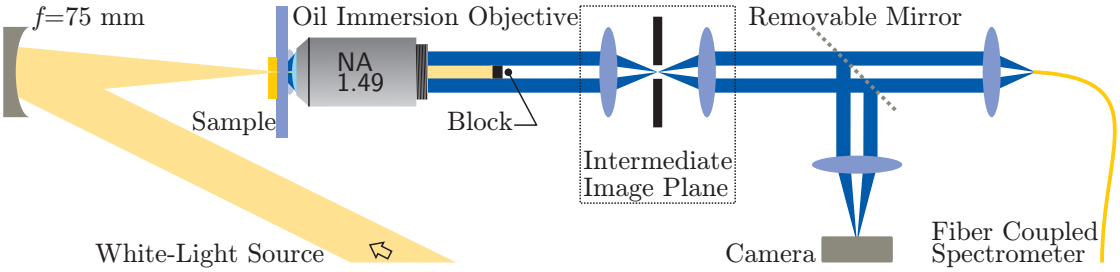

Figure 4.6: Schematic of the dark-field spectroscopy setup. A white-light source is focused with a long-focal-length concave mirror on the sample. The high-NA objective collimates the undisturbed white light (shown in yellow) and the scattered light (shown in blue). A circular block then blocks the undisturbed light. In an intermediate image plane a rectangular aperture crops the relevant image part. The light can be reflected by a removable mirror to produce an image on a camera or it is coupled to a fiber of a spectrometer.

4.2 Dark-Field Spectroscopy

The results on all active nanoantennas in this thesis are obtained on individual structures. A standard method to obtain spectral information of plasmonic structures is white-light-transmission spectroscopy, where a white-light source is focused onto the sample and the transmitted light spectrum ($I(\lambda)$) is compared to the transmission spectrum of the bare substrate $I_0(\lambda)$) to get the transmittance:

$$T(\lambda) = \frac{I(\lambda)}{I_0(\lambda)} = \frac{I_0(\lambda) - \Delta I(\lambda)}{I_0(\lambda)} \quad . \tag{4.6}$$

While this method is suitable for a lot of experiments, especially as a fast test bench measurement during sample fabrication, it shows some disadvantages. Since the extinction cross section of a single plasmonic structure is small [119], the intensity change $\Delta I(\lambda)$ is too. This small change has to be measured on top of a large background. In practice this means that the measurement has to be performed on an array of typically some hundred nominal identical structures [41]. Therefore, the obtained spectrum will suffer from ensemble averaging due to inhomogeneous realization of the single structures. Furthermore, lattice effects like Wood's Anomaly [120] can occur, interfering with the plasmonic resonances. Hence, to measure optical properties of single nanoparticles a dark-field spectroscopy approach has to be employed, where the background $I_0(\lambda)$ is suppressed. The background light (incident light) covers the same spectral range as the signal. Thus, it can not be done separated with spectral filters, and the light has to be spatially filtered [121, 122].

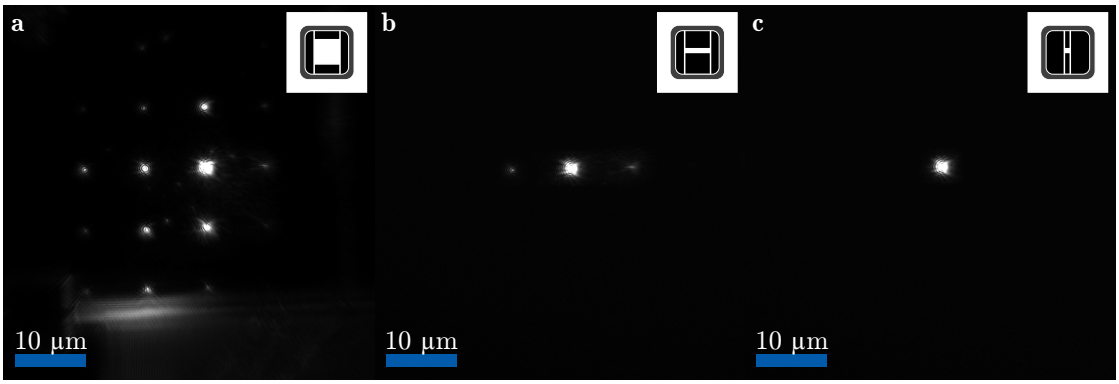

Figure 4.7: Dark-field microscopy images taken in preparation of the spectroscopy of single nanoparticles. **a** With the block behind the microscope objective a dark-field image is created. The scatterers appear bright, and edges on structures are emphasized. **b** and **c** With the adjustable, rectangular aperture in the intermediate image plane regions of interest can be selected.

The used measurement scheme is shown in Fig. 4.6. It is compatible with the existing confocal microscope such that the spectra of individual nanoantennas can be compared with fluorescence measurements in the same setup. A supercontinuum white-light laser (SuperK Versa, NKT Photonics) is focused on the sample with an on-axis concave mirror ($f = 75\,\mathrm{mm}$). The focused light beam exhibits a numerical aperture of NA$= 0.07$. The angle between the mirror symmetry axis and the impinging light needs to be as small as possible to generate a high quality focus. Due to physical constraints in the setup, i.e., the sizes of the sample substrate, its mount and the objective, the angle of incidence that is used is 6°.

In contrast to the other experiments described in this thesis, the laser is not fiber coupled and impinges the sample on the structured side of the sample. This way, dark-field spectroscopy can be obtained in the existing confocal setup, while the sample is mounted.

The sample is illuminated by the white laser light and the high-NA microscope objective collects and collimates the light. Due to the large ratio between the NA of the impinging light and the NA of the microscope objective, the white-light is collimated to a thin beam. Together with a tube lens in front of a camera the setup functions as a standard microscope in this configuration. This mode is used to locate the structure on the sample surface. A removable mirror can be detached such that the light is coupled into the input fiber of a grating spectrometer (Acteon SP2300 equipped with Pixis 256, Princeton Instruments). A small black plastic disk with a diameter of 3 mm is used as a beam block. It is mounted to a mechanical stage by a thin wire. It can be driven into the beam behind the high-NA objective

such that it is centered on the optical axis. It changes the operating mode of the microscope to dark field by blocking the undisturbed light, which is confined to a beam smaller than the disk's diameter. Ideally, without a scatterer on the sample, the image now would be black. In reality impurities in the substrate and surface roughness will contribute to a non zero background. Viewing the sample structure with the beam block yields images, where edges and small structures appear bright. An exemplary dark-field image of a calibration sample of gold nanodisks is shown in Fig. 4.7.a. The block can be seen as a high-pass filter in the Fourier plane, blocking all low spatial frequencies. Light that has been scattered on the sample is not confined to that small beam and can partially pass by the beam block.

In a measurement, the structure on the sample is located in bright-field mode. Then the beam-block is introduced and the scatterers, i.e., the nanoantennas, appear bright. With the rectangular aperture in the intermediate image plane the light from a single scatterer is isolated (example in Fig. 4.7.b-c). When the mirror is removed, the light is coupled to the fiber of the spectrometer. To obtain the scattering spectra of the nanoantenna, a reference spectrum needs to be recorded. Thus, the sample is moved such that the image of the nanoantenna leaves the region of interest and the beam block is removed. The recorded spectrum serves as the reference. The measured signal from the nanoantennas are divided by the the reference to account for the non-flat white-light spectrum. Absolute measurements of the scattering cross section are not possible with this method. However, keeping the region of interest the same size over all measurements provides scattering spectra that are comparable to each other.

Chapter 5

Active Plasmonic Nanoantennas

Plasmonic nanoantennas are used to gap the mismatch of the wavelength of light and the size of local emitters such as single molecules or quantum dots. They can be designed to mediate the coupling of small emitters to the far field and vice versa [9, 11, 26]. In receiving mode, nanoantennas can locally increase the light intensity by several orders of magnitude [14–16]. An emerging application is the sensing of small quantities of particles [34–37]. In transmitting mode, coupling of quantum emitters to nanoantennas allows for the control of the emission properties [24–27].

To engineer working devices a complete knowledge of the optical properties of the used nanoantennas is crucial. Thus, various techniques are used to characterize nanoantenna thoroughly that rely either on far-field or near-field measurements. There are both far-field measurements that work on individual nanoparticle [121, 122] and ensemble based methods [43]. With the latter, the obtained spectra suffer from ensemble averaging due to inhomogeneous realization of the single structures. Besides those methodical differences, the different techniques do not necessarily measure the same resonances. For example it is known that plasmonic nanoparticle's near-field properties peak at lower energies than the far-field quantities [38]. Moreover, a whole class of resonance can not be examined with standard far-field approaches. They usually rely on plane waves impinging at normal incidence and can only directly detect modes with a non-vanishing dipole moment. Thus, non-dipolar modes are considered to be dark [12, 39]. The investigation has lead to new effects and applications [12, 40–43]. A fundamental understanding of those modes is crucial and a variety of techniques is employed to make dark modes visible. Especially near-field methods, e.g., electron energy loss spectroscopy (EELS) or scanning near-field optical microscope do not show this constriction [43, 103]. In this chapter the results on dark-mode probing of plasmonic rod antennas using quantum dot fluorescence is presented. Gold rod nanoantennas are the model system, since they have a well known spectrum with an easily designable resonance wavelength and as discussed in Section 2.2.3 they exhibit both dipolar and non-dipolar modes. We compare spectra, taken with far-field spectroscopy of individual nanoantennas and quantum dot based near-field

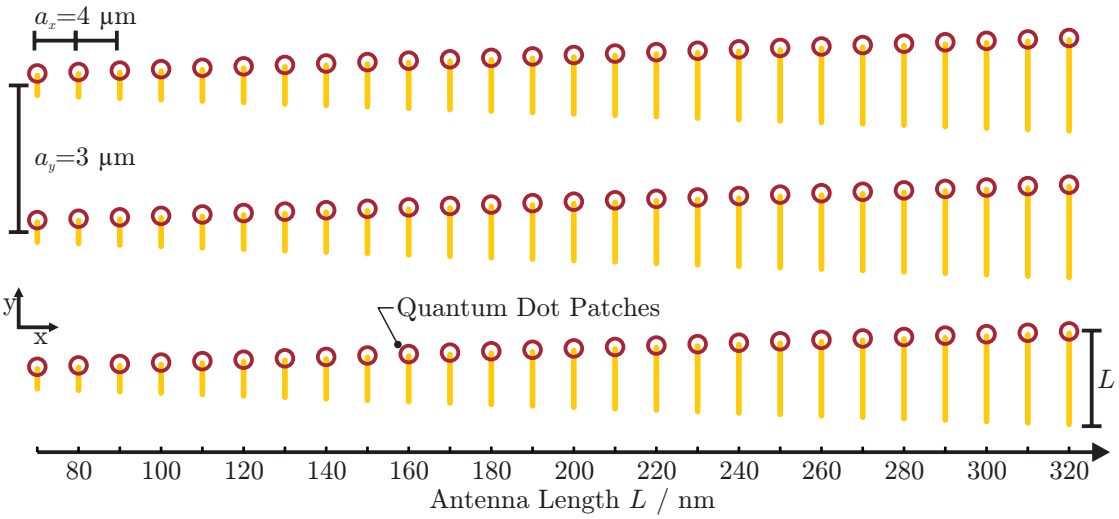

Figure 5.1: Not-to-scale sketch of the experimental sample design. The active nanoantennas are arranged on the sample in a grid structure. The antenna length is increased by 10 nm in x-direction, with a lattice constant of $a_x = 3\,\mu\text{m}$. In y-direction the antennas are repeated with $a_y = 4\,\mu\text{m}$. The red circles mark the quantum dot patches.

probing. With both methods we can identify the first mode, but only the near-field method succeeds to excite the second mode.

5.1 Sample Design

The active gold rod nanoantennas are fabricated by the two-step lithography method presented in Chapter 3. On the sample the individual nanoantennas are placed on a grid, each consist of a gold rod antenna and a 70 nm × 70 nm quantum dot patch centered at its tip. The grid has lattice constants $a_x = 3\,\mu\text{m}$, $a_y = 4\,\mu\text{m}$ such that the active nanoantennas can be addressed by focused light individually. The antenna length serves as the changing parameter in the experiment. To realize that, antennas of increasing length from $L = 70\,\text{nm}$ to $L = 320\,\text{nm}$ are fabricated. The length increases in 10 nm steps in x-direction of the grid such that there are 26 different antenna lengths. The height for the gold nanostructures is set by the evaporation process to $h = 40\,\text{nm}$. The nanoantennas' width is uniformly $w = 30\,\text{nm}$. Since the resonance wavelength scales linearly with the nanoantenna length, this creates a comb of resonances. This comb is repeated in y-direction without alteration.

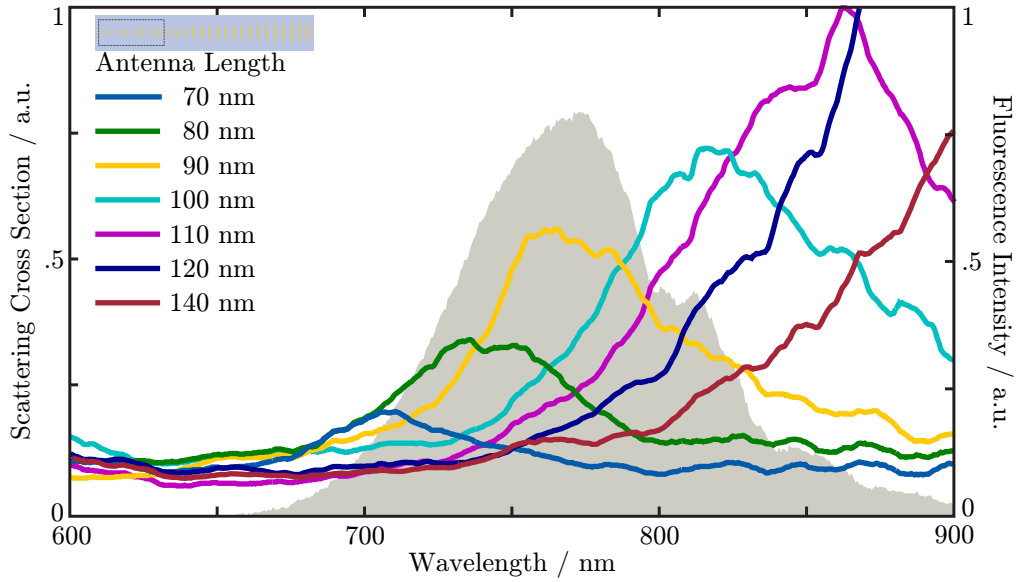

Figure 5.2: Scattering spectra of single gold nanoantennas. The resonance wavelength of the fundamental antenna mode for antenna lengths from $L = 70\,\text{nm}$ to $L = 140\,\text{nm}$ scans over the quantum dot fluorescence spectrum shown in gray.

5.2 Scattering Spectra

To measure far-field properties of individual nanoantennas, the dark-field scheme as described in Section 4.2 is used, where light impinging under normal incident is scattered by a single nanoantenna. The pump light is blocked spatially such that only the scattered light is recorded and compared to the exciting white-light spectrum. As described the sample is designed so that the nanoantennas can be addressed individually.

The obtain scattering spectra of seven individual antennas are shown in Fig. 5.2. The measured quantum dot fluorescence spectrum as introduced in Section 3.2.3 is shown as a gray area in the background. The measured scattering cross sections are all given in units relative to the maximum cross section of the $L = 110\,\text{nm}$ antenna. As expected the resonance wavelength increases from the shortest antenna with length $L = 70\,\text{nm}$ to the longest antenna $L = 140\,\text{nm}$, where the maximum is already outside the measurement range. The longer antennas have a higher scattering strength.

These resonances can be attributed to the fundamental antenna mode with a dipolar, longitudinal charge separation. The resonance position and their full width at half maximum are found with a Gaussian fit. The results are listed in Tab. 5.1. The resonance wavelength of the $L = 120\,\text{nm}$ antenna was read out

L / nm	70	80	90	100	110	120
λ_{res} / nm	704 ± 5	735 ± 2	763 ± 2	820 ± 5	859 ± 5	933 ± 15
$\Delta\lambda$ / nm	67 ± 3	64 ± 3	65 ± 5	86 ± 2	114 ± 4	—

Table 5.1: The table lists the wavelengths and widths of the fundamental resonances of the shortest six nanoantennas.

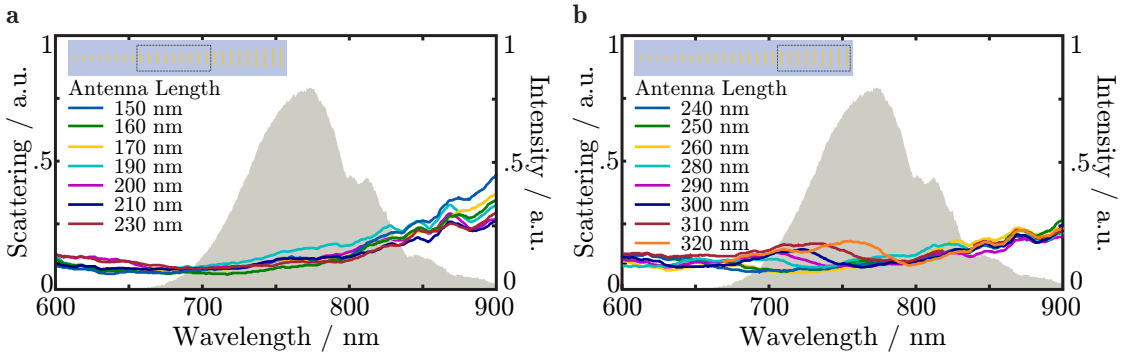

Figure 5.3: **a** Scattering spectra of single gold nanoantennas of medium sizes. The scattering increases for longer wavelengths, but there is no resonance at the quantum dot fluorescence spectrum (shown in gray). **b** Scattering spectra of single gold nanoantennas of large sizes. The scattering strength is comparable to the medium sized antenna. However, for the longest set of antennas a small resonance emerges that is barely stronger than the background scattering.

manually, since the signal in the infrared regime is to noisy for a fit. A linear regression to the maxima position of the shortest five antennas and comparison to eq. (2.34) yields:

$$L = \frac{1}{2}\lambda_{\mathrm{eff}} = \frac{1}{2}\left(p_1 + p_2\frac{\lambda}{\lambda_{\mathrm{P}}}\right) = \frac{1}{2}\left(-178\,\mathrm{nm} + 0.456 \cdot \lambda\right) \quad . \tag{5.1}$$

As the antennas get longer the measurement gets more challenging, since the fundamental resonance drifts out of the measurement range and the signal gets flat. The scattering spectra of seven medium sized antennas is plotted in Fig. 5.3.a. The spectra exhibit no resonance feature at the quantum dot fluorescence. There is however, scattering for longer wavelength. Since this increase gets smaller with larger antenna sizes, it can mainly be attributed to the tail of the very broad fundamental antenna mode in the infrared.

For the longest antennas as depicted Fig. 5.3.b, the scattering strength is comparable to the medium antenna case. For the antennas with lengths $L = 290\,\mathrm{nm}$, $L = 300\,\mathrm{nm}$, $L = 310\,\mathrm{nm}$ and $L = 320\,\mathrm{nm}$ however, a small feature shifts in from

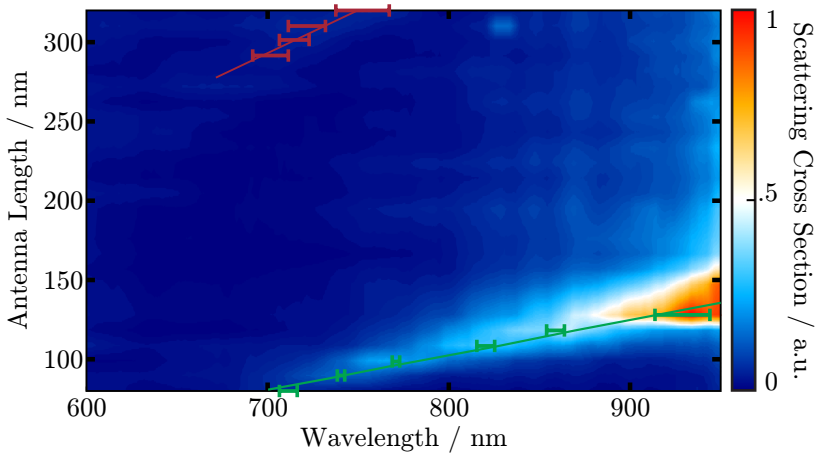

Figure 5.4: Extinction cross section of gold rod nanoantennas normalized to the overall maximum. As expected, the maxima of the fundamental resonance (green) shift to longer wavelength. The green line is a linear regression to the maxima. Barely over the detection limit the third-order maxima are visible (red). They can only be identified in the corresponding line scans. The linear regression shown in red has a higher slope.

small wavelength. Its height is just over the detection limit. This feature is identified to be the third-order resonance of the antenna. Only the resonance of the three longest antennas has a significant overlap with the quantum dot fluorescence, but is still remarkably smaller than the first-order resonances. The maxima positions were here just estimated since a fit is not feasible.

A plot of the complete data set combined and normalized to the overall maximum can be found in Fig. 5.4. The first and third-order maxima that were identifies in the spectra (Fig. 5.2 and 5.3) and the regression lines are shown to guide the eye. The behavior presented in this plot is similar to the numerical calculations shown in Fig. 2.4. As expected, there are no second-order resonances visible. The far-field excitation with plane waves under normal incident can not excite all antenna modes.

5.3 Fluorescence Enhancement

The scattering cross sections of the nanoantennas were investigated with dark-field spectroscopy. In order to get more insight in the functionality of the coupling between the quantum dot and the gold structure, i.e., investigating the active part of the system, the fluorescence is investigated. As a light source to excite

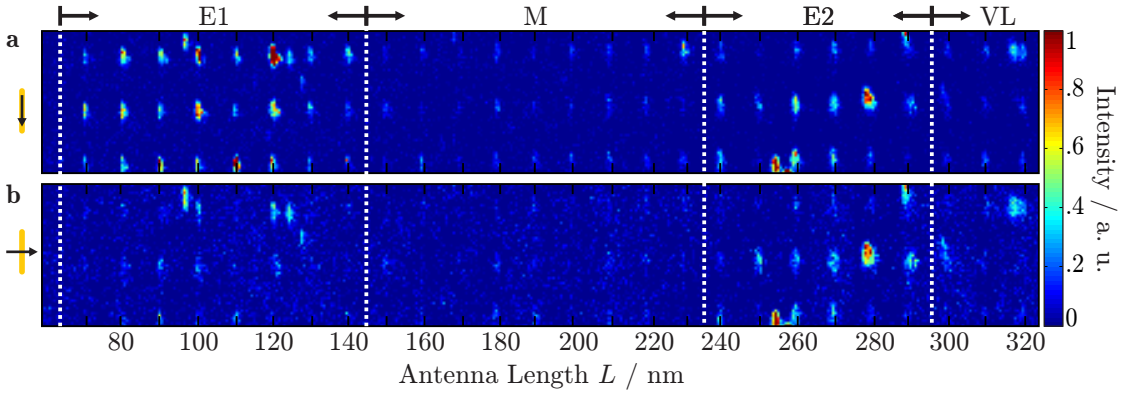

Figure 5.5: A polarization sensitive fluorescence scan of a sample with active nanoantennas with length from $L = 70\,\text{nm}$ to $L = 320\,\text{nm}$. Four regions can be identified: short active antennas show an enhanced fluorescence signal (E1) compared to the medium sized (M), the fluorescence of longer active antenna is enhanced again (E2) in comparison to the longest set of antennas (VL). **a** The fluorescence of the antennas with polarization parallel to the antenna shows more prominent enhancement behavior compared to (**b**) the antenna fluorescence with polarization perpendicular to the antenna, which is overall weaker.

the quantum dots a blue pump laser ($\lambda = 450\,\text{nm}$, PiL044X, Advanced Laser Diode Systems) is used. It is operated at a repetition rate of 500 kHz. A suitable dichroic mirror (Beamsplitter T 510LPXRXT, AHF) and optical filters (794/160 BrightLine HC, AHF; FGL550, Thorlabs) are chosen to filter the pump light from the fluorescence detection arm of the setup. Here it is divided into two orthogonal polarizations states by a beam splitter. Each part beam of the is focused onto an individual single photon avalanche diode (Channel 1 and 2). Since light emitted via the antenna mode is polarized (see Section 2.2.3), a difference in both channels is expected. The measurement setup is sketched in (Fig. 4.4.a).

The scan region is $90\,\mu\text{m} \times 40\,\mu\text{m}$ with a step size of 200 nm. During the scan the samples position was corrected for a sample tilt with resulting slope of 12 nm/µm in x-direction and 8 nm/µm in y-direction. The region of interest around the active nanoantennas is $80\,\mu\text{m} \times 12\,\mu\text{m}$, but the scan region is chosen larger to include a patch of quantum dots without an underlying nanostructure. Here, the average count rates of both channels over an area of $5\,\mu\text{m}^2$ is used to normalized both channels. Due to the large number of emitters, the fluorescence here is unpolarized and both channels should record the same average count rate. In reality those signals differ by 4 %, which is accounted for in the analysis. The difference stems from unequal coupling efficiency to the active areas of the diodes.

The corrected signal from both diodes – channel 1 and 2 – are shown in Fig. 5.5.a and .b, respectively. Channel 1 detects the fluorescence intensity of polarization state parallel to the antenna axis, while channel 2 records the perpendicular state. The plotted area represents the sample design discussed before and sketched in Fig. 5.1. Each column consists of three nominal identically active plasmonic nanoantennas made from a gold nanorod with a patch of quantum dots attached. In 26 columns the length of the gold nanoantenna is increased in 10 nm steps. The grid formed by the fluorescence of the 78 active antennas can be identified. The elongated form of the fluorescence points is not to be interpreted as an image of the structure of the nanoantennas, since the size of the smallest antennas is below the theoretical resolution limit of the microscope. It rather represents the point spread function of the system, indicating a slightly elliptical focus on the sample. The background signal is mostly dominated by the dark count rate of the diode and auto fluorescence of the immersion oil and glass.

Four regions can be identified: The fluorescence signal of the shortest active antennas ($L \leq 140\,\text{nm}$) (E1) is clearly enhanced compared to the signal of the medium sized (150 nm to 230 nm) active antennas (M), the fluorescence of longer (240 nm to 300 nm) active antenna is enhanced again (E2) in comparison to the longest ($L > 300\,\text{nm}$) set (VL).

The first enhancement region E1 coincides with the first plasmonic resonance overlapping with the quantum dot fluorescence as shown in Fig. 5.2. Thus, the increased signal can be attributed to the quantum dot fluorescence being enhanced by the available antenna modes. This is supported by the much lower signal in channel 2. The observed slight enhancement in this perpendicular fluorescence state can be attributed to the non-perfect extinction ratio and primarily a slight tilt in between antenna and polarizer axes. As the overlap for the antennas of length 130 nm and 140 nm gets smaller, so does the enhancement of the fluorescent signal. The uniformity of the fluorescence strength of the medium sized antennas in region M further supports the interpretation of an enhancement by the local density of states altered by the plasmonic antennas: The antennas of those sizes do not exhibit a scattering cross section overlapping with the quantum dot fluorescence (see Fig. 5.3.a).

However, the fluorescence enhancement for the antennas in E2 does not correspond to a resonance measured in the scattering cross sections (see Fig. 5.3.b). Interestingly, for the longest set of antennas (VL), where the fluorescence is not enhanced, an emerging feature was observed in the scattering cross sections. These features were attributed to the third-order resonances. They just start to overlap with the quantum dot fluorescence with the 300 nm antenna, where the fluorescence enhancement decreases already. Additionally, the measured third-order resonances are just barley stronger than the background signal. Thus, the fluorescence enhancement E2 does not coincide in strength or spectrally with the third-order

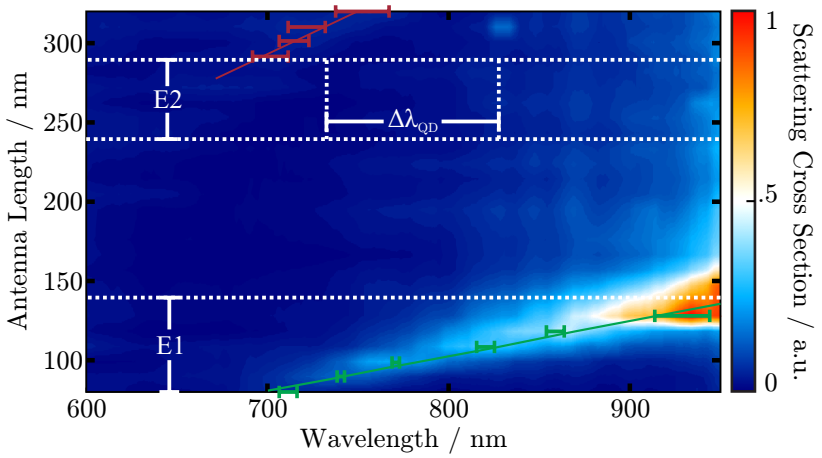

Figure 5.6: An illustration of the observed fluorescence enhancement layed over the measured extinction cross section of gold rod nanoantennas. The dashed lines limit the antenna length region, for which the fluorescence is enhanced (E1 and E2). The width of the quantum dot fluorescence is marked.

mode. Hence, it can be deduced that the fluorescence was enhanced by an antenna mode, which can not be excited in far-field measurements.

An illustration of the position of the excited dark modes can be found in Fig. 5.6. On the scattering cross section map, measured with dark-field spectroscopy, the two regions of the enhancement E1 and E2 is depicted. The width of the quantum dot fluorescence is marked. The limits of E2 and the quantum dot fluorescence form rectangle. It is this estimated region where the dark mode and quantum dot fluorescence should overlap significantly. This region is distinct from the measured far-field resonances and lays between the first and third-order mode so that it is reasonable to conclude that the enhancement is due to the dark, second-order antenna mode.

To support this argumentation discontinuous Galerkin time domain calculations were performed. In those calculations Maxwell's equations are solved on a discretized mesh. The calculations presented here were carried out by Julia Werra from the group of Kurt Busch in Berlin. Details on the used method can be found in [123]. The vicinity of a gold nanoantenna alters the decay rate of a dipole. To calculate this, the Poynting flux through a sphere containing the dipole and the antenna is recorded and compared to the flux through a sphere just containing the emitter. As the emitter's spectrum the measured quantum dot fluorescence is put into the calculation. The gold nanoantennas are assumed to have a rectangular footprint and a decreasing cross section in height. The dipoles were set at various positions around the tip of the antenna and the decay rate calculated for three

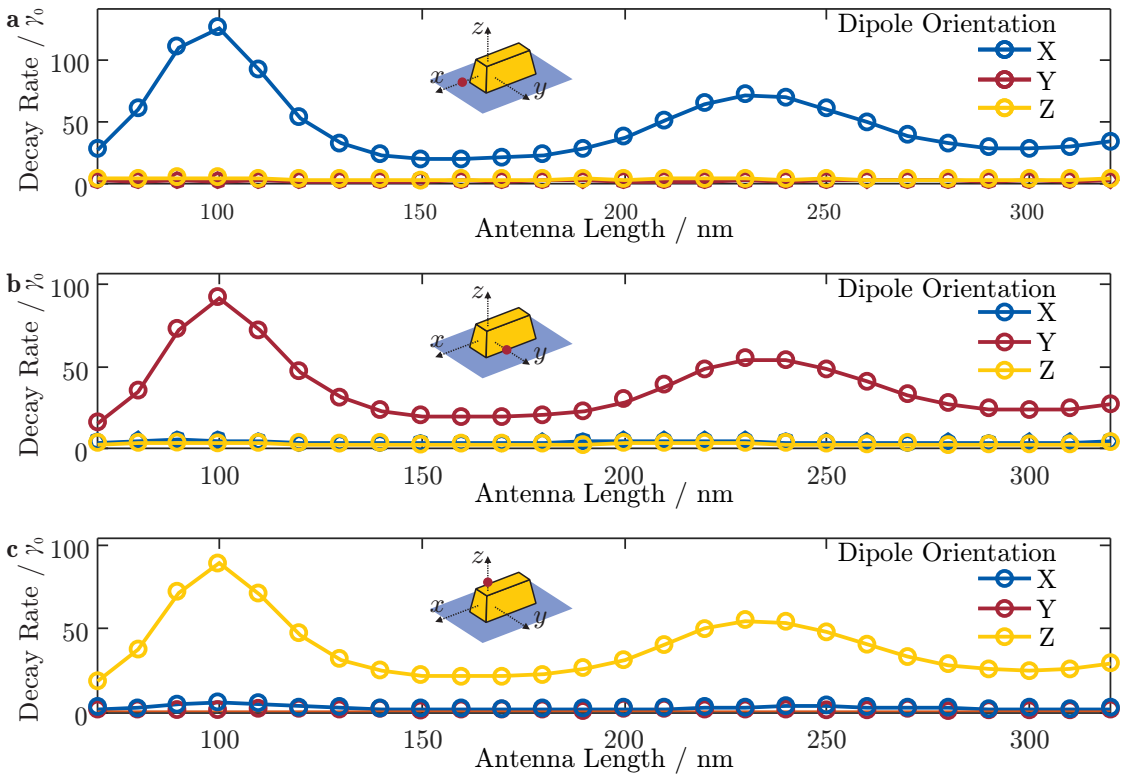

Figure 5.7: Numerical calculation of the decay rate of dipoles coupled to plasmonic nanoantennas carried out by collaborators. The rate is given in units of the decay rate of a bare emitter γ_0. The calculation were performed for three dipole orientations parallel to the coordinate axes at three different positions: **a** $\Delta x = 10\,\mathrm{nm}$ distance from the short bottom edge of the antenna, on the symmetry axis of the antenna $\Delta y = 0\,\mathrm{nm}$ and $\Delta z = 15\,\mathrm{nm}$ above the substrate; **b** at $\Delta x = -20\,\mathrm{nm}$ distance from the short bottom edge, at $\Delta y = 15\,\mathrm{nm}$ distance from the long bottom edge and $\Delta z = 5\,\mathrm{nm}$ above the substrate; **c** at $\Delta x = -10\,\mathrm{nm}$ distance from the short bottom edge, on the symmetry axis $\Delta y = 0\,\mathrm{nm}$ and $\Delta z = 5\,\mathrm{nm}$ above the antenna.

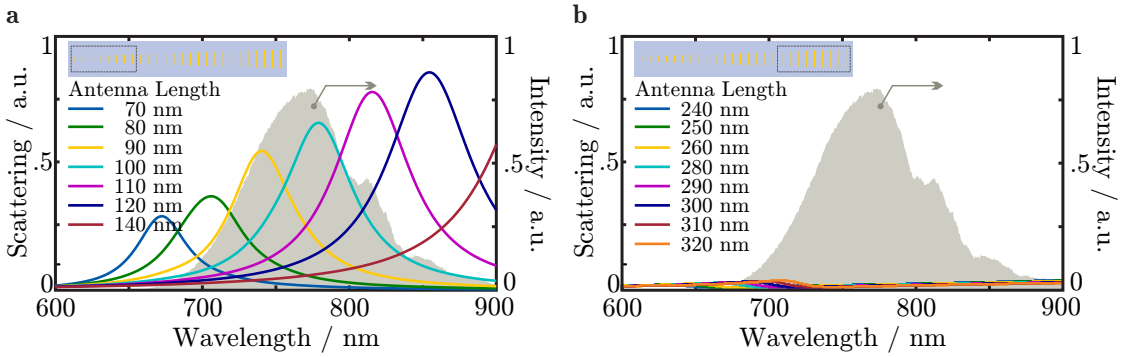

Figure 5.8: Calculated scattering spectra of single gold nanoantennas of medium (**a**) and large (**b**) antennas. As the in the experimental results, the second fluorescent enhancement region (E2) does not coincides with resonance obsverable in th scattering spectra. Additionally for the longest antennas, the third-order resonance becomes observable.

different dipole orientations parallel to the coordinate axes. Those calculations were performed for a set of 26 antennas from $L = 70\,\text{nm}$ to $L = 320\,\text{nm}$ as in the experiment.

The decay rate of dipoles at three characteristic positions can be found in Fig. 5.7.a-c, with a sketch of the antenna geometry in an inset. The rate is given in units of the decay rate of a bare emitter γ_0. The results for all dipole positions is similar, just with interchanged orientations. The affected and modulated dipole orientation is always the one pointing towards the antenna. As in the measurements, there are two regions of enhancement identifiable: One for of small antennas (E1) and one for longer antennas (E2). Even though the regions are slightly shifted compared to the experimental findings in regards of the antenna length, the qualitative behavior is strikingly similar. The shift can be attributed to the geometry of the antennas differing from the experimental realization.

As in the experiment, the near-field findings can be compared with the scattering cross section of the antennas. They were calculated by assuming a plane wave impinging on the antennas. The calculated spectra for the smallest and longest antennas are shown in Fig. 5.8.a and .b, respectively. The medium sized antenna' cross section are neglectable. As expected, there is no dipolar mode overlapping for the second fluorescence enhancement. Similar to the experimental findings, for the longest antennas a small feature is observable, which can be attributed to the third-order resonance. Again, those third-order modes do not coincidence in strength or spectrally with the the second fluorescence enhancement. Thus, the numerical calculation support our experimental findings qualitatively.

In conclusion, a comparison of far-field measurements with fluorescence mea-

surements shows that the fundamental dipolar mode of an antenna enhances the fluorescence. A second enhancement region could be explained by an enhancement due to the third-order dark mode. Thus, this measurement is a proof of principle of a direct detection of dark modes in nanostructures.

Chapter 6

Active Dielectric Nanoantennas

The results on active dielectric nanoantennas have been published and their presentation in this chapter follows closely the paper [124].

The active nanoantennas discussed in Chapter 5 rely on plasmonic resonances and thus, fall in the category of resonant antennas. In radio and microwave technology a second category of traveling-wave antennas is known. Antennas that do not rely on resonances exhibit some interesting properties, e.g., broadband operation [44]. In contrast to resonant nanoantennas, traveling-wave antennas operating at optical frequencies have been studied considerably less. However, there is a growing interest in transferring the traveling-wave concept to higher operating frequencies in order to achieve non-resonant broadband operation [45–47].

This chapter deals with an active, dielectric, leaky-wave antenna for optical frequencies with high directivity. The antenna design consists of only two simple dielectric building blocks and has a total length of approximately three times the free-space operation wavelength. It can be easily adapted to various low-loss dielectric materials. Moreover, its non-resonant nature makes the antenna design inherently robust against fabrication imperfections and guarantees broadband operation.

6.1 Antenna Design

The antenna design was proposed by a collaborating group of the University of Paderborn. One design goal was a feed region feasible for quantum dot deposition [125]. As a material hafnium dioxide was chosen. Hafnium dioxide is transparent for visible light and has a refractive index of 2 in the visible regime [48]. As it is established in semiconductor industry [126], it is ideal for adaptation for applications. The waveguide – in antenna context called director – has a designed rectangular cross section of $180\,\mathrm{nm} \times 600\,\mathrm{nm}$ and a length of 2200 nm. The propagating mode inside the director is fed by end-fire coupling with quantum dots

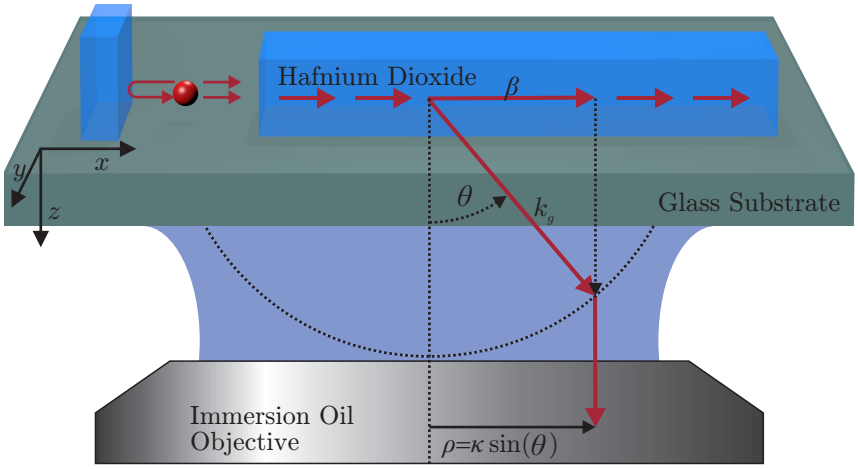

Figure 6.1: Schematic representation of the operating principle of the dielectric nanoantenna. The intensity distribution in the back-focal plane of the collecting objective is related to the angular distribution of emitted light by the sine condition.

placed next to it. The cuboid with footprint of 180 nm × 785 nm next to the director is called reflector. Reflector and director are separated by the 260 nm wide feed gap. The operating principle of the active nanoantenna is shown in Fig. 6.1 and can be qualitatively understood as follows: The fluorescence of the quantum dots excites a leaky mode in the director by end-fire coupling. Light propagating along the director is continuously coupled to radiating modes in the substrate and emitted into the glass under an angle $\sin(\theta_{\mathrm{beam}}) = \beta/k_{\mathrm{g}}$ relative to the substrate normal, i.e., the optical axis. Emission into the air is prohibited since the phase velocity of the guided wave is smaller than that of light in air. To increase the gain of the antenna, the reflector redirects fluorescence emitted in the backward direction. The active dielectric nanoantennas are fabricated by electron-beam lithography as described in Chapter 3. An electron micrograph of one dielectric nanoantenna is shown in Fig. 6.2.

6.2 Imaging of the Back-Focal Plane

In the optical experiments, a blue pump laser ($\lambda = 450$ nm) is focused by a high-numerical-aperture objective (100× magnification, NA = 1.49) through the substrate onto a single antenna to excite the quantum dots in the feed gap. The fluorescence emitted by this active antenna is collected with the same objective and separated from reflected pump light by a dichroic mirror (Beamsplitter T 510LPXRXT, AHF) and a series of optical filters (794/160 BrightLine HC, AHF;

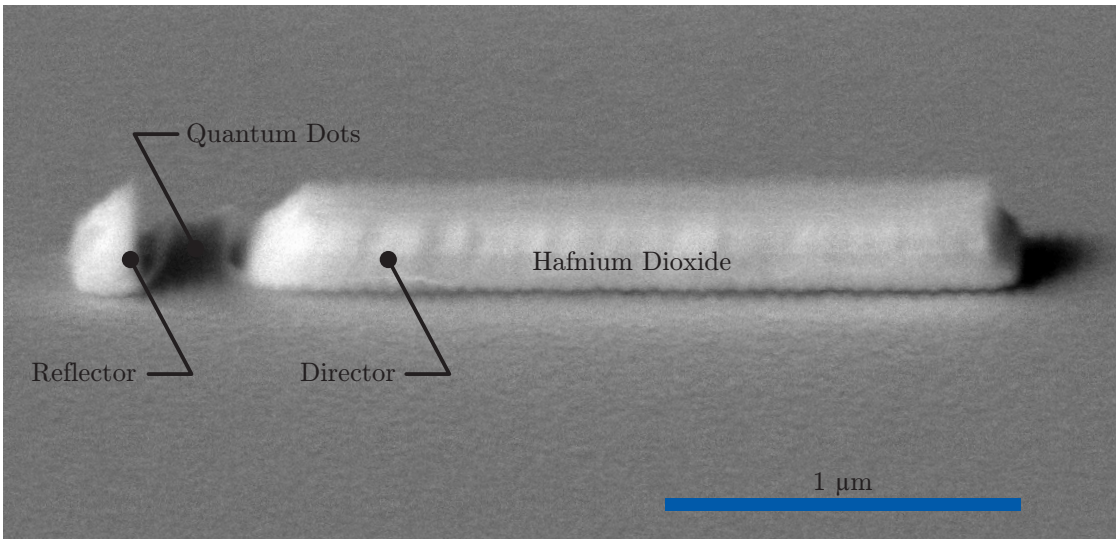

Figure 6.2: Scanning electron micrograph of an active hafnium dioxide nanoantenna. It consists of two 180 nm thick hafnium dioxide elements: The reflector has a designed footprint of 180 nm × 785 nm and the director of 2200 nm × 600 nm. They are separated by a 260 nm wide feed gap. The quantum dots in the feed gap are not visible.

FGL550, Thorlabs). For our aplanatic objective lens, the spatial intensity distribution in the back-focal plane of the objective is related to the angular distribution of the collected light by the sine condition. A lens creates a real image of the back-focal plane on a scientific complementary metal-oxide-semiconductor (sCmos) camera. The largest angle θ_{NA} that can be still collected with the objective and hence be observed on the camera corresponds to the radius of a ring with $\rho_{\mathrm{NA}} = \kappa \mathrm{NA}/n_{\mathrm{g}}$. This relation is used with the known NA to determine the conversion factor κ. In this analysis, the orientation of the coordinate system is chosen such that the antenna axis points in the ($\theta = 90°$, $\varphi = 0°$) direction and the optical axis corresponds to the ($\theta = 0°$) direction.

6.3 Angular Intensity Distributions

Figure 6.3.a depicts the normalized angular intensity distribution emitted by the active dielectric nanoantenna shown above. Here, the analyzer axis is set perpendicular to the antenna axis, i.e., we record the emission of a TE-polarized leaky mode (see inset). The active antenna shows a highly directional emission with a strong main lobe at ($\theta_{\mathrm{max}} = (70 \pm 2)°$, $\varphi_{\mathrm{max}} = (0 \pm 3)°$). This lobe has a full width at half maximum of $\Delta\theta_{\mathrm{max}} = (9 \pm 2)°$ and $\Delta\varphi_{\mathrm{max}} = (24 \pm 4)°$. Because of

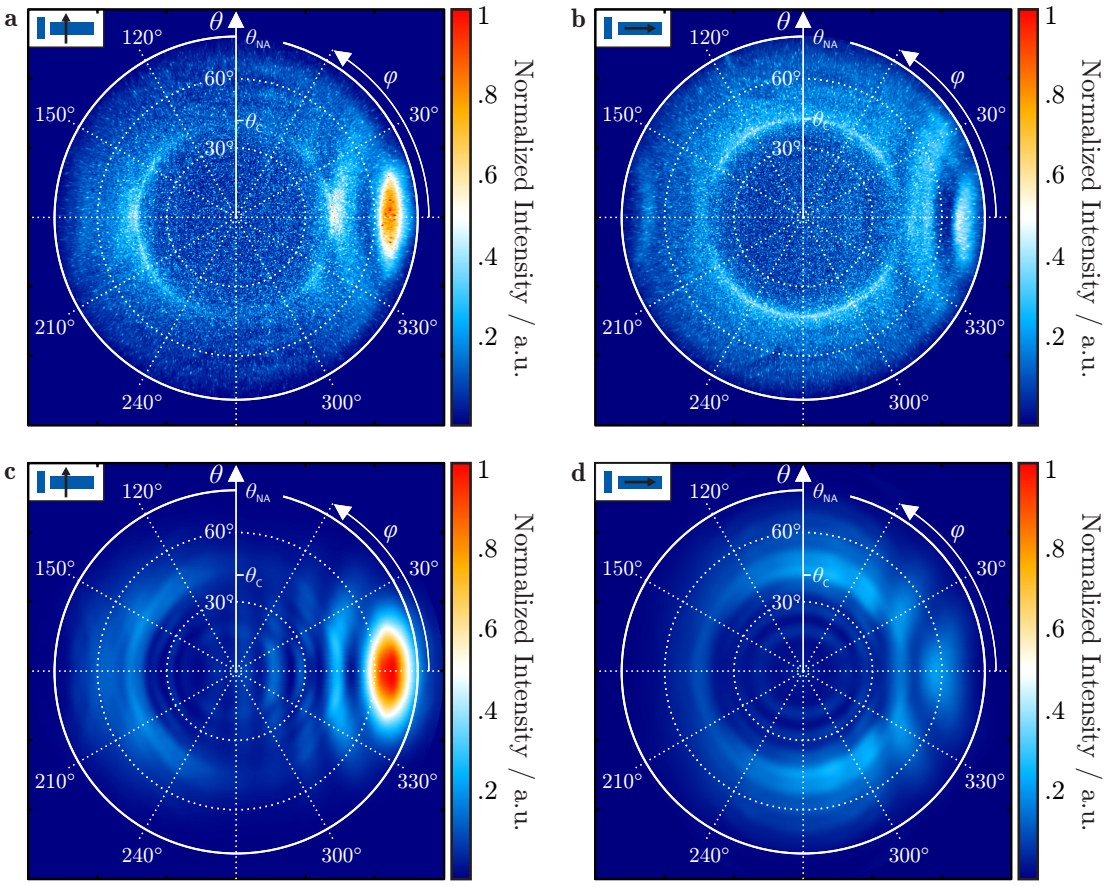

Figure 6.3: **a** and **b** Measured angular intensity distributions of an active dielectric nanoantenna for two different analyzer settings (see inset) normalized to the same value. The main-lobe maxima in both distributions are at $\theta_{\mathrm{max}} = 70°$. The central ring-like feature is attributed to dipoles not coupled to the antenna emitting directly into the substrate. The white circles at $\theta_{\mathrm{NA}} = 79°$ mark the experimentally accessible angular range. The calculated intensity distributions for the corresponding analyzer settings in **c** and **d**, show a similar behavior as the experimental data.

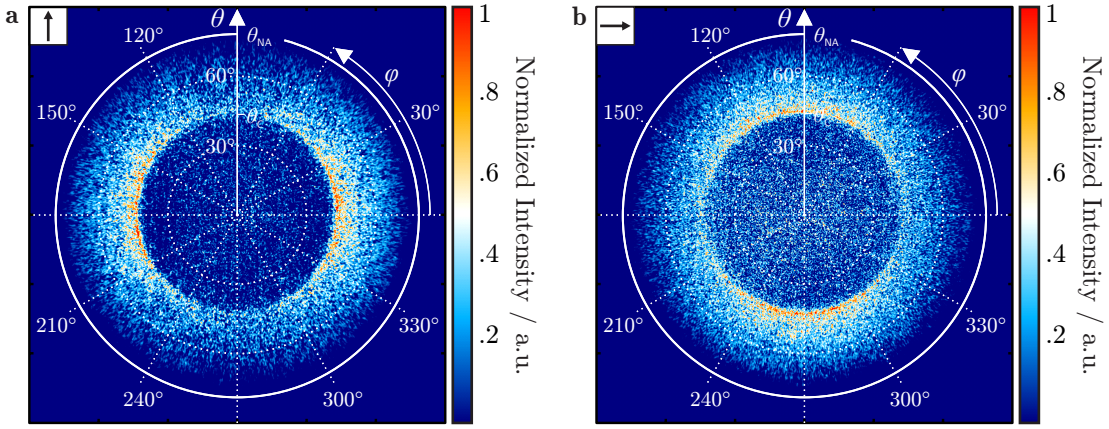

Figure 6.4: Measured angular intensity distributions of a bare quantum dot patch. The insets indicate the orientation of the analyzer.

the finite length of the director, additional concentric side lobes around the main lobes are visible.

A reference measurement of the angular intensity distribution of a bare quantum dot patch without nanoantennas is shown in Fig. 6.4. The emission follows the expected pattern of emitters close to a surface as discussed in Section 2.3.4. Similar to the antennas pattern, the enhanced feature on the critical ring rotates with the analyzer. It indicates that the weak circular feature at $\theta \approx \theta_c = 41.1°$ seen in the antennas pattern can be attributed to uncoupled quantum dot fluorescence, which preferentially emit at the critical angle between air and glass [10].

The directivity D of an antenna was defined in Section 2.2.1 as the ratio of the peak intensity and the intensity averaged over all directions as observed in the far field. The collection angle in our experiment is limited by the NA of the microscope objective, i.e., light emitted by an angle larger than $\theta_{NA} = 79°$ is not detected. As a result, a part of the intensity distribution is cut off. To estimate the directivity, it is assumed that the average intensity emitted into not detected angles equals the average intensity in the detected area. This assumption is reasonably, since it will not overestimate the directivity. The antenna is designed to emit into the detected angle range and in the numerical calculations there is no emission lobe into air. Additionally, as discussed in Section 2.3.4 even uncoupled quantum dot, emit most power into the detection angle range. With those restriction in mind, the directivity of the antenna over the measured part of the distribution can be estimated to be $D = 12.5\,\mathrm{dB}$.

In order to compare the performance of our antenna with previous works on nanoantennas, we additionally use the front-to-back ratio (FBR), defined [25] as the intensity ratio between the maximum at $(\theta_{max},\ \varphi_{max})$ and the opposing point

($\theta_{\max}$, $\varphi_{\max} + 180°$), to quantify the directional performance of our active antenna. The FBR value of the dielectric nanoantenna measured here is 12 dB. This value is quite competitive in comparison with plasmonic nanoantennas: for example Curto *et al.* reported a FBR value of their plasmonic Yagi-Uda nanoantennas of 6 dB [25].

The angular intensity distribution for the analyzer axis parallel to the antenna is shown in Fig. 6.3.b. It is normalized to the same value as the data discussed above. The peak intensity as well as the directivity ($D = 9\,\mathrm{dB}$) are in this case smaller than that recorded for the perpendicular analyzer setting (compare Fig. 6.3.a and .b). A plausible explanation for these observations is that the coupling of the quantum dots to the TM-polarized leaky mode is less efficient. This interpretation is consistent with numerical calculations.

To support the experimental findings, André Hildebrandt from the group of Jens Förstner in Paderborn performed numerical calculations based on finite integration technique (FIT) using CST Microwave Studio [127]. A single dipole in the feed gap served as the active element and three different perpendicular dipole orientations along the coordinate axes were assumed in successive calculations. Each dipole orientation is sketched in Fig. 6.5.a–c as the head of a column. For each dipole orientation, the far-field intensities for the two analyzer settings used in the experiments were evaluated separately. Finally, the intensities of the three dipole-orientations are summed for each analyzer setting. With this procedure, we simulate the ensemble of quantum dots with random dipole orientations as used in the experiment. The calculated intensity distributions for both analyzer settings are shown in Fig. 6.3.c and 6.3.d. They feature the same main and side lobes as the experimental data. The corresponding directivities for the analyzer in the y- and x-direction are $D = 14.05\,\mathrm{dB}$ and $D = 8.347\,\mathrm{dB}$, respectively.

The numerical results can be used for a detailed analysis of the contribution of different dipole orientations to the antennas pattern. The calculated angular intensity distributions for the six possible combination of dipole orientations and analyzer setting are shown in Fig. 6.5. The sketches in the top row (a–c) depict the assumed dipole orientation for the respective column. The first row (d–f) shows the intensity distributions for the analyzer parallel to the antenna axis and the second row (g–i) the distributions for the perpendicular analyzer setting. The contribution to the overall distribution of the dipole orientated in z-direction (a) is neglectable. As expected a dipole oriented along the waveguide direction does not couple to an antenna mode, since it does not radiate in direction of its axis (Section 2.2.1). There are two main contributions to the main lobes: (h) the dipole oriented along the y-direction couples primarily to the TE leaky mode and (f) the dipole oriented along the z-direction predominately excites the TM leaky mode. A comparison of these two cases shows that the coupling efficiency to the TM mode is smaller, resulting in a lower directivity for light polarized along the antenna axis as seen in the experimental data.

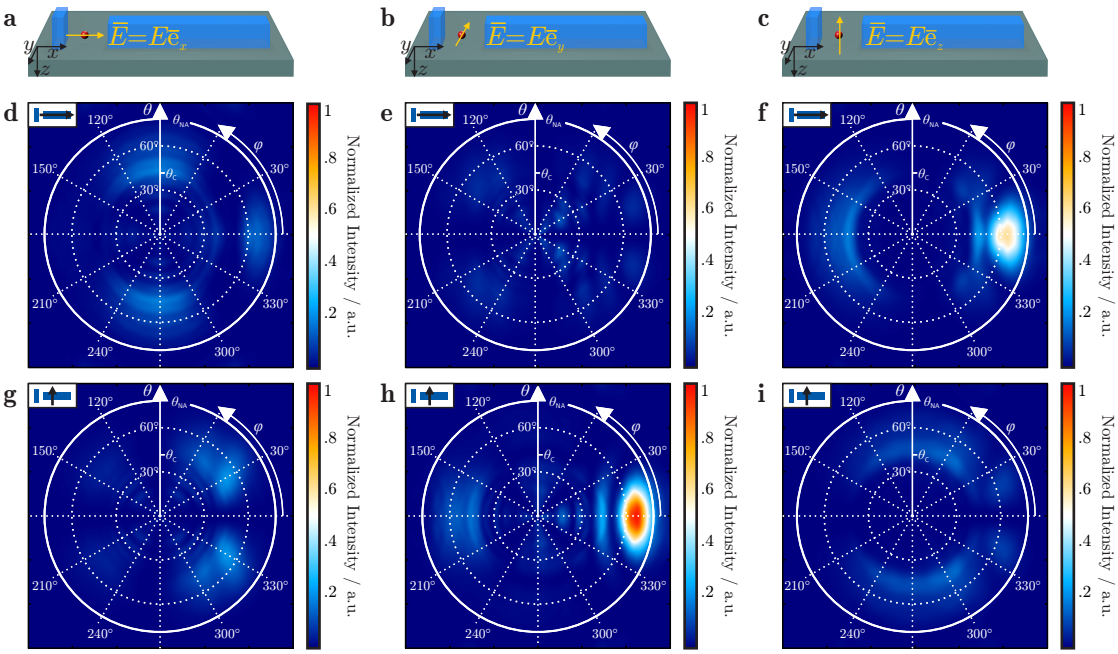

Figure 6.5: Detail analysis of the numerical calculations. Each column shows the contribution of one of three dipole orientations (**a**–**c**) to the angular intensity distribution. In the first row (**d**–**f**) the results for the analyzer parallel to the antenna axis and the second row (**g**–**i**) for the perpendicular analyzer setting. **f** and **h** show the main contributions to the lobe.

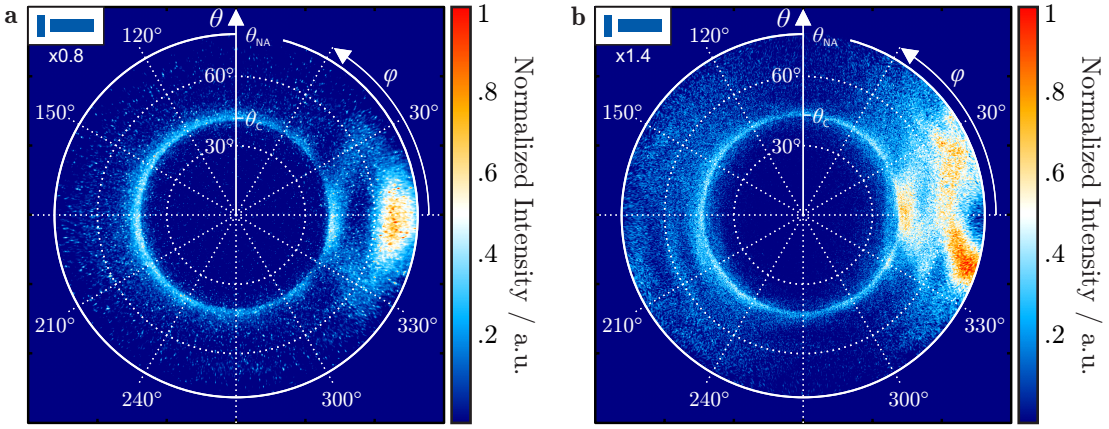

Figure 6.6: Angular intensity distribution of dielectric antennas without analyzer with footprints **a** 0.8× and **b** 1.4× as large as the original design. The white circles mark the experimentally accessible angular range.

6.3.1 Size Variation

A main advantage of non-resonant antennas is their high bandwidth and robustness against fabrication imperfections. To investigate that property, antennas with geometries that do not correspond to the original design are fabricated. Their footprint is 0.8× or 1.4× as large as the original antenna. Since the height is set for the whole sample by the evaporation process, it was not scaled. We anticipate that the far-field pattern of the antennas will differ from the one measured for the original design, but still exhibits a directional emission into the designed forward direction. The changed footprint leads to a different director cross section and thus a different propagation constant β. According to eq. (2.40) there will be directivity into the forward direction as long as there is a propagating mode supported in the director with a propagation constant smaller than the wavenumber of the substrate.

As expected, both antennas still show directional emission (see Fig. 6.6.a and .b). The results show the combination of both polarization states without an analyzer. The features in the pattern of the smaller antenna resembles the ones seen in the pattern of the original antenna. A main lobe concentrates the intensity in a small solid angle. The beam direction $\theta^{\mathrm{S}}_{\mathrm{max}} = (68 \pm 3)^\circ$ is only slightly smaller than the one of the original design. The estimated directivity is $D^{\mathrm{S}} = 7.5\,\mathrm{dB}$. The pattern of the large antenna is significantly different. The form of the angular region of highest intensity resembles the side lobes seen in the original antenna. A possible explanation is that the main lobe is at an angle larger than the maximal detectable angle of the microscope. Hence, the estimated directivity $D^{\mathrm{B}} = 6.2\,\mathrm{dB}$ is smaller.

Even though the directivity of both antennas is smaller than the one for the

original antenna, we deduce that the variation of the antenna dimensions results in a different beam direction but not a total loss of the antenna's functionality. This behavior agrees well with the numerical calculations, which predict a plateau of high directivities for a broad range of the widths and lengths around the original design [125].

The performed experiments show that the antennas made form lossless hafnium dioxide exhibit highly directional emission.

Chapter 7

Outlook

Fabrication Method

The results that are presented in this thesis use the quantum dots as a bright dye with high quantum yield as a feeding source of the antenna. For future projects that involve coherent interactions of quantum dots, e.g., moderated by a long plasmonic antenna, a precise placement of single emitters is necessary. We believe that even with the inherently statistical placement method, it is feasible to reliably place single quantum dots with a high probability. Therefore, currently a master thesis investigates the parameters of the deposition technique. A Hanbury Brown and Twiss experiment added to the existing optical setup will be used to clearly demonstrate the placement of single emitters by measuring anti-bunching. Furthermore, we believe the technique can be adapted to different types of quantum emitters, e.g., nano diamonds with a color center, as long as their surface can be chemically modified.

A succeeding project will study the coupling of small ensembles of quantum emitters to an electromagnetic environment tailored by metallic nanostructures. Those experiments will have to be conducted at cold temperatures, to unbroaden the line width of the emitters.

Even though, the results presented in this thesis focus on individual nanostructures, the chosen fabrication methods are already suitable for processing of large scale composite materials. A large array of active nanoantennas could serve as an active thin film with higher light intensity for real life applications.

Active Plasmonic Nanoantennas

The second order mode, excited by the quantum dot fluorescence, is non-dipolar. Using the Fourier imaging method implemented for the measurement of the dielectric antennas, the far-field pattern of the resonance could be characterized. We expect it to be distinct from the far-field pattern of a dipolar mode. In an application this could be used to separate the fluorescence of different wavelength spatially.

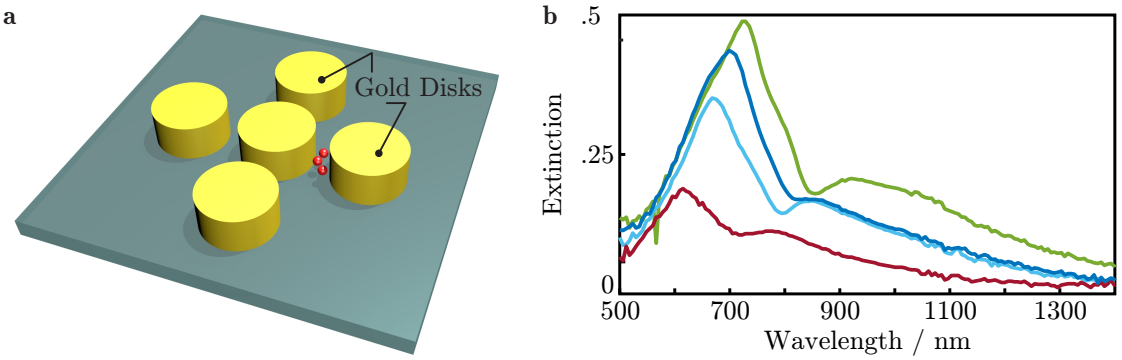

Figure 7.1: **a** An example for a more complex structure to be investigated with quantum dot fluorescence is a pentamer made from five gold nanodisks. They exhibit a sharp feature in their extinction spectrum as shown in a measurement in (**b**) called a Fano dip originating from the overlap of a sharp dark and a broad bright mode. By placing the quantum dots at different positions next to the pentameter the modes could potentially be excited selectively.

Gold rod nanoantennas are a basic structure and were used in this thesis as a model system to show that dark modes can be excited with the described near-field method. The approach to gain information over a nanostructure by probing its near field with quantum dot emission is a promising way to investigate more complex structures.

Fano resonances have been used before to investigate dark modes of plasmonic structures. For example, a pentamer consiting of five gold nanodisks as sketched in Fig. 7.1.a shows a distinct Fano dip. The spectral overlap of a broad bright and a narrow dark mode results in a characteristic dip in the extinction spectra as plotted in Fig. 7.1.b. By changing the size of the nanodisk, the spectral feature can be moved similar to the rod antenna resonances. By placing the quantum dots precisely in a near-field hot spot of the dark or bright mode, a selective excitation of only one of the modes could be investigated.

We envision that in combination with a third lithography step an active, switchable active plasmonic nanoantenna could be built. A part element of a complex antenna structure, like a disk of the pentamer, could be covered in a photochromic material, i.e., a material with a complex refractive index that can be switched by light inducing a chemical reactions. That way the emission profile could be controlled by a second light field.

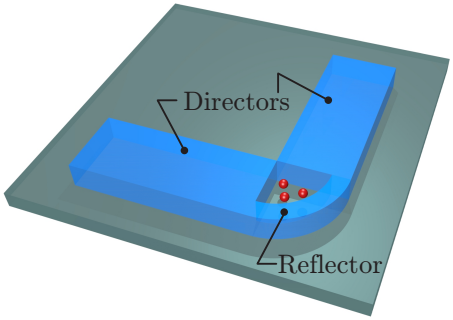

Figure 7.2: Design of a two-way active dielectric nanoantenna. It consists of two directors perpendicular to each other and a ring-shaped reflector.

Active Dielectric Nanoantennas

We think the active dielectric nanoantennas presented here are promising candidates for future applications. There is a large set of interesting experiments based on the results of this work that can be conducted to get more insight over its working principle and bring it closer to applications. All of the ideas presented here are pursued in Phd- and master theses building on the work presented.

A decomposition of the building blocks of the antenna would help to understand the benefit of the reflector, i.e, comparing the far-field patterns of active dielectric nanoantennas with single reflectors or directors would clarify the role of the individual building blocks. Additionally, fabricating antennas with a variation of the director geometry could help to increase the understanding of the details of the radiation pattern: By changing the cross section and measuring the beam direction, the propagation constant of the different waveguides could be conducted. Even though there is no resonance behavior depending on the director length, varying it, will influence the width of the main lobe and the strength of side lobes. A detailed analysis of this relationship will help to design antennas with even higher directionality.

The high bandwidth of the antennas could further be investigated by using quantum dots with different emission wavelengths. Because they are available with the same polymer coating, the deposition process should still be feasible. Since we expect different beam directions when varying the propagation constant in the director, a mixture of different quantum dots in the feed gap would be interesting to investigate. The waveguide dispersion would lead to the different fluorescence colors being emitted in diverging angels, which could be used for demultiplexing.

Together with our collaborates we aim to build a more complex antenna based on the original design idea that could help to investigate the distribution of dipole orientations in the feed gap. Figure 7.2 shows a sketch of the design consisting

of two directors perpendicular to each other. A ring-shaped reflector connects them. The fabrication challenge lies in the feed gap area, which would resemble a free standing PMMA column during the lithographic process prone to tilting over. In a working two-way antenna however, the dipoles orientated parallel to the director axis, which do not couple efficiently to the antenna mode, can couple to the perpendicular director. The different polarization states would be spatially separated. The overall coupling efficiency of the quantum dot ensemble would increase.

The losslessness of the antennas was deduced in this thesis from the known optical parameters of the used materials, however not quantified. A measurement of this quantity would surely benefit the reach for applications. Since there is no control over the orientation of the quantum dots, it would be easiest to base such an experiment on averaging over a large number of antennas. The collected power of quantum dot patches without antennas would be compared to the same measurement for active nanoantennas to get information on the loss introduced by the antennas.

We envision an application that would benefit from the losslessness of the design and emerges naturally from the fabrication process. It has been shown that colloidal semiconductor quantum dots similar to the ones used in this thesis can be single photon sources even at room temperature [128]. A dielectric antenna in combination with a single quantum dot may be used as a highly directional single-photon source without inherent losses. By placing the dielectric antenna into a liquid crystal cell, the beam direction can potentially be tuned electrically.

Chapter 8

Conclusion

This thesis presents results on the fabrication, investigation and characterization of active optical nanoantennas. The three partial results in order of their occurrence are: (i) The demonstration of the operational capability and versatility of a quantum dot deposition technique by fabricating active plasmonic and dielectric nanoantennas. (ii) The optical detection of dark modes of plasmonic nanoantennas. (iii) The optical characterization of the novel dielectric nanoantennas.

A versatile method to deposit quantum dots on nanostructured samples to produce an active optical nanoantennas was developed during the course of this thesis. The deposition technique is based on electron-beam lithography, where a template is written in a resist. The developed holes in the polymer define sites to deposit the quantum dots. To ensure an enduring attachment, a zero-length linking is used. The precision of the placement is governed by the smallest hole, that can be written by electron-beam lithography and is here in the order of 30 nm. The accuracy is given by the ability to rebuilt the coordinate system of the underlying structure and is typically about 5 nm. Since this method bases on standard techniques, it can be employed in scientific research and large scale fabrication of devices as well. It can be used to fabricate individual structures with quantum emitters attached as well as structured active thin films. The size of structured regions is only limited by the write field of the lithographic setup.

The versatility of the method was shown in this thesis by producing structured quantum dot films of various sizes and placing quantum dots on top of nanostructures of divers materials. In the thesis the technique was not developed for its own sake, but applied to two different experiments. Precise placed quantum dots were used to built active gold and hafnium dioxide nanoantennas.

The optical characterization of both antenna types was conducted in a setup that was developed as a confocal microscope with versatile means to measure the properties of nanoantennas. Maps of the reflectivity of the sample produce a standard confocal scanning image of the sample. The fluorescence can be recorded as in a confocal fluorescence microscope. A polarizing beam splitter and two detectors complement it to a polarization-sensitive fluorescent microscope. Additionally, a

Fourier imaging setup was added such that the angular intensity distribution, i.e., the far-field pattern, of emitters can be recorded up to angles of 78°. Additionally attached to the setup is a dark-field spectrometer capable of measuring the relative scattering cross section of individual nanoscatterers.

The experiments on the well known gold rod nanoantennas focused on the investigation of dark modes. Modes are called dark, when they are non-dipolar and thus do not or only weakly interact with far fields under normal incident. A comb of active nanoantennas with lengths increasing from $L = 70\,\mathrm{nm}$ to $L = 320\,\mathrm{nm}$ was fabricated. The antennas' resonance wavelengths is known to scale linearly with the antenna length such that the resonances of this antenna comb scans over the fluorescence spectrum of the quantum dots. The extinction cross sections of the individual nanoantennas were measured with dark-field spectroscopy. For the smallest set of antennas the fundamental resonance shifts with increasing length from $\lambda = 700\,\mathrm{nm}$ over the quantum dot spectrum into the infrared. For the longest set of antennas the third-order resonance was recorded around $\lambda = 750\,\mathrm{nm}$. Its strength is just over the measurement sensitivity. The second-order, non-dipolar mode could not be measured with this far-field method. Using the quantum dots as feed elements in the hot spot of the antennas, resonances in the nanoantennas were excited with a near-field method, i.e., the quantum dot emitted fluorescence moderated by the antenna into the far field. As expected, the first-order resonance, as measured with the dark-field spectroscope, produced an enhanced, polarized fluorescence signal. Additionally, a fluorescence enhancement for longer antennas was measured. Since it does not coincidence in strength or spectrally with the third-order mode, it can be attributed to the second-order, non-dipolar mode. Thus, this measurement is a proof of principle of a direct detection of dark modes in nanostructures. This additional insight in the operating principles of nanostructures could benefit the design of more complex plasmonic applications.

The second nanostructure investigated is a novel type of optical antenna. The nanoantenna design based on the operating principle of leaky-wave antennas was fabricated and equipped with quantum dots. It consists of only two simple dielectric building blocks and has a total length of approximately three times the free-space operation wavelength. The fluorescence of the quantum dots excites a leaky mode in the director by end-fire coupling. Light propagating along the director is continuously coupled to radiating modes in the substrate and emitted into the glass. With Fourier imaging, the far-field pattern of individual antennas was measured and shown to be highly directional. The directivity of the antenna was measured to be $D = 12.5\,\mathrm{dB}$. Together with numerical calculations, polarization dependent measurements gave insight in the different coupling strength in regards of the quantum dots' dipole orientation relative to the antenna. Experiments with different antenna sizes indicate the broadband operation of the nanoantenna design. It can be easily adapted to various low-loss dielectric materials. Moreover,

its non-resonant nature makes the antenna design inherently robust against fabrication imperfections and guarantees broad-band operation. These characteristics make the active antenna a promising candidate for future applications. We envision that the dielectric antenna in combination with a single quantum emitter may be used as a highly directional single-photon source without inherent losses. By placing the dielectric antenna into a liquid crystal cell, the beam direction can potentially be tuned electrically.

Bibliography

[1] Busch, K. *et al.* Periodic nanostructures for photonics. *Phys. Rep.* **444**, 101–202 (2007).

[2] Homburg, O., Hauschild, D. & Lissotschenko, V. Manufacturing and application of micro-optics. *Opt. & Phot.* **3**, 48–52 (2008).

[3] Meschede, D. *Optics, Light and Lasers* (Wiley-VCH, Weinheim, 2007).

[4] Träger, F. *Springer handbook of lasers and optics* (Springer Science & Business Media, New York, 2012).

[5] Ozbay, E. Plasmonics: merging photonics and electronics at nanoscale dimensions. *science* **311**, 189–193 (2006).

[6] Meyer, H. *et al.* Direct photonic coupling of a semiconductor quantum dot and a trapped ion. *Phys. Rev. Lett.* **114**, 123001 (2015).

[7] Kok, P. *et al.* Linear optical quantum computing with photonic qubits. *Rev. Mod. Phys.* **79**, 135 (2007).

[8] Lu, Y.-J. *et al.* Plasmonic nanolaser using epitaxially grown silver film. *Science* **337**, 450–453 (2012).

[9] Bharadwaj, P., Deutsch, B. & Novotny, L. Optical Antennas. *Adv. Opt. Photon.* **1**, 438 (2009).

[10] Novotny, L. & Hecht, B. *Principles Of Nano-Optics* (Cambridge University Press, Cambridge, 2012).

[11] Eisler, H., Martin, O. J. F., Hecht, B., Mu, P. & Pohl, D. W. Resonant Optical Antennas. *Science* **308**, 1607–1609 (2005).

[12] Biagioni, P., Huang, J. & Hecht, B. Nanoantennas for visible and infrared radiation. *Rep. Prog. Phys.* **024402**, 76 (2012).

[13] Taminiau, T., Stefani, F., Segerink, F. & Van Hulst, N. Optical antennas direct single-molecule emission. *Nat. Photonics* **2**, 234–237 (2008).

[14] Lal, S., Link, S. & Halas, N. J. Nano-optics from sensing to waveguiding. *Nat. Photonics* **1**, 641–648 (2007).

[15] Maier, S. A. *Plasmonics: Fundamentals And Applications* (Springer Science & Business Media, New York, 2007).

[16] Krasnok, A. E. *et al.* Optical nanoantennas. *Phys. Usp.* **56**, 539–564 (2013).

[17] Pfeiffer, M. *et al.* Enhancing the optical excitation efficiency of a single self-assembled quantum dot with a plasmonic nanoantenna. *Nano Lett.* **10**, 4555–4558 (2010).

[18] Ureña, E. B. *et al.* Excitation enhancement of a quantum dot coupled to a plasmonic antenna. *Adv. Mater.* **24** (2012).

[19] Linnenbank, H., Grynko, Y., Förstner, J. & Linden, S. Second harmonic generation spectroscopy on hybrid plasmonic / dielectric nanoantennas. *Light: Sci. Appl.* **5**, 1–7 (2015).

[20] Metzger, B. *et al.* Strong enhancement of second harmonic emission by plasmonic resonances at the second harmonic wavelength. *Nano Lett.* **15**, 3917–3922 (2015).

[21] Schumacher, T. *et al.* Nanoantenna-enhanced ultrafast nonlinear spectroscopy of a single gold nanoparticle. *Nat. Commun.* **2**, 333 (2011).

[22] Wang, H. F. *et al.* In vitro and in vivo two-photon luminescence imaging of single gold nanorods. *Proc. Natl. Acad. Sci. U.S.A.* **102**, 15752–15756 (2005).

[23] Ghenuche, P., Cherukulappurath, S., Taminiau, T. H., van Hulst, N. F. & Quidant, R. Spectroscopic mode mapping of resonant plasmon nanoantennas. *Phys. Rev. Lett.* **101**, 116805 (2008).

[24] Kühn, S., Håkanson, U., Rogobete, L. & Sandoghdar, V. Enhancement of single-molecule fluorescence using a gold nanoparticle as an optical nanoantenna. *Phys. Rev. Lett.* **97**, 017402 (2006).

[25] Curto, A. G. *et al.* Unidirectional emission of a quantum dot coupled to a nanoantenna. *Science* **329**, 930–933 (2010).

[26] Hoang, T. B. *et al.* Ultrafast spontaneous emission source using plasmonic nanoantennas. *Nat. Commun.* **6**, 7788 (2015).

[27] Dregely, D. *et al.* Imaging and steering an optical wireless nanoantenna link. *Nat. Commun.* **5** (2014).

[28] Farahani, J. N., Pohl, D. W., Eisler, H. J. & Hecht, B. Single quantum dot coupled to a scanning optical antenna: A tunable superemitter. *Phys. Rev. Lett.* **95** (2005).

[29] Muskens, O. L., Giannini, V., Sánchez-Gil, J. A. & Gómez Rivas, J. Strong enhancement of the radiative decay rate of emitters by single plasmonic nanoantennas. *Nano Lett.* **7**, 2871–2875 (2007).

[30] Knight, M. W. *et al.* Aluminum Plasmonic Nanoantennas. *Nano Lett.* **12**, 6000–6004 (2012).

[31] Zhao, Q., Zhou, J., Zhang, F. & Lippens, D. Mie resonance-based dielectric metamaterials. *Mater. Today* **12**, 60–69 (2009).

[32] Staude, I. *et al.* Tailoring directional scattering through magnetic and electric resonances in subwavelength silicon nanodisks. *ACS Nano* **7**, 7824–7832 (2013).

[33] Fu, Y. H., Kuznetsov, A. I., Miroshnichenko, A. E., Yu, Y. F. & Luk'yanchuk, B. Directional visible light scattering by silicon nanoparticles. *Nat. Commun.* **4**, 1527 (2013).

[34] Liu, N., Tang, M. L., Hentschel, M., Giessen, H. & Alivisatos, A. P. Nanoantenna-enhanced gas sensing in a single tailored nanofocus. *Nat. Mater.* **10**, 631–636 (2011).

[35] Zhang, W., Huang, L., Santschi, C. & Martin, O. J. Trapping and sensing 10 nm metal nanoparticles using plasmonic dipole antennas. *Nano Lett.* **10**, 1006–1011 (2010).

[36] Kinkhabwala, A. *et al.* Large single-molecule fluorescence enhancements produced by a bowtie nanoantenna. *Nat. Photonics* **3**, 654–657 (2009).

[37] Bharadwaj, P., Beams, R. & Novotny, L. Nanoscale spectroscopy with optical antennas. *Chem. Sci.* **2**, 136–140 (2011).

[38] Zuloaga, J. & Nordlander, P. On the energy shift between near-field and far-field peak intensities in localized plasmon systems. *Nano Lett.* **11**, 1280–1283 (2011).

[39] Yang, S.-C. *et al.* Plasmon hybridization in individual gold nanocrystal dimers: direct observation of bright and dark modes. *Nano Lett.* **10**, 632–637 (2010).

[40] Lovera, A., Gallinet, B., Nordlander, P. & Martin, O. J. Mechanisms of fano resonances in coupled plasmonic systems. *ACS Nano* **7**, 4527–4536 (2013).

[41] Hentschel, M. *et al.* Transition from isolated to collective modes in plasmonic oligomers. *Nano Lett.* **10**, 2721–2726 (2010).

[42] Zhang, S., Genov, D. A., Wang, Y., Liu, M. & Zhang, X. Plasmon-induced transparency in metamaterials. *Phys. Rev. Lett.* **101**, 047401 (2008).

[43] Giannini, V., Fernández-Domínguez, A. I., Heck, S. C. & Maier, S. A. Plasmonic nanoantennas: fundamentals and their use in controlling the radiative properties of nanoemitters. *Chem. Rev.* **111**, 3888–3912 (2011).

[44] Johnson, R. C. *Antenna Engineering Handbook* (McGraw-Hill, New York, 2007).

[45] Monticone, F. & Alù, A. Leaky-wave theory, techniques, and applications: From microwaves to visible frequencies. *Proc. IEEE* **103**, 793–821 (2015).

[46] Shegai, T. *et al.* Unidirectional broadband light emission from supported plasmonic nanowires. *Nano Lett.* **11**, 706–711 (2011).

[47] Esquius-Morote, M., Gomez-Diaz, J. S. & Perruisseau-Carrier, J. Sinusoidally modulated graphene leaky-wave antenna for electronic beamscanning at THz. *IEEE Trans. THz Sci. Technol.* **4**, 116–122 (2014).

[48] Fadel, M., Azim M, O., Omer, O. & Basily, R. A study of some optical properties of hafnium dioxide (HfO2) thin films and their applications. *Appl. Phys. A.* **66**, 335–343 (1998).

[49] Kern, J. *et al.* Electrically driven optical antennas. *Nat. Photonics* **9**, 582–586 (2015).

[50] Pfeiffer, M. *et al.* Positioning plasmonic nanostructures on single quantum emitters. *Phys. Status Solidi B* **249**, 678–686 (2012).

[51] Wientjes, E., Renger, J., Curto, A. G., Cogdell, R. & Van Hulst, N. F. Strong antenna-enhanced fluorescence of a single light-harvesting complex shows photon antibunching. *Nat. Commun.* **5** (2014).

[52] Akimov, A. *et al.* Generation of single optical plasmons in metallic nanowires coupled to quantum dots. *Nature* **450**, 402–406 (2007).

[53] Weeber, J.-C. *et al.* Colloidal quantum dot integrated light sources for plasmon mediated photonic waveguide excitation. *ACS Photonics* **3**, 844–852 (2016).

[54] Kraus, T. *et al.* Nanoparticle printing with single-particle resolution. *Nat. Nanotech.* **2**, 570–576 (2007).

[55] Gruber, C., Kusar, P., Hohenau, A. & Krenn, J. R. Controlled addressing of quantum dots by nanowire plasmons. *Appl. Phys. Lett.* **100**, 231102 (2012).

[56] Maxwell, J. C. A dynamical theory of the electromagnetic field. *Phil. Trans.* **155**, 459–512 (1865).

[57] Jackson, J. D. *Classical Electrodynamics* (John Wiley & Sohns, New York, 1999).

[58] Drude, P. Zur Elektronentheorie der Metalle. *Ann. Phys.* **306**, 566–613 (1900).

[59] Born, M. & Wolf, E. *Principles of optics* (Cambridge University Press, Cambridge, 1999).

[60] Dressel, M. & Scheffler, M. Verifying the drude response. *Ann. Phys.* **15**, 535–544 (2006).

[61] Kittel, C. *Introduction to Solid State Physics* (John Wiley & Sohns, New York, 2005).

[62] Wooten, F. *Optical Properties of Solids* (Academic Press, New York, 1972).

[63] Lorentz, H. A. The motion of electrons in metallic bodies. i. *Proc. Kon. Ned. Akad. Wet.* **7**, 438–453 (1905).

[64] Bohren, C. F. & Huffman, D. R. *Absorption and Scattering of Light by Small Particles* (John Wiley & Sohns, New York, 1983).

[65] Jellison Jr, G. & Modine, F. Parameterization of the optical functions of amorphous materials in the interband region. *Appl. Phys. Lett.* **69**, 371–373 (1996).

[66] Tompkins, H. & Irene, E. A. *Handbook of Ellipsometry* (William Andrew, Norwich, 2005).

[67] Myroshnychenko, V. *et al.* Modelling the optical response of gold nanoparticles. *Chem. Soc. Rev.* **37**, 1792–1805 (2008).

[68] Jasik, H. *Antenna Engineering Handbook* (McGraw-Hill Book Company, New York, 1961).

[69] Balanis, C. A. *Antenna Theory* (John Wiley & Sohns, New Jersey, 2016).

[70] Kraus, J. & Marhefka, R. *Antennas For All Applications* (McGraw-Hill, New York, 2002).

[71] Hertz, H. Ueber Strahlen electrischer Kraft. *Wied. Ann.* **272**, 769–783 (1889).

[72] Hertz, H. Ueber die Ausbreitungsgeschwindigkeit der electrodynamischen Wirkungen. *Wied. Ann.* **270**, 551–569 (1888).

[73] Novotny, L. Effective wavelength scaling for optical antennas. *Phys. Rev. Lett.* **98** (2007).

[74] Krenn, J. *et al.* Design of multipolar plasmon excitations in silver nanoparticles. *Appl. Phys. Lett.* **77**, 3379–3381 (2000).

[75] Hansen, W. Radiating electromagnetic wave guide (1946). US Patent 2,402,622.

[76] Saleh, B. E. A. & Teich, M. C. *Fundamentals of Photonics* (John Wiley & Sohns, New York, 1991).

[77] Ekimov, A. I., Efros, A. L. & Onushchenko, A. A. Quantum size effect in semiconductor microcrystals. *Sol. State Comm.* **56**, 921–924 (1985).

[78] Schmid, G. *Nanoparticles* (Wiley-VCH, Weinheim, 2010).

[79] Rooksby, H. The colour of selenium ruby glasses. *J. Soc. Glass Techn.* **16**, 171 (1932).

[80] Woggon, U. *Optical Properties of Semiconductor Quantum Dots* (Springer, Berlin, 1997).

[81] Ekimov, A. & Onushchenko, A. Size quantization of the electron energy spectrum in a microscopic semiconductor crystal. *JETP Lett.* **40**, 1136–1139 (1984).

[82] Rossetti, R., Ellison, J., Gibson, J. & Brus, L. E. Size effects in the excited electronic states of small colloidal Cds crystallites. *J. Chem. Phys.* **80**, 4464–4469 (1984).

[83] Chakraborty, T. *Quantum Dots* (Elsevier, Amsterdam, 1999).

[84] Jacak, L., Wójs, A. & Paweł, H. *Quantum Dots* (Springer, Berlin, 1998).

[85] Purcell, E. M. Spontaneous Emission Probabilities at Radio Frequencies. *Phys. Rev.* **69**, 681 (1946).

[86] Lukosz, W. & Kunz, R. Light emission by magnetic and electric dipoles close to a plane interface. i. total radiated power. *J. Opt. Soc. Am.* **67**, 1607–1615 (1977).

[87] Lukosz, W. & Kunz, R. Light emission by magnetic and electric dipoles close to a plane dielectric interface. ii. radiation patterns of perpendicular oriented dipoles. *J. Opt. Soc. Am.* **67**, 1615–1619 (1977).

[88] Rogers, J. A. & Nuzzo, R. G. Recent progress in soft lithography. *Mater. Today* **8**, 50–56 (2005).

[89] Guillot, N. & de la Chapelle, M. L. Lithographied nanostructures as nanosensors. *J. Nanophotonics* **6**, 064506–1 (2012).

[90] Malloy, M. & Litt, L. C. Technology review and assessment of nanoimprint lithography for semiconductor and patterned media manufacturing. *J Micro Nanolithogr MEMS MOEMS* **10**, 032001–032001 (2011).

[91] Hameka, H. F. *Quantum Mechanics* (John Wiley & Sohns, New Jersey, 2004).

[92] SCHOTT AG. *D 263® M – Glass for Microscopy Cover Slips* (13/03/2017). URL `http://www.schott.com/`.

[93] Present status of transparent conducting oxide thin-film development for indium-tin-oxide (ito) .

[94] Norrman, K., Ghanbari-Siahkali, A. & Larsen, N. 6 studies of spin-coated polymer films. *Ann. Rep. Progr. Chem.* **101**, 174–201 (2005).

[95] Micro Chem. *PMMA Data Sheet* (08/03/2017). URL `http://www.microchem.com/pdf/PMMA_Data_Sheet.pdf`.

[96] Allresist. *AR-P 631-679 e-beam resists for nanometer lithography* (13/03/2017). URL `http://www.allresist.com/`.

[97] Barnes, M. C., Kim, D.-Y., Ahn, H. S., Lee, C. O. & Hwang, N. M. Deposition mechanism of gold by thermal evaporation: approach by charged cluster model. *J. Cryst. Growth.* **213**, 83–92 (2000).

[98] Buzea, C. & Robbie, K. State of the art in thin film thickness and deposition rate monitoring sensors. *Rep. Prog. Phys.* **68**, 385 (2005).

[99] Al-Kuhaili, M., Durrani, S. & Khawaja, E. Characterization of hafnium oxide thin films prepared by electron beam evaporation. *J. Phys. D: Appl. Phys.* **37**, 1254 (2004).

[100] Lee, K., Chromey, N., Culik, R., Barnes, J. & Schneider, P. Toxicity of n-methyl-2-pyrrolidone (nmp): teratogenic, subchronic, and two-year inhalation studies. *Toxicol. Sci.* **9**, 222–235 (1987).

[101] Broers, A., Hoole, A. & Ryan, J. Electron beam lithography—resolution limits. *Microelectron. Eng.* **32**, 131–142 (1996).

[102] Alberti, J., Linnenbank, H., Linden, S., Grynko, Y. & Förstner, J. The role of electromagnetic interactions in second harmonic generation from plasmonic metamaterials. *Appl. Phys. B* **122**, 1–5 (2016).

[103] von Cube, F. *et al.* From isolated metaatoms to photonic metamaterials: evolution of the plasmonic near-field. *Nano Lett.* **13**, 703–708 (2013).

[104] Eyerer, P., Hirth, T. & Elsner, P. *Polymer Engineering* (Springer-Verlag, Berlin Heidelberg, 2008).

[105] Alivisatos, A. P. Semiconductor clusters, nanocrystals, and quantum dots. *Science* **271**, 933 (1996).

[106] Liang, G.-X. *et al.* Fabrication of near-infrared-emitting cdsete/zns core/shell quantum dots and their electrogenerated chemiluminescence. *Chem. Commun.* **46**, 2974–2976 (2010).

[107] Medintz, I. L., Uyeda, H. T., Goldman, E. R. & Mattoussi, H. Quantum dot bioconjugates for imaging, labelling and sensing. *Nat. Mater.* **4**, 435–446 (2005).

[108] Carl Zeiss NTS - Nano Technology System Division. *Sigma Instruction Manual – Operator's User Guide* (05/2011).

[109] Shipway, A. N., Katz, E. & Willner, I. Nanoparticle arrays on surfaces for electronic, optical, and sensor applications. *ChemPhysChem* **1**, 18–52 (2000).

[110] Na, Y. J., Park, S. J., Lee, S. W. & Kim, J. S. Photolithographic process for the patterning of quantum dots. *Ultramicroscopy* **108**, 1297–1301 (2008).

[111] ThermoFisher Scientific – invitrogen. *Qdot ITK Carboxyl Quantum Dots* (09/03/2017). URL `https://tools.thermofisher.com/content/sfs/manuals/mp19020.pdf`.

[112] Nakajima, N. & Ikada, Y. Mechanism of amide formation by carbodiimide for bioconjugation in aqueous media. *Bioconjugate Chem.* **6**, 123–130 (1995).

[113] Hermanson, G. T. *Bioconjugate Techniques* (Academic Press, San Diego, 1996).

[114] Lilley, C. M. & Huang, Q. Surface contamination effects on resistance of gold nanowires. *Appl. Phys. Lett.* **89**, 203114 (2006).

[115] Valerini, D. *et al.* Temperature dependence of the photoluminescence properties of colloidal cd se/ zn s core/shell quantum dots embedded in a polystyrene matrix. *Phys. Rev. B* **71**, 235409 (2005).

[116] Sheppard, C. J. R. & Shotton, D. M. *Confocal Laser Scanning Microscopy* (BIOS Scientific Publishers, Oxford, 1997).

[117] Corle, T. R. & Kino, G. S. *Confocal Scanning Optical Microscopy and Related Imaging System* (Academic Press, San Diego, 1996).

[118] Richards, B. & Wolf, E. Electromagnetic diffraction in optical systems. II. Structure of the image field in an aplanatic system. *Proc. R. Soc. A* **253**, 358–379 (1959).

[119] Husnik, M. *et al.* Absolute extinction cross-section of individual magnetic split-ring resonators. *Nat. Photonics* **2**, 614–617 (2008).

[120] Wood, R. Xlii. on a remarkable case of uneven distribution of light in a diffraction grating spectrum. *Philos. Mag.* **4**, 396–402 (1902).

[121] Hu, M. *et al.* Dark-field microscopy studies of single metal nanoparticles: understanding the factors that influence the linewidth of the localized surface plasmon resonance. *J. Mater. Chem.* **18**, 1949–1960 (2008).

[122] Weigel, A., Sebesta, A. & Kukura, P. Dark field microspectroscopy with single molecule fluorescence sensitivity. *ACS Photonics* **1**, 848–856 (2014).

[123] Werra, J. F. M. *Probing plasmonic nanostructures.* Ph.D. thesis, Humboldt-Universität zu Berlin, Mathematisch-Naturwissenschaftliche Fakultät (2016).

[124] Peter, M. *et al.* Directional emission from dielectric leaky-wave nanoantennas. *Nano Lett.* (2017).

[125] Hildebrandt, A., Reichelt, M., Meier, T. & Förstner, J. Engineering plasmonic and dielectric directional nanoantennas. *SPIE OPTO* **8984**, 89841G (2014).

[126] Zhu, H., Tang, C., Fonseca, L. & Ramprasad, R. Recent progress in ab initio simulations of hafnia-based gate stacks. *J. Mater. Sci.* **47**, 7399–7416 (2012).

[127] Weiland, T. A discretization model for the solution of maxwell's equations for six-component fields. *Electron. Commun. AEU* **31**, 116–120 (1977).

[128] Michler, P. *et al.* Quantum correlation among photons from a single quantum dot at room temperature. *Nature* **406**, 968–970 (2000).

Publications

Parts of this work have been published in an electronics preprint repository:

- Peter, M. *et al.* Directional Emission from Dielectric Leaky-Wave Nanoantennas. *Nano Lett.* (2017)

Parts of this work have been presented on international conferences:

- Peter, M., Friesen, C., & Linden, S. Fabrication and characterization of active plasmonic antennas. *9th International Congress on Advanced Electromagnetic Materials in Microwaves and Optics (METAMATERIALS)*, 256—258 (IEEE, 2015).
- Peter, M., Hildebrandt, A., Förstner, J., & Linden, S. Directional Emission from Active Dielectric Nano Antennas. *6th International Topical Meeting on Nanophotonics and Metamaterials (NANOMETA)*, (EPS, 2017).

Danksagung

Am Ende dieser Arbeit möchte ich auf Deutsch Menschen danken, die mich unterstützt haben:
Ich möchte mich zuerst bei Prof. Stefan Linden für die Betreuung meiner Doktorarbeit bedanken. Er hat sich immer viel Zeit für meine Arbeit genommen und Probleme ausführlich mit mir diskutiert. Viele erfolgreiche Ideen dieser Arbeit sind aus diesen Gesprächen mit ihm erwachsen.
Mein Dank gilt außerdem Priv.-Doz. Elisabeth Soergel für die Anfertigung des Zweitgutachtens meiner Arbeit, sowie Prof. Johann Kroha und Prof. Moritz Sokolowski für die Bereitschaft Mitglieder meiner Promotionskommission zu werden.
Ich danke André Hildebrandt und Julia Werra für die Zusammenarbeit und die Durchführung der numerischen Berechnungen. Ich bedanke mich bei Prof. Klas Lindfors, der mit mir zusammen die Quantenpunktspektroskopie bei tiefen Temperaturen durchgeführt hat. Danke an die EMA-Gruppe und die Mitarbeiter des Reinraums am Forschungsinstitut caesar, die mich mit meiner Arbeit dort unterstützt haben.
Unser Arbeitsgruppe war für mich immer besonders: Als inoffizielle Gruppe von Pionieren haben Felix Bleckmann, Felix von Cube, Heiko Linnenbank und Thorsten Weber mit mir in Gesprächen viele Ideen und Lösungen entwickelt und ich habe mit ihnen tolle Momente als Gruppe von Freunden erlebt. Danke!
Ein Teil des Doktorandenberufs, der mir besonders viel Freude gemacht hat, ist das Betreuen von Abschlussarbeiten. Ich habe während zwei Bachelor- und vier Masterarbeiten, die ich als Betreuer begleiten durfte, viele Diskussionen geführt und neue Ideen umgesetzt, die in diese Arbeit eingeflossen sind. Aus diesen Zusammenarbeiten sind mir sehr wichtige Freundschaften erwachsen. Stellvertretend möchte ich hier Kimia Gharib und Cody Friesen erwähnen: Thanks!
Auch vielen Menschen, die keine PhysikerInnen sind, muss ich danken: meinen Geschwistern, Björn, Annika und Julia, Freunden und Pfadfindern, die mich begleitet haben. Die vielen, vielen Menschen, die ich gerne um mich habe und die mich unterstützen, fallen häufig gleich in mehrere dieser Kategorien. Stellvertretend seien hier Benedikt und Simon erwähnt.
Großen Dank schulde ich meinen Eltern: Sie sind großartige Menschen, die mich immer unterstützt haben. Ihren Beitrag zu dieser Arbeit kann ich nicht überschätzen. Mein größter Dank gilt Natalie, die mich als die klügere Physikerin von uns beiden, hilfsbereite Kollegin, beste Freundin und Gefährtin trägt.